SPIKE DYNAMICS IN 2-COMPONENT AND 3-COMPONENT REACTION DIFFUSION SYSTEMS

by

Chunyi Gai

Submitted in partial fulfillment of the requirements
for the degree of Doctor of Philosophy

at

Dalhousie University
Halifax, Nova Scotia
August 2021

Table of Contents

List of Tables

List of Figures

Abstract

In this thesis, we study spike dynamics and stability in different reaction-diffusion systems. Since localized patterns are "far-from-equilibrium" structures, the classical Turing-type stability analysis is not applicable. Instead, we apply the method of matched asymptotic expansions and nonlocal eigenvalue problems to analyze these singular perturbed PDEs.

In the first part of the thesis, we investigate an SIRS model with spatial diffusion and nonlinear incidence rates. We show that for small diffusion rate of the infected class, the infected population tends to be highly localized. We then study three distinct destabilization mechanisms, as well as a transition from localized spikes to plateau solutions. In all cases, the stability thresholds are computed asymptotically and are verified by numerical experiments.

In the second part we study the effect of noise on spike dynamics for the Gierer-Meinhardt model. When spatial-temporal noise is introduced in the activator equation, we derive a stochastic ODE that describes the motion of a single spike. For small noise level, the spike can deviate from the domain center but remains "trapped" within a subinterval. For larger noise levels, the spike undergoes large excursions that eventually collide with the domain boundary. We then derive the expected time for the spike to collide with the boundary.

In third part we propose an extension of the Klausmeier model to two plant species that consume water at different rates. We are interested in how the competition for water affects stability of plant patches. We find a finite range of precipitation rate for which two species can co-exist. Outside of that range, the frugal species outcompetes the thirsty species. There is sequence of stability thresholds such that thirsty plant patches are the first to die off, while the frugal spots remain resilient for longer.

In the end, an analysis is undertaken of the formation and stability of localized patterns in the Schnakenberg model with source terms in both the activator and inhibitor fields. Single-spike patterns are constructed and we then derive the nonlocal eigenvalue problem and study a Hopf bifurcation in the amplitudes of the spike.

Acknowledgements

I would like to thank my supervisor, Dr. Theodore Kolokolnikov. His expert guidance, patience and continuous support helped me in all of my time of studies and the completion of this thesis. I would also like to thank our collaborators David Iron, John Rumsey, Fahad Al Saadi and Alan Champneys for the valuable discussions and ideas. To the end, I would like to sincerely thank Dr. Michael Ward for so kindly supporting me as a visiting student of UBC for a year.

I am grateful for financial support from my supervisor, Dalhousie graduate scholarship and NSGS Scholarship.

Chapter 1

Introduction

Reaction-diffusion systems play an important role as fundamental models in many areas, such as biology, chemistry, physics and ecology. They can describe a wide class of spatio-temporal patterns observed in the physical world as well as in living systems. In recent years, the study of spatial pattern formation and dynamics in reaction-diffusion systems has gained increasing attention and many new developments have been made.

In this thesis, we analyze the dynamics and stability of spike patterns in four different reaction-diffusion systems. The first model, studied in chapter 2, is the SIRS epidemic model, initially formulated with no diffusion. It was first introduced by Kermack and McKendrick in 1927 [1] and is widely used to model the spread of infectious diseases. In the model, the population is divided into three disjoint classes: susceptible (S), infected (I), and recovered (R), where susceptibles can be infected by those already infected and subsequently recover, and the recovered class is immune to the disease but loses immunity over time. With diffusion terms included, it can be written as

$$\begin{cases} S_t = D_S S_{xx} - SI^2 + \gamma R, \quad x \in [-L, L], \quad t > 0, \\ I_t = \varepsilon^2 I_{xx} + SI^2 - I, \quad x \in [-L, L], \quad t > 0, \\ R_t = D_R R_{xx} + I - \gamma R, \quad x \in [-L, L], \quad t > 0, \\ \qquad S_x = I_x = R_x = 0 \quad \text{at} \pm L, \end{cases} \tag{1.1}$$

where D_S, ε^2, D_R are the diffusion coefficients of each class of population, and γ is the rate of immunity loss.

The second model, studied in chapter 3, is the Gierer-Meinhardt system. It was introduced in [2] to describe biological morphogenesis. This model is known to have a rich pattern-formation structure [2, 3, 4]. In this thesis, we study the effect of noise on spike dynamics for the classical Gierer-Meinhardt model and we consider the

following equations:

$$\begin{cases} u_t = \varepsilon^2 u_{xx} - u + \frac{u^2}{v} + \sigma u W \frac{\sqrt{dt}}{dt}, \quad x \in [-L, L], \quad t > 0, \\ 0 = v_{xx} - v + \frac{u^2}{\varepsilon}, \quad x \in [-L, L], \quad t > 0, \\ \qquad u_x = v_x = 0 \quad \text{at} \quad x = \pm L. \end{cases} \tag{1.2}$$

Here u and v represent the activator and the inhibitor concentrations, ε^2 is the diffusion rate of activator and we assume $0 < \varepsilon \ll 1$. The term $\sigma u W \frac{\sqrt{dt}}{dt}$ is the differential form of the spatio-temporal Gaussian white noise in the decay of u, in which $W(x,t)$ is a normally distributed random variable and is defined in (3.3). σ is a constant which denotes the noise size.

The third model, studied in chapter 4, is the Klausmeier model of vegetation. First proposed by Klausmeier [5], it is a widely studied reaction-diffusion model of vegetation pattern formation in semiarid environments [6, 7, 8, 9]. Here we consider a modified version of the Klausmeier model which has 3 components:

$$\begin{cases} u_{1t} = \varepsilon^2 u_{1xx} - u_1 + u_1^2 v, \quad x \in [-L, L], \quad t > 0, \\ u_{2t} = \varepsilon^2 u_{2xx} - u_2 + u_2^2 v, \quad x \in [-L, L], \quad t > 0, \\ \tau v_t = D v_{xx} + a - \frac{u_1^2 v}{\varepsilon} - \beta \frac{u_2^2 v}{\varepsilon}, \quad x \in [-L, L], \quad t > 0, \\ \qquad u_{1x} = u_{2x} = v_x = 0 \quad \text{at} \quad x = \pm L. \end{cases} \tag{1.3}$$

Here u_1, u_2 are the concentration of two plants with different water intake rates and v denotes water density. ε^2 and D are diffusion coefficients, a represents rate of rainfall, and β is the ratio of water intake rate between u_2 and u_1. τ represents the differing timescales in changes in water level versus those in plant density.

The last model, studied in chapter 5, is the Schnakenberg system. This is a basic differential equation model to describe an autocatalytic chemical reaction [10]. With assumption that the activator source term is $O(\varepsilon)$ and the substrate source is $O(\varepsilon^2)$, where ε^2 is the diffusion ratio, we have the following equations:

$$\begin{cases} u_t = \varepsilon^2 \frac{\partial^2 u}{\partial x^2} + u^2 v - u + \varepsilon\alpha, \quad x \in [-L, L], \quad t > 0, \\ v_t = \frac{\partial^2 v}{\partial x^2} - u^2 v + \varepsilon^2 \beta, \quad x \in [-L, L], \quad t > 0, \\ \qquad u_x = v_x = 0 \quad \text{at} \quad x = \pm L. \end{cases} \tag{1.4}$$

A common feature observed in these models is that their solution exhibits spikes-type patterns: a highly localized structure in space, which is concentrated on a discrete

number of points of the domain. The goal of this thesis is to study the stability and dynamics of these spike patterns.

1.1 Background

The modern theory of pattern formation was initiated by Alan Turing in 1952 [11]. In his seminal paper [11], Turing proposed a simple reaction-diffusion system to account for pattern formation in chemical systems. He introduced a linear stability analysis to show that diffusion can cause instability to a homogeneous steady state even if it's stable in the absence of diffusion, and different spatio-temporal patterns can arise in reaction-diffusion systems.

Let us recall the Turing instability analysis of reaction-diffusion systems that forms a pattern from a uniform state. A typical two-component reaction-diffusion system has the form

$$\begin{cases} U_t = D_U U_{xx} + f(U,V), \quad x \in [-L,L], \quad t > 0, \\ V_t = D_V V_{xx} + g(U,V), \quad x \in [-L,L], \quad t > 0, \\ \qquad U_x = V_x = 0 \quad \text{at} \quad x = \pm L. \end{cases} \tag{1.5}$$

This system has a spatially homogeneous equilibrium solution U_e, V_e such that $f(U_e, V_e) = g(U_e, V_e) = 0$. Next, we linearize around the equilibrium. Any random perturbation of the uniform equilibrium can be decomposed in Fourier modes ($\cos(mx)$), and each of these modes grows or decays exponentially ($e^{\lambda t}\cos(mx)$) depending on the sign of the real part $Re(\lambda_m)$. So we let

$$U = U_e + \phi e^{\lambda t}\cos(mx), \quad V = V_e + \psi e^{\lambda t}\cos(mx),$$

where ϕ and ψ are assumed small.

To satisfy the Neuwmann boundary condition, we require that $mL = j\pi$, where j is a non-negative integer. We then obtain $\lambda\vec{\eta} = J\vec{\eta}$, where $\vec{\eta} = (\phi, \psi)^T$ and

$$J = \begin{pmatrix} -m^2 D_U + f_U(U_e, V_e) & f_V(U_e, V_e) \\ g_U(U_e, V_e) & -m^2 D_V + g_V(U_e, V_e) \end{pmatrix} \tag{1.6}$$

is the corresponding Jacobian matrix. By computing the eigenvalues of J, i.e. λ_m for modes with any wavenumber m, we can find that the interaction between reactions

and diffusion can give rise to bands of unstable modes with positive growth rates, These modes with particular wavelengths are amplified out of a random perturbation, which gives rise to pattern formation.

Turing's study was extended by Segal and Jackson [12], and Gierer and Meinhardt [2], who postulated that "Turing patterns" are assumed to be driven by *"short range activation"* and *"long rang inhibition"* [13]. Later works showed that the long-range inhibition does not necessarily require an inhibitor, but can also result from the *depletion of the substrate* that is consumed during the production of the autocatalytic activator [14]. Let us illustrate how the *activator-inhibitor* mechanism and *activator-substrate* mechanism work.

For *activator-inhibitor* mechanism, we consider two chemical components. First, the (short range) activator catalyzes its own production so that its concentration can increase exponentially. However, the activator cannot increase indefinitely since the inhibitor, which is also produced by the activator, can inhibit the behavior of the activator. Secondly, the (long range) inhibitor has a much larger diffusion rate. Hence, it does not accumulate locally with the activator but diffuses laterally. Among the models studied in this thesis, Gierer-Meinhardt model is a typical *activator-inhibitor* system.

Different from the *activator-inhibitor* model, the rapidly diffusing component in a *activator-substrate* model changes to a substrate that is depleted by conversion into the activator. The long range inhibition here is due to *depletion of substrate*. Therefore, the concentration of the substrate is lowest in regions of activator peaks, in contrast to the situation in an *activator–inhibitor* system, in which the inhibitor has high values near activator peaks (see Figure 1.1). Among the models studied in this thesis, Schnackenberg model is a typical *activator-substrate* system.

Some biological systems are very complex and may contain multiple activators or substrates. In this thesis, we consider two multi-component systems, one is the SIR epidemic model (2), which is an activator-substrate-inhibitor system; the other one is the three-component Klausmeier system (1.3), which models two activators and one substrate.

In this thesis, we consider the limit where the activator diffusivity is small, in which case localized spike patterns can arise from Turing instability. Such patterns

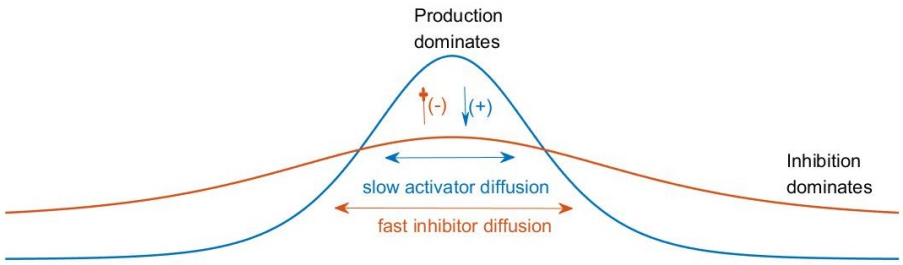

(a) Pattern formation by an activator–inhibitor mechanism

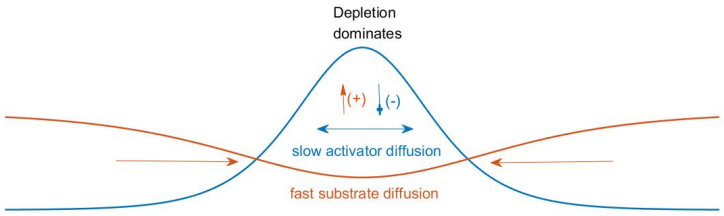

(b) Pattern formation by an activator–substrate mechanism

Figure 1.1: (a) In the activator-inhibitor model, the slowly diffusing activator catalyses its own production, which in turn stimulates the production of a fast-diffusing inhibitor that suppresses autocatalytic activator production. (b) In the activator-substrate model, the inhibitor is replaced by a substrate, and autocatalytic activator production is replaced by the autocatalytic conversion of substrate into activator.

are considered 'far-from-equilibrium' structures [15], and the conventional Turing-type stability analysis is not applicable. Starting from the 1990s, many new approaches have been introduced to study the large-amplitude patterned states.

During the last three decades, there has been great progress in the study of existence and stability for spike-type solutions. The existence of symmetric N-spike steady-state solutions in the Gierer-Meinhardt model is first established in [16]; these solutions are periodic and have the same spike height. Then in [3], the stability of the general N-spike solution for the 1-D Gierer-Meinhardt model is studied using NLEP approach. In [17], using matched asymptotic expansions, the existence and stability of asymmetric multi-spike solutions which contain two types of spikes with different heights for the one-dimensional Gierer-Meinhardt model is studied. For the case of symmetric N-spike solutions the instability always arises first from the small eigenvalues [3], while asymmetric multi-spike solutions are always unstable with respect to small eigenvalues [17].

While the 1-D problems are rather well-studied, there have been far fewer studies of the existence, linear stability, and dynamics of localized spot patterns in higher dimensions. The existence of spikes for the two-dimensional Gierer-Meinhardt system has been proved in [18, 19, 20, 21, 22]. The stability of stripes for the Gierer-Meinhardt system has been studied in [23]. This study has been extended to the Gierer-Meinhardt system with saturation in [24]. Moreover, the existence of solutions to the Gierer-Meinhardt system in three dimensions is studied in [25, 26].

The existence, linear stability, and dynamics are also studied in many other reaction-diffusion systems as well as their extensions. For example, spikes for the Schnakenberg model have been considered in [27, 28] for one dimension and [29] for two dimensions. In [30] a hybrid asymptotic-numerical method is employed to analyze the linear stability and slow dynamics of multi-spot patterns of the 3-D Schnakenberg model. Another well-known activator-substrate model is the Gray-Scott model [31, 32], and much theoretical work has been done to analyze the dynamics and instabilities of spike solutions. For example, pattern formation and stability of spike patterns for $D = O(1)$ have been studied in [33, 34, 35, 36], and slow dynamics of quasi-equilibrium spike patterns have been studied in [37, 38, 39].

There have been many studies on extensions of dynamical systems. For example, reaction-diffusion systems are usually studied for coefficients that are constant in space; however, it's more realistic to consider spatially varying coefficients in reaction kinetics, which is referred to as precursor gradients. It is shown in [17] that the asymmetric spike patterns in the GM model with constant coefficients are always unstable with respect to small eigenvalues. While in [40] it turns out that precursor gradient can lead to the existence of stable, asymmetric, two-spike patterns. Moreover, large scale spike density distribution for the Gierer-Meinhardt model with precursor is considered in [41].

1.2 Brief introduction of related models in the thesis

1.2.1 History of SIR epidemic model

Mathematical modeling of infectious diseases began in the early 20th century with the pioneering work of William Hamer [42] and Ronald Ross [43]. In 1927, Kermack

and McKendrick proposed the first epidemic model which is known as the SIR model [44]. This model was successful in predicting the behavior of outbreaks very similar to that observed in many recorded epidemics [45, 46].

There are many extensions of the SIR model, such as SEIR and SIRS model. In the SIRS model, the population is divided into three disjoint classes: susceptible (S), infected (I), and recovered (R), where susceptibles can be infected by those already infected and subsequently recover, and recovered class are immune to the disease but lose immunity over time. These assumptions are modelled using the following system of ODEs:

$$\begin{cases} S_t = -\beta SI + \gamma R, \\ I_t = \beta SI - \nu I, \\ R_t = \nu I - \gamma R, \end{cases} \tag{1.7}$$

where β is the infection rate, ν is the recovery rate, and γ is the rate of immunity loss. Note that the total population $N = S + I + R$ is a constant, this can be verified by adding together the three equations in (1.7), and integrating in terms of t. Kermack and McKendrick's work has motivated the use of mathematics in the study of epidemiology [47, 48, 49].

While spatially homogeneous dynamics are by now well understood, modelling spatial interactions is still an active area of research. In recent decades, numerous methodologies have been used to describe spatial interactions. This includes the use of cellular automata [50, 51], metapopulations [52, 53, 54], networks [55, 56] and partial diffusion equations [57, 58]. Generally speaking, incorporating spatial structure leads to very rich dynamics in epidemic models, such as the formation of disease hot spots.

1.2.2 History of Gierer-Meinhardt model

The Gierer-Meinhardt (GM) model was first proposed in [2] to model head formation in the hydra. It has the following non-dimensional form:

$$\begin{cases} u_t = \varepsilon^2 \Delta u - u + \frac{u^p}{v^q}, \quad x \in \Omega, \quad t > 0, \\ \tau v_t = \Delta v - v + \frac{u^r}{v^s}, \quad x \in \Omega, \quad t > 0, \\ \partial_n u = \partial_n v = 0, \quad x \in \partial\Omega. \end{cases} \tag{1.8}$$

Here Ω is a bounded domain, u and v represent the activator and the inhibitor concentrations, ε^2 is the diffusion rate of the activator u, τ is the reaction-time constant,

∂_n denotes the outward normal derivative, and the exponents (p, q, r, s) are assumed to satisfy

$$p > 1, q \geq 1, r > 0, s \geq 0, \frac{p-1}{q} < \frac{r}{s+1}.$$

The GM model has been widely used to model localization processes in nature, such as cell differentiation and morphogenesis [59, 60], biological pattern formation [61], and the formation of sea-shell patterns [62]. Many variants of this model have been proposed and studied numerically in [61]. These models involve additional chemical species, saturation effects, etc. The model (1.8) is the simplest model in this hierarchy.

The most interesting phenomenon associated with GM model is the existence of stable spikes and stripes. There has been a large literature on the stability of localized 1-D spike solutions to the GM model (1.8) [63, 64, 65, 3, 66, 22, 67]. For 2-D spatial domain, there are only a few analytical results characterizing stability and dynamics of spot patterns, such as [20, 68, 19, 21, 24].

1.2.3 History of Klausmeier model of vegetation

In the semiarid regions, where water resource is limited, it is hard for the vegetation cover to maintain homogeneity, which may lead to self-organized vegetation patterns. This phenomenon is well-known to occur in many parts of the world, such as Africa [69], Australia [70], and the U.S. [71]. In recent decades, vegetation pattern formation has aroused widespread interests of ecologists and mathematicians [72, 73, 74].

Many studies suggest that the formation of vegetation patterns in semi-arid regions results from feedback between biomass and water resource [75, 76, 77, 74, 78]. Based on this mechanism, a great number of mathematical models have been established. One of the most widely used models is proposed by Klausmeier [5], and many models developed later can be considered as modified versions of the Klausmeier model [79, 80, 81]. In dimensionless form, the Klausmeier model contains the following equations:

$$\begin{cases} \underbrace{\dfrac{\partial n}{\partial t}}_{\text{rate of plants}} = \underbrace{\delta \dfrac{\partial^2 n}{\partial x^2}}_{\text{diffusion}} + \underbrace{n^2 w}_{\text{water intake}} - \underbrace{n}_{\text{plant death}}, \\ \underbrace{b\dfrac{\partial w}{\partial t}}_{\text{rate of water}} = \underbrace{c\dfrac{\partial w}{\partial x}}_{\text{flow downhill}} + \underbrace{a}_{\text{precipitation}} - \underbrace{w}_{\text{evaporation}} - \underbrace{n^2 w}_{\text{plant intake}} + \underbrace{d\dfrac{\partial^2 w}{\partial x^2}}_{\text{diffusion}}, \end{cases} \tag{1.9}$$

where $n(x,t)$ and $w(x,t)$ denote plant density and soil water concentration respectively. The parameter a represents the precipitation rate. Parameter b represents the differing timescales in changes in water level (in days, say) versus those in plant density (in months).

There has been some previous work on the analysis of the Klausmeier model. In a collection of articles [82, 83, 84, 85, 86], the behavior of stripe solutions to (1.9) has been studied in various parameter regimes. In [87], system (1.9) was extended by adding the diffusion term of water component w (typically water is assumed to diffuse at a faster rate than that of the vegetation component), which is called the generalized Klausmeier–Gray–Scott model. In [6], a modified Klausmeier–Gray–Scott model was studied and it was shown that the speed of precipitation changes can induce a delay in bifurcation from homogeneous equilibrium to non-homogeneous patterns. If the drift speed is sufficiently small, there is enough time for the spatial perturbations to grow, and the system is able to transition to the patterned state. This state extends beyond the tipping point. However, if the drift speed is too large, the perturbations may not have enough time to grow before the tipping point is reached. If this happens, the tipping point will be activated before the system can transition to the patterned state. In this case the plant population crashes to zero, resulting in rapid desertification.

1.2.4 History of Schnackenberg model

The Schnakenberg model was first proposed in [10] and has many applications involving pattern formations in biology [88, 89]. This system describes an autocatalytic chemical reaction between two chemical products U, V and two sources A and B as follows:

$$U \rightleftharpoons A, \quad B \longrightarrow V, \quad 2U + V \longrightarrow 3U.$$

Applying the law of mass action, one can obtain the following system of reaction-diffusion equations:

$$\begin{cases} u_t = a - u + u^2 v + d_1 u_{xx}, & -L < x < L, \quad t > 0, \\ v_t = b - u^2 v + d_2 v_{xx}, & -L < x < L, \quad t > 0, \\ u_x(\pm L, t) = v_x(\pm L, t) = 0. \end{cases} \tag{1.10}$$

Here u and v represent the activator and the inhibitor concentration, respectively, and the parameters $a, b > 0$ are the respective constant concentrations of A and B.

Because of its algebraic simplicity, the Schnakenberg model has been used by many people as an exemplifying reaction–diffusion system to study spatio-temporal pattern formation. On a one-dimensional interval, the existence and stability of multi-interior spike solutions have been established in both symmetric case [28] and asymmetric case [27]. In a two-dimensional domain, the existence and dynamical behavior of multi-spot solutions have been shown in [29, 90]. More recently, the existence, linear stability, and slow dynamics of localized quasi-equilibrium multi-spot patterns are analyzed in [30] on a finite three-dimensional domain. In [91], the Schnakenberg model was extended to a three-component activator-substrate-inhibitor reaction-diffusion system and new oscillatory dynamics are presented and analyzed.

1.3 Main contributions and comparison to previous work

There have been many studies in dynamics and linear stability analysis with localized patterns, especially on one-dimensional intervals. However, most of them are concentrated in deterministic two-component reaction-diffusion systems. By contrast, the models studied in this thesis are extended to three-component systems or stochastic models. These models introduce several new phenomena which have not been seen in previous work. By analyzing the dynamics and stability of the spike patterns in these models, we link our results to the applications and explain the phenomena in nature.

While the various ODE systems of SIRS model are well-studied, much less work has been done on PDE systems. The first novel result presented in this thesis is the existence of K-spike patterns and several instability mechanisms in the SIRS model with spatial diffusion and nonlinear incidence rates are considered. The results have been published in [92].

The second new result presented in this thesis is the effect of noise on the dynamics of a single spike in the GM model. While the behavior of single spike has been well studied in previous work [3, 34], there are many new phenomena that occur when the spatio-temporal noise is added to the system. These new phenomena have no counterpart with previous work on GM model. This work has been published in [93].

In [94] we study the model for two-plant species (1.3), with competition for a common resource (water). This model is based on the well-known Klausmeier model

of vegetation patterns. We have shown that in the water-constrained regime where spike patterns exist, the two species can co-exist. However, as the precipitation rate decreases, the "frugal" plant is more robust and can out-compete the more "thirsty" plant, leading to the death of thirsty plants and survival of the more frugal plant.

Finally, the thesis includes work from [95], where we study the modified Schnackenberg model. Here, the new result is the existence of single-spike patterns on an infinite domain with the introduction of non-zero activator feed rate. In this case, the outer region for u no longer decays to zero, which is the case in the "classical" Schnakenberg model with $a = 0$, and this leads to a nonlinear outer problem.

1.4 Objectives and Outline

We now present the main goals of this thesis and an overview of the remainder of the chapters. The conventional Turing-type stability analysis shown in § 1.1 leads to the determination of conditions for which spatially uniform steady-state solutions bifurcate to spatially nonuniform solutions. These instabilities have been shown to yield spike-type solutions in semi-strong reaction-diffusion systems. However, this analysis can say nothing about the stability and dynamics of the spike solutions. The main goal of this thesis is to use the method of matched asymptotic expansions to study these spike solutions, which are far from homogeneous steady states.

In chapter 2, we study spatially-localized outbreaks for the SIRS model with spatial diffusion and nonlinear incidence rates. In § 2.1 we show that for a small diffusion rate for the infected class D_I, the infected population tends to be highly localized at certain points inside the domain, forming K spikes. A linearization about this solution leads to a non-local eigenvalue problem which is studied in § 2.2. We then study three distinct destabilization mechanisms, as well as a transition from localized spikes to plateau solutions. Two of the instabilities studied in § 2.3 are due to coarsening (spike death) and self-replication (spike birth), and have well-known analogues in other reaction-diffusion systems such as the Schnakenberg model. The third transition is when a single spike becomes unstable and moves to the boundary. This instability is studied in § 2.4.1 and § 2.4.2. In all cases, the stability thresholds are computed asymptotically and are verified by numerical experiments. In § 2.4.3 we show that the spike solution can transit into a plateau-type solution when the

diffusion rates of recovered and susceptible class are sufficiently small. The material in this chapter is published in [92].

In chapter 3, we study the effect of noise on the dynamics of a single spike for the classical Gierer-Meinhardt model on a finite interval $[-L, L]$. When spatio-temporal noise is introduced in the equation for the activator, we derive in § 3.1 a stochastic ODE that describes the motion of a single spike on a slow time scale. Then in § 3.2, we look for the long-term density distribution for spike positions, which is obtained by computing the steady state via the corresponding Fokker-Plank PDE. For sufficiently small noise level, the spike performs random fluctuations near the center of the domain. For even larger noise levels, the spike starts to undergo large excursions that eventually collide with the domain boundary and temporarily trap the spike there. In § 3.3, we reformulate this problem in terms of mean first passage time (MFPT), and derive the expected time for the spike to collide with the boundary. The work has been published in [93].

In chapter 4, we analyze the stability and dynamics of multi-spike solutions in the "two-species vegetation model". In § 4.1, we construct the non-trivial steady state which contains two types of spikes, u_1 and u_2. With different water intake rates, the two types of spikes have different heights and radius. Then we analyze the stability of the N-spike equilibrium with respect to the large eigenvalues by deriving the corresponding nonlocal eigenvalue problem (NLEP), and with respect to the small eigenvalues by looking at asymmetric branches in § 4.2. We then show that the instability due to small eigenvalues is the dominant instability. In § 4.3 we use numerics to explore what happens in the high-precipitation regime of large a, and we conclude with some open questions. The work has been published in [94].

In chapter 5, we study the stability of single-spike patterns in modified Schnackenberg model in the semi-strong regime on bounded and unbounded domain. First, we construct the steady state in § 5.1 with finite and infinite L. Then we derive the corresponding nonlocal eigenvalue problem in § 5.2 to study the Hopf instability of the single spike under the case $\tau = 0$ and $\tau \neq 0$. These results have been published in section 3 and section 4 of the paper [95].

Finally, in chapter 6, we summarize the main results and contributions of this thesis and identify several open problems for future study.

Chapter 2

Localized outbreaks in SIRS model with diffusion

In this chapter we study spatially localized outbreaks for the SIRS (1.7) model with spatial dispersion. As will be shown below, such outbreaks can occur when the infection rate β increases with the number of infected individuals. Here, we will assume that β is proportional to I, and we model spatial dispersion using diffusion. This results in the following system,

$$\begin{cases} S_t = D_S S_{xx} - \chi S I^2 + \gamma R, \\ I_t = D_I I_{xx} + \chi S I^2 - \nu I, \\ R_t = D_R R_{xx} + \nu I - \gamma R. \end{cases} \tag{2.1}$$

Here D_S, D_I, D_R are diffusion coefficients of each class of population and χI is the rate of infection. We study this epidemic system on a 1-D interval $[-L, L]$ with Neumann boundary conditions, so that $S_x = I_x = R_x = 0$ at $x = \pm L$. For simplicity, we also assumed the timescale of infection and recovery is much shorter than people's average life span, so birth and death rates for each class are neglected.

The second key assumption we make is that the infected class I diffuses more slowly than others. There are two scenarios where this is biologically plausible. The first scenario, common in many species, is that the disease itself reduces the species mobility. A second scenario, applicable to humans, is an intentional quarantine policy to limit the spread of infection. Such a policy is well known to be effective in controlling disease outbreaks and is often used a first-line defense against quickly-spreading infections.

We therefore write $D_I = \varepsilon^2$ where ε is small. By further rescaling [1], we may set $\chi = 1, \nu = 1$. This leads to the following singularly perturbed reaction diffusion

[1] Let $t = \frac{\hat{t}}{\nu}, S = \sqrt{\frac{\nu}{\chi}}\hat{S}, I = \sqrt{\frac{\nu}{\chi}}\hat{I}, R = \sqrt{\frac{\nu}{\chi}}\hat{R}$ and define new parameters by $\gamma = \nu\hat{\gamma}, D_S = \nu\hat{D_S}, D_I = \nu\varepsilon^2, D_R = \nu\hat{D_R}$. Upon dropping the hats, this yields (2.2).

system:

$$\begin{cases} S_t = D_S S_{xx} - SI^2 + \gamma R, \\ I_t = \varepsilon^2 I_{xx} + SI^2 - I, \\ R_t = D_R R_{xx} + I - \gamma R. \end{cases} \tag{2.2}$$

Under these assumptions, this system has localized disease concentrations corresponding to spike-type solutions. Such spike patterns have been studied in great detail since the 1990's in simpler reaction-diffusion systems consisting of two components, such as Gierer-Meinhardt system, Gray-Scott model, Schnakenberg model and Keller-Segel model and its variants. We refer the readers to [4, 63, 3, 96, 97, 98, 64, 36, 99, 100] and references therein. The introduction of a third component leads to interesting new phenomena not present in two-component reaction-diffusion systems [101].

Simulations and analysis show that the behavior of the system is highly dependent on the diffusion rate of the recovered class D_R, relative to the diffusion rate of infected class, ε^2. We isolate two distinct regimes: either $D_R \gg O(\varepsilon^2)$ or $D_R \leq O(\varepsilon^2)$.

Depending on the regime, several different types of instability may occur. In § 2.1, § 2.2, § 2.3, we study the regime $D_R \gg O(\varepsilon^2)$, where the steady-state population consists of K hot-spots of disease, uniformly distributed inside the interval $[-L, L]$. Depending on system parameters, the K-spike steady state can undergo two types of instabilities. The first type, analyzed in Section § 2.3.1 is referred to as *spike competition instability*. As a result of such an instability, some of the hot-spots are "absorbed" by others, resulting in fewer hot-spots. The second type of instability, studied in Section § 2.3.2 is referred to as *self-replication instability*, whereby a spike splits into two, resulting in more spikes. These instabilities are illustrated in Figure 2.1. Figure 2.1(a) shows 8 spikes that gradually coarsen into 2 as D_S is gradually increased. On the other hand, with one-spike equilibrium as initial condition, replication occurs and more spikes appear as we gradually decrease D_S. This is shown in Figure 2.1(b). We derive explicit thresholds for D_S such that the spike competition occurs when $D_S > D_{SK}^{com}$, $K \geq 2$; and self-replication instability occurs when $D_S < D_{SK}^{rep}$, $K \geq 1$. Formulas for D_{SK}^{com} and D_{SK}^{rep} are given in Section § 2.3.

In Section § 2.4 we study the other regime where D_R is small: $D_R \leq O(\varepsilon^2)$. In this case, a single spike can become unstable, and depending on other parameters, two

phenomena can occur. If D_R is sufficiently small, a single spike moves to the boundary (depending on how big D_S is), as illustrated in Figure 2.2. This phenomenon is studied in Section § 2.4.2. On the other hand, when both D_R and D_S are small, the spike "fattens up" and becomes a mesa-type pattern, i.e., a contiguous region of high concentration of disease connected via a sharp interface to a region of low concentration. Numerically we observe two types of inhomogeneous equilibrium depending on the value of D_S and an example of such a steady state pattern is shown in Figure 2.3. Spike-type solution exists for sufficiently large D_S, but transition to interface-type patterns for small D_S. This process is illustrated in Figure 2.3(left). Interface patterns are studied in Section § 2.4.3.

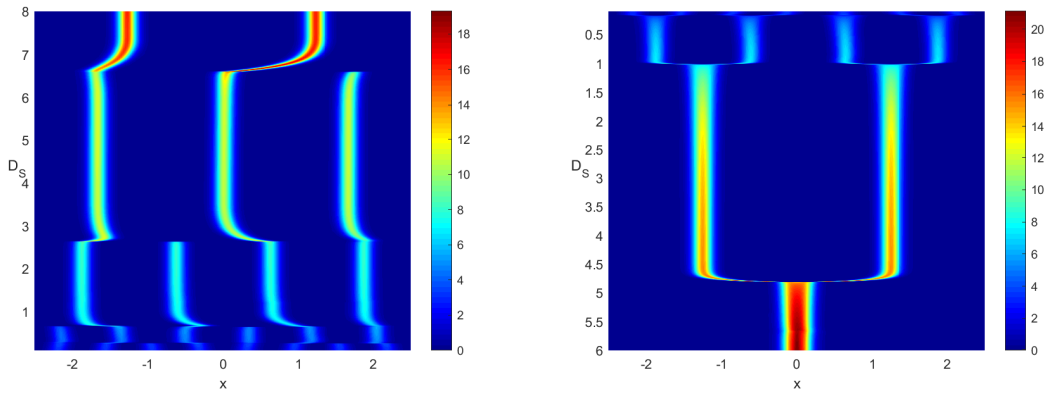

(a) (b)

Figure 2.1: Instabilities of steady state spike solutions induced by slowly increasing D_S or decreasing D_S. Here $D_R = 1, L = 2.5, \varepsilon = 0.05, N = 15$ and $\gamma = 1$. Left: Coarsening (competition) instability when D_S is increased ($D_s = 1 + 10^{-5}t$). Color plot of I is shown in each case. Right: Self-replication instability when D_S is slowly decreased ($D_s = 6 - 10^{-5}t$).

2.1 Symmetric spike equilibrium solutions

We begin by calculating the equilibrium spike solution of system (2.1) using matched asymptotic methods. In particular, we start by constructing single-spike solutions, then we can apply the "gluing" technique to construct K-spike symmetric equilibrium solutions.

To do this, we first consider a one-spike solution on the interval $|x| < L$ centered

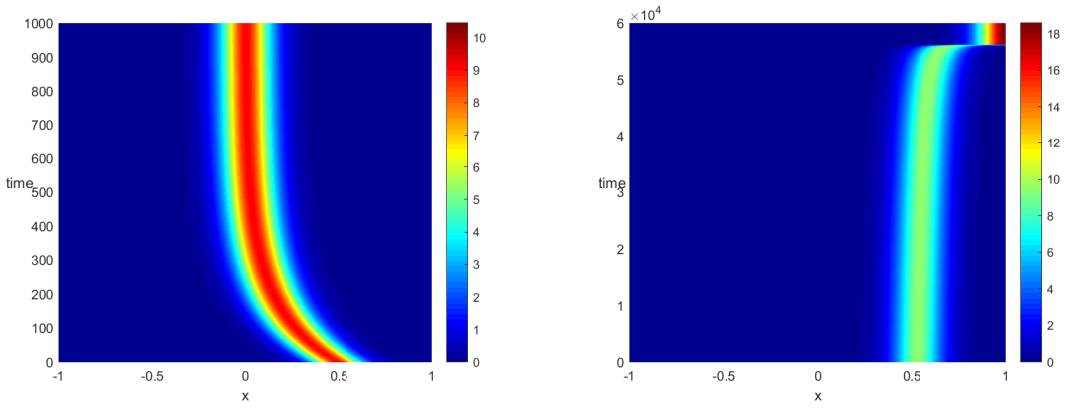

(a) $D_R = 1$ (b) $D_R = 0.0036$

Figure 2.2: Stable and unstable motion of a single spike. Here, D_R is as indicated while other parameters are fixed at $D_S = 5, L = 1, \varepsilon = 0.06, N = 5$ and $\gamma = 1$. In (a), one-spike equilibrium moves to the center, which shows that the center spike is stable. In (b) the spike moves to boundary instead of moving to center, showing that a single spike is unstable.

at x_0. The extent of the spike is of $O(\varepsilon)$, we therefore introduce the inner variable

$$y = \frac{x - x_0}{\varepsilon}. \tag{2.3}$$

In the inner region the equilibrium solution of (2.4) satisfies

$$\begin{cases} S_{yy} - \frac{\varepsilon^2}{D_S} SI^2 + \frac{\varepsilon^2}{D_S}\gamma R = 0, \\ I_{yy} + SI^2 - I = 0, \\ R_{yy} + \frac{\varepsilon^2}{D_R} I - \frac{\varepsilon^2}{D_R}\gamma R = 0. \end{cases} \tag{2.4}$$

We then expand S, I, R as

$$\begin{aligned} S &= S_0 + \varepsilon S_1 + O(\varepsilon^2), \\ I &= I_0 + \varepsilon I_1 + O(\varepsilon^2), \\ R &= R_0 + \varepsilon R_1 + O(\varepsilon^2). \end{aligned} \tag{2.5}$$

Upon substituting (2.5) into (2.4) and collecting higher-order terms in ε, we obtain, to leading order,

$$\begin{cases} S_{0yy} = 0, \\ I_{0yy} + S_0 I_0^2 - I_0 = 0, \\ R_{0yy} = 0. \end{cases} \tag{2.6}$$

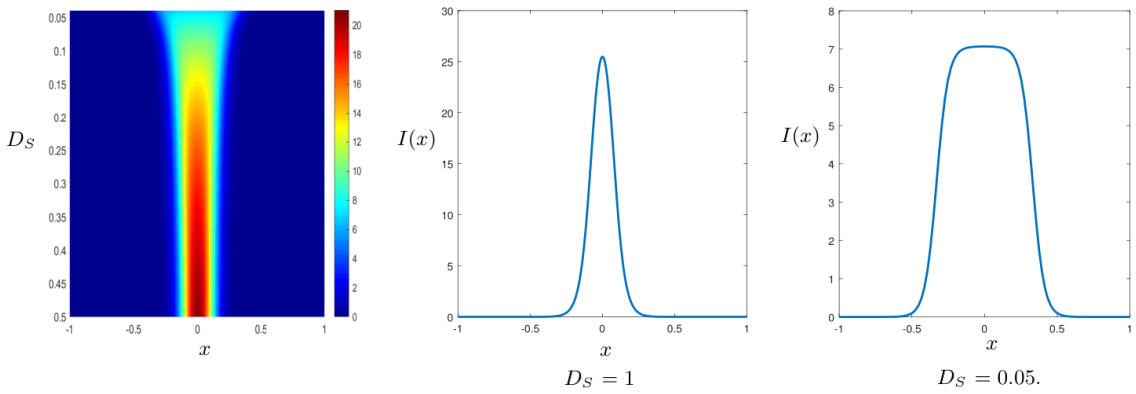

Figure 2.3: Transition from spike to mesa when $D_R = 0, \varepsilon = 0.04, N = 10, L = 1, \gamma = 1$ with D_S as a control parameter. Left: D_S is gradually decreased from 0.5 to 0.05. Middle, Right: Profile of $I(x)$ for D_S as indicated.

This shows that S_0 and R_0 are constants that are to be determined. We then rescale

$$I_0 = \frac{1}{S_0} w(y), \tag{2.7}$$

where so that w satisfies the well-known ground-state,

$$w'' - w + w^2 = 0, \quad w \to 0 \text{ as } y \to \pm\infty, \tag{2.8}$$

whose explicit solution is given by

$$w(y) = \frac{3}{2}\text{sech}^2\left(\frac{y}{2}\right). \tag{2.9}$$

To determine S_0 and R_0, we must match the inner and the outer region. Since S is localized near $x = x_0$, the terms involving S in (2.2) can be represented as delta functions. Therefore in the outer region we approximate

$$I \sim \left(\int_{-L}^{L} I dx\right) \delta(x - x_0), SI^2 \sim \left(\int_{-L}^{L} SI^2 dx\right) \delta(x - x_0).$$

We further estimate $\left(\int_{-L}^{L} I dx\right) \sim \frac{1}{S_0}\varepsilon \int_{-\infty}^{\infty} w dy \sim 6\varepsilon/S_0$ and similarly, $\int_{-L}^{L} SI^2 dx \sim 6\varepsilon/S_0$, so that S, R in the outer region satisfy

$$\begin{aligned} D_S S_{xx} + \gamma R &= 6\varepsilon/S_0 \delta(x - x_0), \\ D_R R_{xx} - \gamma R &= -6\varepsilon/S_0 \delta(x - x_0). \end{aligned} \tag{2.10}$$

To solve (2.10), we introduce the modified Green's function $G(x;x_0)$, which satisfies

$$\begin{cases} G_{xx} - \frac{\gamma}{D_R} G = -\delta(x;x_0), \\ G_x(x_0^+) - G_x(x_0^-) = -1, \\ G_x(\pm L) = 0. \end{cases} \tag{2.11}$$

A simple calculation gives

$$G(x;x_0) = \begin{cases} \frac{\cosh\left(\sqrt{\frac{\gamma}{D_R}}(x+L)\right)\cosh\left(\sqrt{\frac{\gamma}{D_R}}(x_0-L)\right)}{\sqrt{\frac{\gamma}{D_R}}\sinh(2\sqrt{\frac{\gamma}{D_R}}L)}, & -L < x < x_0 \\ \frac{\cosh\left(\sqrt{\frac{\gamma}{D_R}}(x_0+L)\right)\cosh\left(\sqrt{\frac{\gamma}{D_R}}(x-L)\right)}{\sqrt{\frac{\gamma}{D_R}}\sinh(2\sqrt{\frac{\gamma}{D_R}}L)}, & x_0 < x < L. \end{cases} \tag{2.12}$$

The solution to (2.10) is then given by

$$R(x) = \frac{6\varepsilon}{S_0 D_R} G(x;x_0), \tag{2.13}$$

and

$$S(x) = -\frac{D_R}{D_S} R(x) + \frac{D_R}{D_S} R_0 + S_0, \tag{2.14}$$

where $R_0 = \frac{6\varepsilon}{S_0 D_R} G(x_0;x_0)$ and S_0 is to be determined. To find S_0, we use the conservation of mass. Let N be the total population, so that

$$N \equiv \int_{-L}^{L} (S + I + R)dx. \tag{2.15}$$

Note that by adding three equations in (2.2) and integrating over the domain, N is independent of time. We will also take

$$N = 2N_0 L, \tag{2.16}$$

where N_0 is an arbitrary constant depending on the initial conditions, so that N scales with domain size; N_0 can be thought of an average density.

We now substitute (2.7), (2.13), and (2.14) into the mass conservation condition (2.15, 2.16) to obtain that

$$S_0^2 - N_0 S_0 + E = 0, \tag{2.17}$$

where

$$E = \frac{3\varepsilon}{L}\left(1 + \frac{1}{\gamma} - \frac{D_R}{\gamma D_S} + 2\sqrt{\frac{D_R}{\gamma}}\frac{L}{D_S}\frac{\cosh(\sqrt{\frac{\gamma}{D_R}}(x_0+L))\cosh(\sqrt{\frac{\gamma}{D_R}}(x_0-L))}{\sinh(2\sqrt{\frac{\gamma}{D_R}}L)}\right). \tag{2.18}$$

Solving (2.17) we get two roots when $N_0^2 - 4E > 0$. Asymptotically in ε, they are

$$S_{0-} \sim \frac{E}{N_0}, \tag{2.19}$$

which is of $O(\varepsilon)$ and

$$S_{0+} \sim N_0, \tag{2.20}$$

which is of $O(1)$. Plots of these two roots are shown in Fig 2.4. The two roots connect at a fold point corresponding to a double root of (2.17). We now summarize our first result:

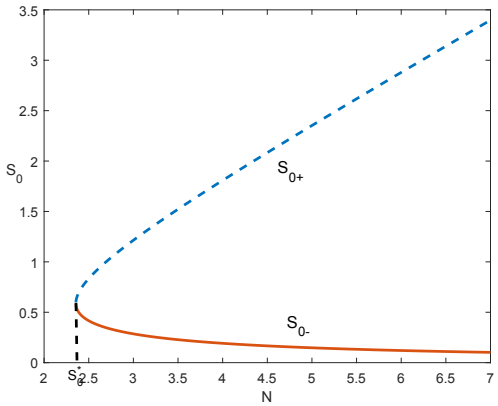

Figure 2.4: Plot of two roots to (2.17) vs. total population N. Here $\varepsilon = 0.05, L = 1, D_R = 1, D_S = 1$ and $\gamma = 1$. The dashed curve denotes S_{0+} and the solid curve denotes S_{0-}. S_0^* is the fold point where (2.17) has double root.

Result 2.1.1 *With $D_I = \varepsilon^2$ and $0 < \varepsilon \ll 1$, the SIRS system (2.2) has the following single-spike steady state:*

$$\begin{aligned} S(x) &\sim -\frac{6\varepsilon}{S_0 D_S} G(x; x_0) + \frac{6\varepsilon}{S_0 D_S} G(x_0; x_0) + S_0, \\ I(x) &\sim \frac{1}{S_0} w\left(\frac{x - x_0}{\varepsilon}\right), \\ R(x) &\sim \frac{6\varepsilon}{S_0 D_R} G(x; x_0), \end{aligned} \tag{2.21}$$

where $G(x; x_0)$ is given by (2.12), $w(y) = \frac{3}{2}\operatorname{sech}^2(\frac{y}{2})$ and S_0 is a constant determined by the total population mass as given in (2.19, 2.20).

2.2 Nonlocal eigenvalue problem

We now study the stability of one-spike solution. We first linearize around the steady state by taking

$$\begin{aligned} S(x,t) &= S(x) + e^{\lambda t}\varphi(x), \\ I(x,t) &= I(x) + e^{\lambda t}\psi(x), \\ R(x,t) &= R(x) + e^{\lambda t}\xi(x). \end{aligned}$$

Assuming $|\varphi|, |\psi|, |\xi| \ll O(1)$ we obtain the linearized problem

$$\begin{cases} \lambda\varphi = D_S\varphi_{xx} - I_0^2\varphi - 2S_0I_0\psi + \gamma\xi, \\ \lambda\psi = \varepsilon^2\psi_{xx} + I_0^2\varphi + (2S_0I_0 - 1)\,\psi, \\ \lambda\xi = D_R\xi_{xx} + \psi - \gamma\xi. \end{cases} \tag{2.22}$$

In the inner region, we let $y = \frac{x-x_0}{\varepsilon}$, where x_0 is the spike position. To leading order, we then obtain $\varphi_{yy} \sim 0$ so that $\varphi(x) \sim \varphi_0$ is a constant to be determined. The equation for ψ is

$$\lambda\psi = \psi_{yy} - \psi + 2w(y)\psi + I_0^2\varphi_0. \tag{2.23}$$

In the outer region, we approximate

$$\begin{cases} D_S\varphi_{xx} - \lambda\varphi + \gamma\xi = c_1\delta(x;x_0), \\ D_R\xi_{xx} - (\gamma+\lambda)\xi = c_2\delta(x;x_0), \end{cases} \tag{2.24}$$

where

$$c_1 = \left(\varphi_0\int I_0^2dx + 2S_0\int I_0\psi dx\right), c_2 = -\int\psi dx. \tag{2.25}$$

We write

$$\xi(x;x_0) = -\frac{c_2}{D_R}G\left(x;x_0,\sqrt{\frac{\gamma+\lambda}{D_R}}\right), \tag{2.26}$$

where $G(x;x_0,\mu)$ is the Green's function that satisfies

$$\begin{cases} G_{xx} - \mu^2G = -\delta(x;x_0), \\ G_x(\pm L) = 0, \end{cases} \tag{2.27}$$

and is explicitly given by

$$G = \frac{1}{\mu\sinh(2\mu L)}\begin{cases} \cosh\left(\mu(x+L)\right)\cosh\left(\mu(x_0-L)\right), & -L < x < x_0 \\ \cosh\left(\mu(x_0+L)\right)\cosh\left(\mu(x-L)\right), & x_0 < x < L. \end{cases}. \tag{2.28}$$

To solve for φ, we make a change of variables. Let

$$\varphi = \frac{D_R\gamma}{\lambda(D_R - D_S) - \gamma D_S}\xi + \varphi_h. \tag{2.29}$$

Then φ_h satisfies:

$$D_S\varphi_{hxx} - \lambda\varphi_h = \left(c_1 - \frac{\gamma c_2}{\lambda(D_R - D_S) - \gamma D_S}\right)\delta(x; x_0)$$

so that

$$\varphi_h = -\frac{1}{D_S}\left(c_1 - \frac{\gamma c_2}{\lambda(D_R - D_S) - \gamma D_S}\right) G\left(x; x_0; \sqrt{\frac{\lambda}{D_s}}\right).$$

Therefore we estimate

$$\begin{aligned}\varphi_0 = \varphi(x_0) \sim -c_2\frac{\gamma}{\lambda(D_R - D_S) - \gamma D_S} G\left(x_0; x_0, \sqrt{\frac{\gamma+\lambda}{D_R}}\right) \\ - \frac{1}{D_S}\left(c_1 - \frac{\gamma c_2}{\lambda(D_R - D_S) - \gamma D_S}\right) G\left(x_0; x_0; \sqrt{\frac{\lambda}{D_s}}\right)\end{aligned}$$

and

$$c_1 = \varepsilon\left(\frac{\varphi_0}{S_0^2}\int w^2 dy + 2\int w\psi dy\right); \quad c_2 = -\varepsilon\int \psi dy. \tag{2.30}$$

After some algebra, this leads to the following non-local eigenvalue problem (NLEP),

$$(L_0 - \lambda)\psi = w^2\frac{2}{\int_{-\infty}^{\infty} w^2 dy - (\lambda+1)\frac{S_0^2}{\varepsilon P}}\int_{-\infty}^{\infty} w\psi dy, \tag{2.31}$$

$$\text{where } L_0\psi = \psi_{yy} - \psi + 2w\psi, \tag{2.32}$$

and where

$$\begin{aligned}P = \frac{\gamma\sqrt{\frac{D_R}{\lambda+\gamma}}}{\lambda(D_R - D_S) - \gamma D_S}\frac{\cosh\left(\sqrt{\frac{\lambda+\gamma}{D_R}}(x_0+L)\right)\cosh\left(\sqrt{\frac{\lambda+\gamma}{D_R}}(x_0-L)\right)}{\sinh\left(2\sqrt{\frac{\lambda+\gamma}{D_R}}L\right)} \\ - \frac{\lambda+1+\frac{D_S\gamma}{\lambda(D_R-D_S)-\gamma D_S}}{\sqrt{\lambda D_S}}\frac{\cosh\left(\sqrt{\frac{\gamma}{D_S}}(x_0+L)\right)\cosh\left(\sqrt{\frac{\gamma}{D_S}}(x_0-L)\right)}{\sinh\left(2\sqrt{\frac{\gamma}{D_S}}L\right)}.\end{aligned} \tag{2.33}$$

For the special case when $x_0 = 0$, this expression simplifies to

$$P(\lambda) = \frac{\gamma\sqrt{\frac{D_R}{\lambda+\gamma}}}{\lambda(D_R - D_S) - \gamma D_S}\frac{\coth\left(\sqrt{\frac{\lambda+\gamma}{D_R}}L\right)}{2} - \frac{\lambda+1+\frac{D_S\gamma}{\lambda(D_R-D_S)-\gamma D_S}}{\sqrt{\lambda D_S}}\frac{\coth\left(\sqrt{\frac{\gamma}{D_S}}L\right)}{2}. \tag{2.34}$$

In general, the NLEP problem (2.31) is difficult to tackle since P has such a complicated dependence on λ. However there are two cases for which stability of (2.31) is well established: namely, large or small $\frac{S_0^2}{\varepsilon}$. Note that S_0 is given by (2.19, 2.20) and has two branches, S_{0+} and S_{0-}, refer to Figure 2.4. Consider the case of large N. Then $\frac{S_{0+}^2}{\varepsilon} \gg 1$, whereas $\frac{S_{0-}^2}{\varepsilon} \ll 1$. In the former case, (2.31) reduces to a *local* eigenvalue problem $(L_0 - \lambda)\psi \sim 0$. This problem is well known to admit a positive eigenvalue $\lambda = 5/4$ so that this branch is unstable. For the latter case ($S_0 = S_{0-}$), the problem (2.31) reduces to the following well-known NLEP problem:

$$\lambda\psi = L_0\psi - 2w^2\frac{\int_{-\infty}^{\infty} w\psi dy}{\int_{-\infty}^{\infty} w^2 dy}, \quad S_0 \sim O(\varepsilon). \tag{2.35}$$

This is well-known to be *stable* as was first proven in [63].

Finally, a lengthy but a straightforward algebraic computation shows that at the fold point where $S_{0+} = S_{0-}$, there is a zero eigenvalue whose corresponding eigenfunction is given by $\psi = w$. This suggests that the entire branch S_{0+} is unstable whereas the entire branch S_{0-} is stable, although the proof of this fact is not in the cards due to the complex structure of $P(\lambda)$. This structure is analogous to the well-known properties of the Grey-Scott model in the low-feed regime [102].

Another approach is to consider the limit of large D_R and/or D_S (so-called shadow limits). We do not observe any additional instabilities of a single spike in this regime so we will not pursue it further here.

2.3 Instability thresholds of Multi-spike equilibrium

In this section we study stability of K-spike patterns in the regime $D_R \gg O(\varepsilon^2)$, where $K \geq 1$. We analyze two types of instabilities, one is referred to as spike competition or coarsening instability, whereby some of the spikes are annihilated if the initial state contains too many spikes. The other is referred to as self replication, whereby a new spike may appear by the process of spike splitting. In this section we derive explicit thresholds for these instabilities.

2.3.1 Coarsening

When there are too many spikes, some of them get absorbed by others. This is known as coarsening or competition instability. To determine the instability threshold for

spike competition, we apply the method in [103, 27] and compute the critical value at which an asymmetric spike pattern bifurcates from symmetric branch. To do this, we consider a single interior spike on the domain $[-l, l]$. Duplicating the domain K times, we obtain K spikes on the domain of size $2L = 2lK$. From (2.14) we have:

$$S(l) = S_0 + \frac{3\varepsilon}{D_S S_0}\sqrt{\frac{D_R}{\gamma}}\left(\frac{1}{\tanh\left(\sqrt{\frac{\gamma}{D_R}}l\right)} - \frac{1}{\sinh\left(\sqrt{\frac{\gamma}{D_R}}l\right)}\right), \tag{2.36}$$

where $S_0 = S_{0-}$ is given in (2.19) with $x_0 = 0$. Plots of $S(l)$ when $D_S = 1$ and $D_S = 3$ are shown in Figure 2.5. The bifurcation point corresponds to the minimum point of the curve $l \to S(l)$. Setting $S'(l) = 0$ then yields the critical stability threshold. Solving for D_S as a function of other parameters, and upon substituting $l = L/K$, we obtain the critical threshold

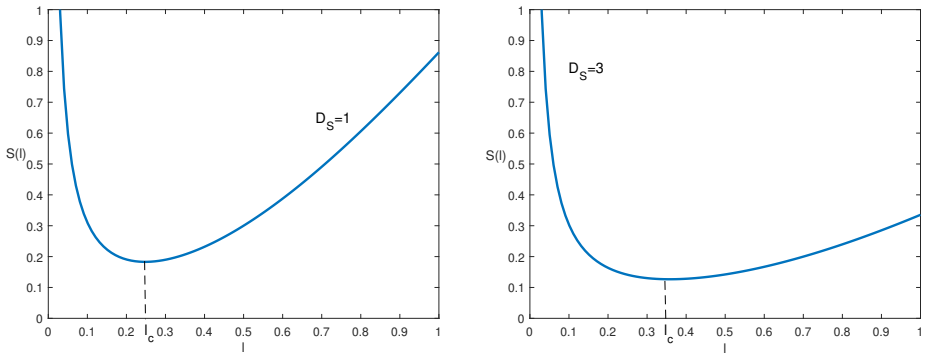

(a) $S(l)$ when $D_S = 1$ (b) $S(l)$ when $D_S = 3$

Figure 2.5: Plots of function $S(l)$ versus l for $D_S = 1$ and $D_S = 3$. Other parameters are fixed and they are: $\varepsilon = 0.02, D_R = 2, \gamma = 1, N_0 = 4$.

$$\begin{aligned} D_{SK}^{com} \sim & \frac{N_0^2\left(\frac{L}{K}\right)^3}{3\varepsilon\left(1+\frac{1}{\gamma}\right)^2}\left(1 - \frac{1}{\tanh^2\left(\sqrt{\frac{\gamma}{D_R}}\frac{L}{K}\right)} + \frac{\cosh\left(\sqrt{\frac{\gamma}{D_R}}\frac{L}{K}\right)}{\sinh^2\left(\sqrt{\frac{\gamma}{D_R}}\frac{L}{K}\right)}\right) \\ & + \frac{N_0^2\left(\frac{L}{K}\right)^2}{3\varepsilon\left(1+\frac{1}{\gamma}\right)^2}\sqrt{\frac{D_R}{\gamma}}\left(\frac{1}{\tanh\left(\sqrt{\frac{\gamma}{D_R}}\frac{L}{K}\right)} - \frac{1}{\sinh\left(\sqrt{\frac{\gamma}{D_R}}\frac{L}{K}\right)}\right). \end{aligned} \tag{2.37}$$

The K-spike solution is unstable and some of the spikes will disappear when $D_S > D_{SK}^{com}$. The plot of D_{SK}^{com} as a function of D_R is shown in Figure 2.6. Note that D_{SK}^{com}

has the following asymptotics as $D_R \to \infty$:

$$D_{SK}^{com} \sim \frac{N_0^2 \left(\frac{L}{K}\right)^3}{3\varepsilon \left(1+\frac{1}{\gamma}\right)^2}, \quad \text{as } D_R \to \infty, \tag{2.38}$$

which is shown in Figure 2.6. We now summarize the following result:

Result 2.3.1 *Consider a K-spike solution for the system (2.2) on an interval of length $2L$ with $K > 1$. Then in the limit of $\varepsilon \to 0$, this solution is stable provided that $D_S < D_{SK}^{com}$, where D_{SK}^{com} is given by (2.37). When $D_S > D_{SK}^{com}$, the K-spike solution becomes unstable due to competition (or coarsening) instability and some of the spikes disappear.*

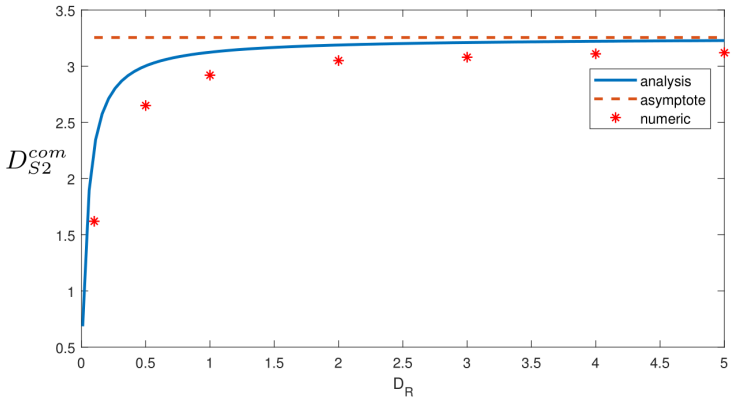

Figure 2.6: Plot of stability threshold D_{S2}^{com} vs. D_R. Here $\varepsilon = 0.02, L = 1, N_0 = 2.5$, and $\gamma = 1$. The solid curve denotes analysis value D_{S2}^{com} obtained by (2.37), and the dashed line is the asymptote of the curve (2.38). The dots are obtained from numerical simulations of the system (2.2) by FlexPDE, and they have good agreement with the analysis. See Appendix A for detailed explanations and the FlexPDE script for simulating (2.2).

2.3.2 Self-replication

Unlike coarsening instability, self-replication is related to disappearance of the single spike equilibrium solution. The mechanism has been studied in detail for the Gray-Scott model [104, 105, 98, 97, 33, 106], and it is similar here. We start by changing variables

$$S(x) = \frac{\varepsilon}{\sqrt{D_S}}\tilde{S}(x), I(x) = \frac{\sqrt{D_S}}{\varepsilon}\tilde{I}(x), x = \varepsilon y, \tag{2.39}$$

so that the system (2.2) transforms to

$$\begin{cases} \frac{\sqrt{D_S}}{\varepsilon}\tilde{S}_{yy} - \frac{\sqrt{D_S}}{\varepsilon}\tilde{S}\tilde{I}^2 + \gamma R = 0, \\ \tilde{I}_{yy} + \tilde{S}\tilde{I}^2 - \tilde{I} = 0, \\ \frac{D_R}{\varepsilon^2}R_{yy} + \frac{\sqrt{D_S}}{\varepsilon}\tilde{I} - \gamma R = 0. \end{cases} \tag{2.40}$$

Next, assume that D_S, D_R are $O(1)$. Then to leading order, in the inner region we obtain the following problem, referred to as the **core problem**,

$$\begin{cases} \tilde{S}_{yy} - \tilde{S}\tilde{I}^2 = 0, \\ \tilde{I}_{yy} + \tilde{S}\tilde{I}^2 - \tilde{I} = 0. \end{cases} \tag{2.41}$$

This core problem is identical to the core problem for both the Grey-Scott model [104, 98, 97, 106], and the Schnakenberg model [100]. Assuming that the spike is symmetric, we define

$$A := \tilde{S}_y(\infty) = \int_0^\infty \tilde{S}\tilde{I}^2 dy. \tag{2.42}$$

By plotting the numerical bifurcation diagram of (2.28), it was found in [98, 106] that the steady state disappears when $A > A_c \approx 1.35$, and this disappearance leads to self-replication. To determine A in terms of the other parameters of the problem, we perform an asymptotic matching to the outer region. We estimate $\int SI^2 dx = \int I dx$ and

$$D_R R_{xx} - \gamma R = -\left(\int I dx\right)\delta(x), \quad D_S S_{xx} + \gamma R = -\left(\int I dx\right)\delta(x).$$

The solution is then given by

$$R(x) = \frac{\left(\int I dx\right)}{D_R} G(x), \tag{2.43}$$

$$S(x) = -\frac{D_R}{D_S}R(x) + \frac{D_R}{D_S}R(0), \tag{2.44}$$

where as before,

$$G(x) = \frac{\sqrt{\frac{D_R}{\gamma}}}{2\sinh\left(\sqrt{\frac{\gamma}{D_R}}l\right)} \begin{cases} \cosh\left(\sqrt{\frac{\gamma}{D_R}}(x+l)\right), & -l < x < 0 \\ \cosh\left(\sqrt{\frac{\gamma}{D_R}}(x-l)\right), & x < x < l. \end{cases} \tag{2.45}$$

We substitute (2.43, 2.44) into the total mass equation (2.15) to obtain that

$$N = 2N_0 l = 2A\sqrt{D_S}\left(1 + \frac{1}{\gamma} - \frac{D_R}{\gamma D_S}\right) + \frac{2Al}{\sqrt{D_S}}\frac{\sqrt{\frac{D_R}{\gamma}}}{\tanh\left(\frac{\gamma}{D_R}l\right)}, \tag{2.46}$$

so that self-replication occurs when

$$A = \frac{N_0 l\sqrt{D_S}}{D_S\left(1+\frac{1}{\gamma}\right) + l\frac{\sqrt{\frac{D_R}{\gamma}}}{\tanh\left(\sqrt{\frac{\gamma}{D_R}}l\right)} - \frac{D_R}{\gamma}} > A_c \approx 1.35. \tag{2.47}$$

Equivalently, we rewrite (2.47) to obtain the following quadratic equation with respect to $\sqrt{D_S}$

$$\left(1+\frac{1}{\gamma}\right)D_S - \frac{N_0 l}{A_c}\sqrt{D_S} + \frac{\sqrt{\frac{D_R}{\gamma}}l}{\tanh\left(\sqrt{\frac{\gamma}{D_R}}l\right)} - \frac{D_R}{\gamma} = 0. \tag{2.48}$$

Therefore replication of one-spike solution occurs when $D_S < D_S^{rep}$, where $\sqrt{D_S^{rep}}$ is the larger root of (2.48). For K spikes on domain $[-L, L]$ with $L = Kl$, this leads to the following result:

Result 2.3.2 *Consider a K-spike solution of the system (2.2) on an interval of length $2L$ with $K \geq 1$. Then in the limit of $\varepsilon \to 0$, this solution is stable provided that $D_S > D_{SK}^{rep}$, where $D_S = D_{SK}^{rep}$ is the root of (2.48), in which $l = \frac{L}{K}$ and $A_c \approx 1.35$ corresponds to the fold point of the problem (2.42).*

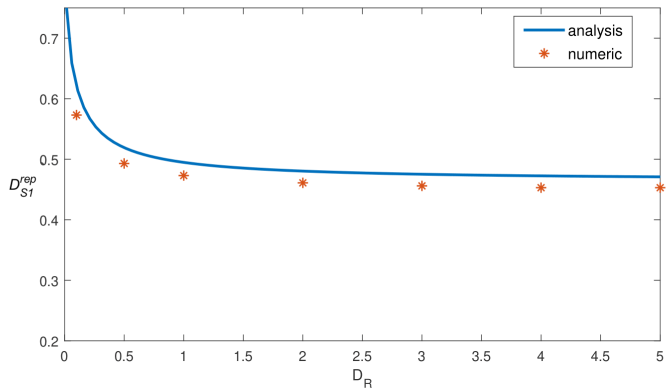

Figure 2.7: Self-replication threshold (Result 2.3.2). Comparison between numerics and analysis. Solid curve is the analytical result given by (2.48). Dots are obtained from numerical simulations of the system (2.2) by FlexPDE. Self-replication is observed as D_S is decreased past the solid curve in the figure. Here $\varepsilon = 0.005, N = 5, L = 1$, and $\gamma = 1$.

Figure 2.7 shows numerical validation of Result 2.3.2. The solid curve denotes the asymptotic curve as given in Result 2.3.2. Above the curve, a single spike is stable.

As D_S is decreased and crosses the curve, self-replication takes place resulting in two spikes. The dots denote numeric simulations in which we look for the self-replication threshold by gradually decreasing D_S until K spikes self-replicate to $K+1$ spikes. See Appendix A for the FlexPDE script for simulating (2.2). Good agreement is observed between numerics and asymptotics.

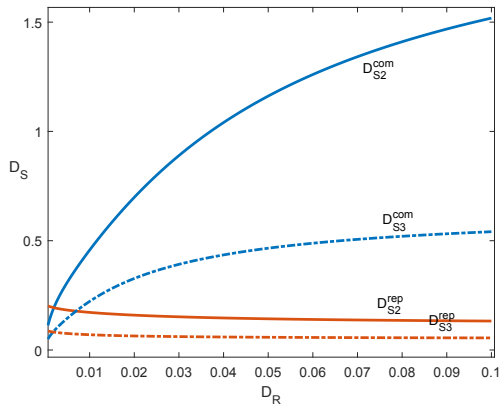

Figure 2.8: Bifurcation diagram of K-spike patterns for $K = 2, 3$. The region between solid curves is the stable region for 2-spike patterns, and the region between dashed curves is the stable region for 3-spike patterns. Above the regions spike competition instability occurs, below the region, self replication instability occurs. Here $\varepsilon = 0.03, N_0 = 2.5, L = 1, \gamma = 1$.

For a fixed D_R and a given number of spikes K, we have derived both upper and lower thresholds on the D_S for which K spikes are stable. Note that multiple solutions (e.g. two or three spikes) can be stable at the same time. This is illustrated in Figure 2.8.

2.4 The regime $D_R \leq O(\varepsilon^2)$

2.4.1 Spike motion

We now study the motion of the interior spike, which is determined by small eigenvalues. We rewrite the system as following:

$$\begin{cases} S_t = D_S S_{xx} - SI^2 + \gamma R, \\ I_t = \varepsilon^2 I_{xx} + SI^2 - I, \\ R_t = D_R R_{xx} + I - \gamma R \end{cases} \tag{2.49}$$

with Neumann boundary conditions and $D_S, D_R \gg O(\varepsilon^2)$. To study the motion of the spike, we expand around the center x_0 by writing $x = x_0 + \varepsilon y$, and let $x_0 = x_0(\varepsilon^2 t)$, $S(y,t) = S\left(\frac{x-x_0(\varepsilon^2 t)}{\varepsilon}\right)$, $I(y,t) = I\left(\frac{x-x_0(\varepsilon^2 t)}{\varepsilon}\right)$, and $R(y,t) = R\left(\frac{x-x_0(\varepsilon^2 t)}{\varepsilon}\right)$. Then system (2.49) becomes

$$\begin{cases} -\varepsilon^3 x_0' S_y = D_S S_{yy} - \varepsilon^2 S I^2 + \varepsilon^2 \gamma R, \\ -\varepsilon x_0' I_y = I_{yy} + S I^2 - I, \\ -\varepsilon^3 x_0' R_y = D_R R_{yy} + \varepsilon^2 I - \varepsilon^2 \gamma R. \end{cases} \tag{2.50}$$

Applying the same expansion (2.5) and collecting ε order terms, we obtain that

$$\begin{cases} S_{1yy} = 0, \\ -x_0' I_{0y} = I_{1yy} + \chi S_1 I_0^2 + 2\chi S_0 I_0 I_1 - I_1, \\ R_{1yy} = 0, \end{cases} \tag{2.51}$$

in which S_0, I_0, R_0 are expressed in (2.19), (2.7) and (2.13). We then multipy the second equation by I_{0y} and integrate to obtain the solvability condition

$$x_0' \int_{-\infty}^{\infty} I_{0y}^2 dy = \frac{1}{3} \int_{-\infty}^{\infty} I_0^3 S_{1y} dy. \tag{2.52}$$

From (2.51), we know that S_1 is linear so that S_{1y} is a constant. To determine S_{1y}, we match to the outer region. We expand

$$\begin{aligned} S(x; x_0) &= S(x_0 + \varepsilon y; x_0) \\ &= S(x_0) + \varepsilon y S'(x_0), \end{aligned} \tag{2.53}$$

where $S(x; x_0)$ in outer region is expressed in (2.14). We then match it with the expansion (2.5) to get

$$S_1 = \left(-\frac{6\varepsilon}{S_0 D_S} G'(x_0; x_0) \right) y, \tag{2.54}$$

where $G(x; x_0)$ is expressed in (2.12). Therefore we have

$$S_{1y} = -\frac{6\varepsilon}{S_0 D_S} \begin{cases} G(x_0^+; x_0), & -L < x < x_0 \\ G(x_0^-; x_0), & x_0 < x < L. \end{cases} \tag{2.55}$$

Substituting (2.55) into the equation (2.52) gives the equation that describes the motion of the interior spike:

$$x_0' = -\frac{6\varepsilon}{D_S S_0^2} \frac{\sinh\left(2\sqrt{\frac{\gamma}{D_R}} x_0\right)}{\sinh\left(2\sqrt{\frac{\gamma}{D_R}} L\right)}, \tag{2.56}$$

where S_0 is expressed in (2.19). Writing

$$S_0 = \varepsilon \hat{S}, \tag{2.57}$$

we then have

$$\frac{dx_0}{dt} = -\frac{6\varepsilon}{D_S \hat{S}^2} \frac{\sinh\left(2\sqrt{\frac{\gamma}{D_R}}x_0\right)}{\sinh\left(2\sqrt{\frac{\gamma}{D_R}}L\right)}. \tag{2.58}$$

It's obvious to see that equation (2.58) has one equilibrium $x_0 = 0$, and the corresponding eigenvalue is

$$\lambda = -\frac{12\varepsilon}{D_S \hat{S}^2} \frac{\sqrt{\frac{\gamma}{D_R}}}{\sinh\left(2\sqrt{\frac{\gamma}{D_R}}L\right)} < 0. \tag{2.59}$$

Therefore the equilibrium centered at $x_0 = 0$ is stable with respect to spike motion.

2.4.2 Boundary effects and spike motion

From formula (2.59), it is clear that the eigenvalue is *stable*, provided that D_R is not too small. However, usng FlexPDE, numerical experiments to system (2.49) show that the spike becomes unstable and moves to the boundary when D_R is of $O(\varepsilon^2)$. To understand this, note that for small D_R, (2.19) simplifies to

$$S_0 \sim \frac{6\varepsilon(1+\frac{1}{\gamma})}{N} \tag{2.60}$$

and $\hat{S} \sim \frac{6(1+\frac{1}{\gamma})}{N}$. Therefore (2.59) simplifies to

$$\lambda \sim -\frac{2}{3} \frac{\varepsilon N^2}{D_S(1+\frac{1}{\gamma})^2} \sqrt{\frac{\gamma}{D_R}} \exp\left(-2L\sqrt{\frac{\gamma}{D_R}}\right), \quad D_R \ll 1. \tag{2.61}$$

As such, the effect of $\langle S_x \rangle$ becomes exponentially small. On the other hand, there are also exponentially weak boundary effects due to the interaction of the pulse with the boundary that we disregarded in the computation leading to (2.52). These boundary terms appear when integrating by parts in (2.52). To compute them, we replace (2.52) by a more precise expression

$$-x_0' \int I_{0y}^2 dy = (I_{0y} I_{1y} - I_0 I_1)\Big|_{y=\frac{-L-x_0}{\varepsilon}}^{y=\frac{L-x_0}{\varepsilon}} + \int I_{0y} I_0^2 S_1 dy. \tag{2.62}$$

The computation of the boundary terms is relatively standard and we summarize it here. Note that

$$w(y) \sim 6e^{-y} \text{ as } y \to \infty \tag{2.63}$$

so that

$$I_0 \sim \frac{6}{S_0} \exp(-y). \tag{2.64}$$

For x near L, we change variables:

$$x = L + \varepsilon z$$

so that $y = \frac{L-x_0}{\varepsilon} + z$ and

$$I_0 \sim \frac{6}{S_0} \exp\left(-\frac{L-x_0}{\varepsilon}\right) \exp(z). \tag{2.65}$$

Near $z = 0$, the equation for I_1 satisfies $I_{1zz} - I_1 \sim 0$, so that $I_1 = A \exp z + B \exp(-z)$. Since $I'(L) = 0$, we must therefore have

$$I_1 \sim \frac{6\varepsilon}{S_0} \exp\left(-\frac{L-x_0}{\varepsilon}\right) \exp(-z), \tag{2.66}$$

so that

$$(I_{0x}I_{1x} - I_0 I_1)|_{x=L} = -\frac{72\varepsilon}{S_0^2} \exp\left(-2\frac{L-x_0}{\varepsilon}\right). \tag{2.67}$$

Performing a similar computation at $x = -L$, and evaluating the remaining terms as before, we obtain

$$x_0' \sim -\frac{6\varepsilon}{D_S} \frac{\sinh\left(2\sqrt{\frac{\gamma}{D_R}}x_0\right)}{\sinh\left(2\sqrt{\frac{\gamma}{D_R}}L\right)} \frac{1}{\hat{S}^2} + 60\varepsilon \left\{ \exp\left(2\frac{x_0 - L}{\varepsilon}\right) - \exp\left(2\frac{-L - x_0}{\varepsilon}\right) \right\} \tag{2.68}$$

so that

$$\lambda \sim -\frac{12\varepsilon}{D_S} \frac{\sqrt{\frac{\gamma}{D_R}}}{\sinh\left(2\sqrt{\frac{\gamma}{D_R}}L\right)} \frac{1}{\hat{S}^2} + 240 \exp\left(-\frac{2L}{\varepsilon}\right). \tag{2.69}$$

This expression clearly shows that the boundary term can play a destabilizing effect when the first term on the right hand side of (2.69) is exponentially small. This happens precisely when D_R is small. Setting $\lambda = 0$, substituting $\hat{S} \sim \frac{6(1+\frac{1}{\gamma})}{N}$ and solving for D_s yields the critical value

$$D_S^* \sim \frac{\varepsilon N^2}{1440} \sqrt{\frac{\gamma}{D_R}} \exp\left(2L\left(\frac{1}{\varepsilon} - \sqrt{\frac{\gamma}{D_R}}\right)\right) \tag{2.70}$$

with a single spike centered at center being unstable when $D_S > D_S^*$, and stable otherwise. This phenomenon is illustrated in Figure 2.2. Take $L = 2, \gamma = 1, N = 5$ and $D_R = 0.005298$. Then (2.70) yields $D_S^* = 5.00$. It follows that a single spike is unstable at the origin when $D_R < 0.005298$ and is stable otherwise. This is confirmed in Figure 2.2.

The boundary effect discussed here is similar to the destabilization discussed in [107]. However the difference here is that this effect is primarily driven by having a small D_R, and is very specific to having three components. Although the asymptotics of (2.70) are valid as long as $D_R \gg O(\varepsilon^2)$, a similar destabilization phenomenon also happens when $D_R = O(\varepsilon^2)$. Although the asymptotics of (2.70) break down in such a case, numerics show that the destabilization phenomenon persists as D_S is increased.

2.4.3 Mesa-like steady states when $D_R = 0$.

As shown in last section, multi-spike configurations lose stability when D_R is sufficiently small: even a single spike eventually becomes unstable (due to an exponentially small eigenvalue becoming positive) and moves towards the boundary when $D_R = O(\varepsilon^2)$. For even smaller values of D_R, we observe numerically that the spike "fattens" as shown in Figure 2.9. In the limit of $D_R \to 0$, numerics indicate a phase separation of infected population. This can be thought of as a "quarantine effect": when mobility of recovered population and susceptible population is reduced, the infected population is confined to a certain region of the entire domain with a sharp interface inbetween.

Here we perform the analysis for the limiting case $D_R = 0$ and D_S being small, although similar results hold even when $D_R = D_S$ and is nonzero. At the steady steate, we then have $I = \gamma R$ so that the model (2.2) reduces to

$$\begin{cases} 0 = D_S S_{xx} - SI^2 + I, \\ 0 = \varepsilon^2 I_{xx} + SI^2 - I. \end{cases} \tag{2.71}$$

Adding the two equations we obtain that $D_S S + \varepsilon^2 I$ is constant. We then eliminate S from the second equation to obtain

$$D_S I_{xx} = \frac{D_S}{\varepsilon^2} I - CI^2 + I^3, \tag{2.72}$$

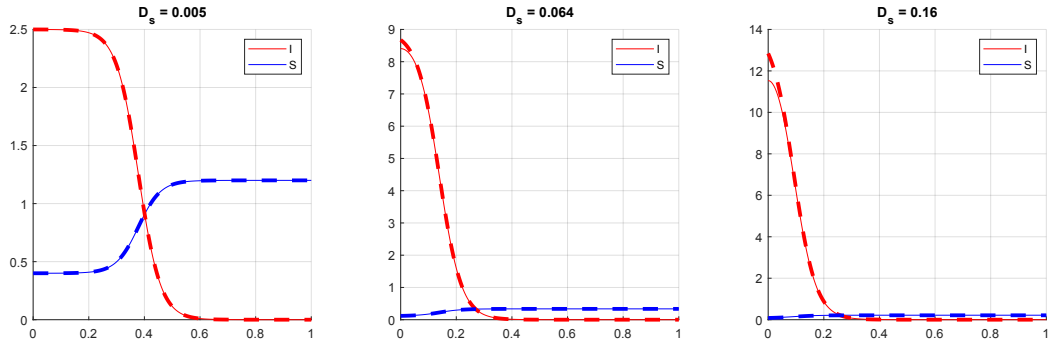

Figure 2.9: Steady states of the system (2.2) with $L = 1, D_R = 0$, $\varepsilon = 0.04$, $\gamma = 1$, $N_0 = 2.79$ and with D_S as indicated. Solid curves correspond to the full numerical solutions of (2.2). These numerical solutions correspond to steady states obtained by running (2.2) in FlexPDE for a long time ($t = 10^5$). Dashed lines show the asymptotic approximation (2.75).

where

$$C = I + \frac{D_S}{\varepsilon^2} S \tag{2.73}$$

is a constant to be determined.

Equation (2.72) admits a heteroclinic solution connecting the steady state $I = 0$ to a positive steady state I_+ provided that the Maxwell-line condition holds:

$$\int_{I0}^{I_+} \left(\frac{D_S}{\varepsilon^2} I - CI^2 + I^3 \right) dI = 0.$$

This is equivalent to the cubic having equidistant roots, that is,

$$\frac{D_S}{\varepsilon^2} I - CI^2 + I^3 = I \left(I - \frac{I_+}{2} \right) (I - I_+) \tag{2.74}$$

so that

$$I_+ = \sqrt{\frac{2D_S}{\varepsilon^2}}, \quad C = \frac{3}{2} I_+. \tag{2.75}$$

In this case there is an interface solution on the domain $[0, L]$ given by

$$\gamma R = I \sim I_+ \left(\frac{1}{2} \tanh \left(\frac{I_+}{2\sqrt{2}} \frac{(l - |x|)}{\sqrt{D_S}} \right) + \frac{1}{2} \right); \tag{2.76}$$

$$S \sim \frac{\varepsilon^2}{D_S} I_+ \left(1 - \frac{1}{2} \tanh \left(\frac{I_+}{2\sqrt{2}} \frac{(l - |x|)}{\sqrt{D_S}} \right) \right). \tag{2.77}$$

Here, l is the location of the interface. A back-to-back interface solution such as shown in Figure 2.3 is obtained by extending this solution to $[-L, L]$ using even reflection.

Finally, the interface location l is determined using the mass conservation condition, $N_0 L = \int_0^L (S + I + R)dx$. In the limit $\varepsilon \to 0$, this yields

$$LN_0 = I_+ \left\{ \left(1 + \frac{1}{\gamma}\right) l + \left(\frac{3}{2}L - \frac{1}{2}l\right) \left(\frac{\varepsilon^2}{D}\right) \right\},$$

and solving for l we obtain

$$l = \frac{N_0 - I_+ \frac{3}{2} \left(\frac{\varepsilon^2}{D}\right)}{I_+ \left(1 + \frac{1}{\gamma} - \left(\frac{\varepsilon^2}{D}\right)\right)} L. \tag{2.78}$$

This result is valid as long as $O(\varepsilon) \ll l < L$. In this case, the interface has an exponentially weak effect on the boundary, and the agreement with the numerical solutions of the system (2.2) is nearly perfect. This is illustrated in Figure 2.9. Solution (2.75) is shown super-imposed on the numerical solution; the difference is imperceptible in the "eye-ball norm"as long as $l = O(1)$. The asymptotics break down when l becomes small (Figure 2.9, right), and the interface transforms into a spike solution.

Note that the infected class subdivides the domain into an outbreak portion ($x < l$) and a disease-free portion ($x > l$). The susceptible population is three times smaller within the outbreak portion of the domain when compared with the disease-free portion.

For simplicity, we took $D_R = 0$ here. Numerical simulations using FlexPDE indicate that similar interface solutions persist for sufficiently small D_R, although it changes l as well as the interface shape. We defer their study to future work.

2.5 Discussion

In this chapter we studied the consequence of adding spatial diffusion to the relatively-standard SIRS model. Under certain reasonable assumptions, the resulting system (2.2) has a very rich solution space, exhibiting hot-spots as well as interface-type solutions, depending on whether D_R is large or small, respectively.

The hot-spot regime $D_R \gg O(\varepsilon^2)$ is very similar to previous analysis for two-component reaction-diffusion systems, such as the Schnakenberg model [27, 100], and the behaviour is qualitatively similar to the SI model with diffusion introduced in [58] (which itself is a generalization of the Schnakenberg model). However, from the

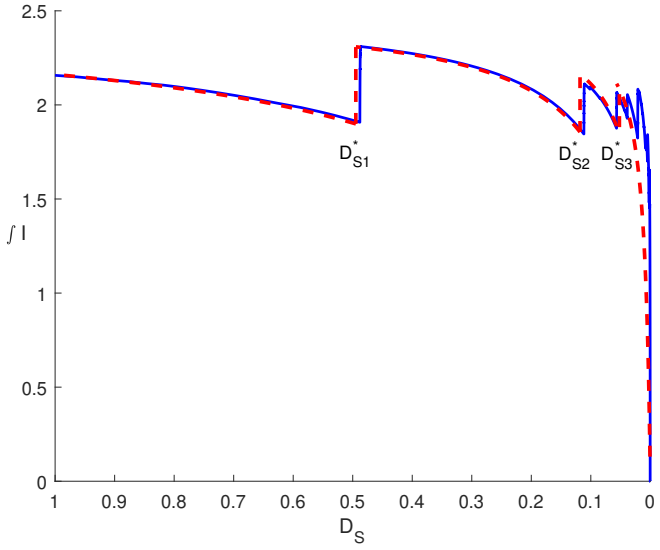

Figure 2.10: Total mass of infected people versus D_S. Here $\varepsilon = 0.005, N = 5, D_R = 1, L = 1$, $D_S = 1 - 10^{-5}t$, and $\gamma = 1$. The solid curve denotes numerical results obtained by FlexPDE, where the integral of I is computed as D_S is gradually decreased from 1 to 0. The dashed curve is the asymptotic result corresponding to the self-replication thresholds of Result 2.3.2.

analysis point of view, the third component introduces a novel non-local eigenvalue problem (see Section 2.2). On the other hand, the regime $D_R \leq O(\varepsilon^2)$ requires completely new analysis. On one hand, the resolution of an exponentially small boundary layer in Section 2.4.2 is crucial for computing stability thresholds of a single interior spike in this regime. On the other hand, this regime also leads to mesa-type solutions of Section 2.4.3. The analysis is similar to the interface solutions derived in [108, 109] for the Gray-Scott model. However it appears to be more robust: such interface solutions exist for a wide range of parameters here, rather than a very narrow range as studied in [108, 109].

In Figure 2.10 we plot the total mass of infected population versus D_S. As D_S is decreased, the mobility of susceptible population is reduced and this initially leads to a decrease of overall disease load. However as D_S is decreased further, eventually a self-replication threshold is triggered. This results in an immediate increase of infection hot-spots and an overall increase in the infected population. This underscores a highly nonlinear relationship between mobility and disease outbreaks.

Chapter 3

Spike dynamics of GM model in the presence of noise

The goal of this chapter is to study the effect of noise on spike dynamics in reaction-diffusion systems. We concentrate on dynamics of a single spike for the Gierer-Meinhardt (GM) model, which is among the simplest reaction-diffusion systems that manifests complex patterns. In one dimension, it has the following form in the absence of noise:

$$\begin{aligned} u_t &= \varepsilon^2 u_{xx} - u + \tfrac{u^2}{v}\,, \\ 0 &= v_{xx} - v + \tfrac{u^2}{\varepsilon}\,. \end{aligned} \tag{3.1}$$

This system can be obtained from general form (1.8) by first taking $p = 2, q = 1, r = 2, s = 0$, then rescaling $u = \frac{\hat{u}}{\varepsilon}$ and $v = \frac{\hat{v}}{\varepsilon}$. Moreover, we choose $\tau = 0$ in (1.8) so that it doesn't affect spike dynamics. We assume $\varepsilon \ll 1$ and Neumann boundary conditions on an interval $x \in [-L, L] : u_x = v_x = 0$ at $x = \pm L$.

There are many ways to introduce noise. Here we study the effect of introducing the noise in th equation for the activator. As we will show, this has a direct effect on the motion of spikes. For concreteness, let us assume that only the decay rate of the activator u is stochastic, although similar analysis works for other types of noise, some of which we discuss in section 3.4. By introducing the noise in the decay of u; equation (3.1) then becomes

$$\begin{aligned} u_t &= \varepsilon^2 u_{xx} - u + \tfrac{u^2}{v} + \sigma u W \tfrac{\sqrt{dt}}{dt}\,, \\ 0 &= v_{xx} - v + \tfrac{u^2}{\varepsilon}\,, u_x = v_x = 0 \quad \text{at} \quad x = \pm L. \end{aligned} \tag{3.2}$$

Here $W(x,t)$ is the spatio-temporal Gaussian white noise. We define W to be

$$W(x,t) = \psi_0(t) + \sqrt{2} \sum_{m=1}^{(N-1)/2} \left(\psi_m(t) \cos\left(\frac{m\pi}{L}\, x\right) + \phi_m(t) \sin\left(\frac{m\pi}{L}\, x\right)\right), \tag{3.3}$$

where ψ_m, ϕ_m are independent standard normal distributions of mean zero and variance one. This definition is motivated in part as follows. When discretizing (3.3) using finite differences on a uniform mesh x_k of size N, one obtains that $W(x_k; t)$

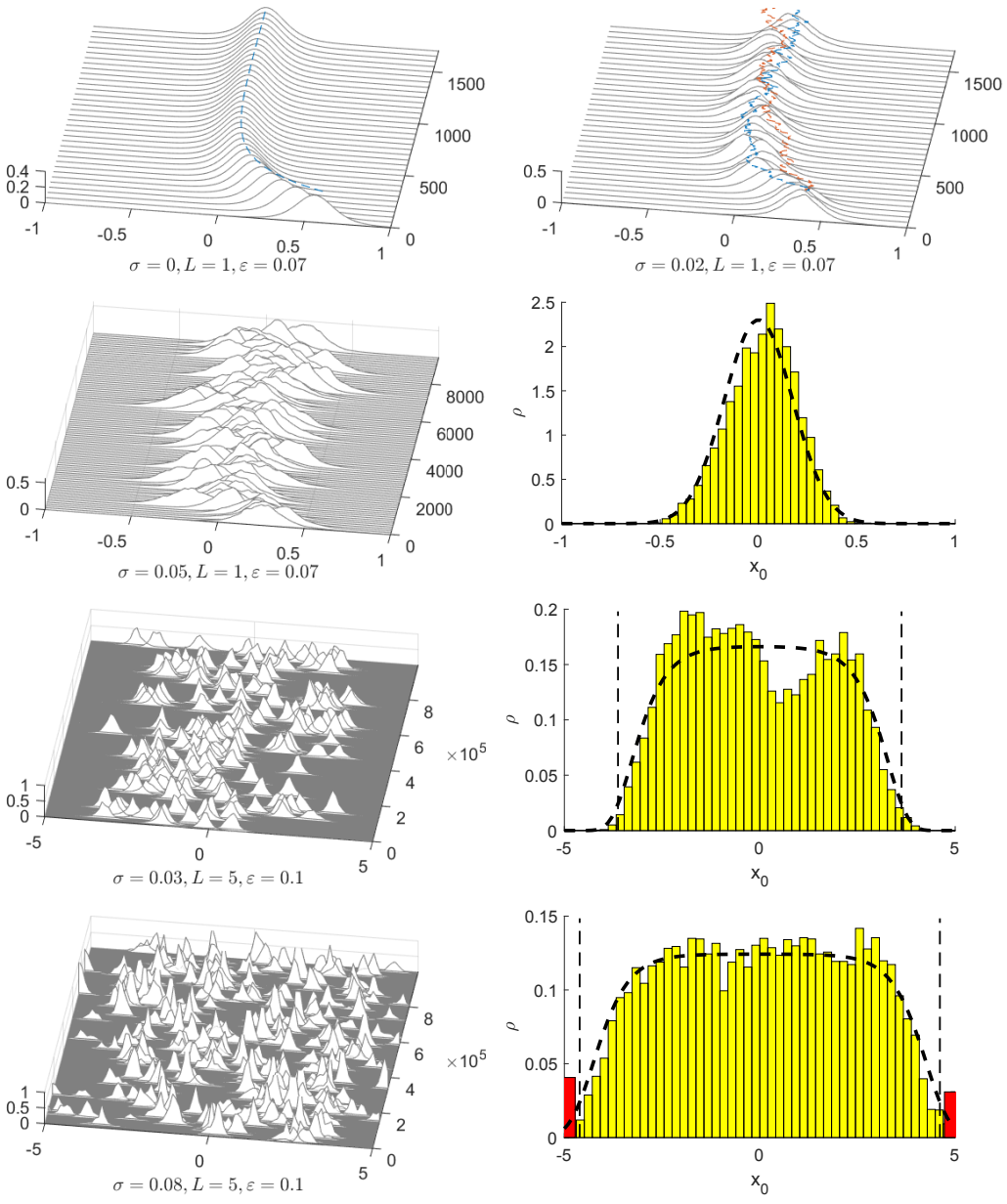

Figure 3.1: Top row and left column: simulation of the full PDE (3.2), parameters as indicated. Dashed lines correspond to the simulation of the SODE (3.4) for the reduced dynamics of the center of the spike. Right column, last three rows: histogram shows probability distribution of spike position over time, as extracted from the corresponding figure to its left. Dashed line denotes the analytical prediction (3.6). For larger σ (bottom right), the spike can hit the boundary and get "stuck" there for some time as indicated by red bars, and then drift back to the middle.

are independent normal variables, all with variance N: See Appendix B for detailed explanations as well as the matlab code for simulating (3.2).

Let us summarize our main findings, which are illustrated in Figure 3.1. As is well known [3, 96], in the absence of noise, the spike center x_0 drifts towards a center of the domain $x = 0$ on a slow-time ($O(\varepsilon^2)$) scale. The reduced equation for the motion of a single spike consists of an ODE for the spike position. When the noise is turned on in the activator equation, it manifests as noise at the level of the reduced equation for the spike motion. As a result, the reduced equation becomes a *stochastic* ODE. In section 3.1 we derive the following SODE which describes the motion for the spike center x_0 :

$$dx_0 \sim -\frac{2\sinh(2x_0)}{\cosh(2x_0)+\cosh(2L)}ds + \sigma^*\xi\sqrt{ds}; \qquad s = \varepsilon^2 t, \tag{3.4}$$

Here, $\xi(s) = \mathcal{N}(0,1)$ is normal random variable and σ^* is the standard deviation, independent of space, given by

$$\sigma^* = \sigma\left(\frac{L}{\varepsilon}\right)^{1/2}\sqrt{\frac{10}{7}}. \tag{3.5}$$

The ODE (3.4) is only valid as long as x_0 remains *away* from the boundaries $\pm L$, more specifically, as long as $|x_0 \pm L| \gg O(\varepsilon)$. In the absence of noise ($\sigma^* = 0$), the deterministic part pushes the spike towards its equilibrium at the center, while the noise can push it *away* from the center. If σ^* is relatively small, the deterministic part dominates, and the spike remains near the center of the domain. In this case, using the Fokker-Plank equation, and for sufficiently small σ^*, we show in section 3.2 that the stationary distribution of spike positions has a density given explicitly by

$$\rho(x_0) = C\exp\left\{-\frac{2}{(\sigma^*)^2}\log\left(\frac{\cosh(2x_0)+\cosh(2L)}{1+\cosh(2L)}\right)\right\}, \tag{3.6}$$

where C is a constant chosen so that $\int \rho(x_0)dx_0 = 1$.

Figure 3.1 shows an excellent agreement of the direct simulations of (3.2) and the spike distribution density given by (3.6), (3.5), as long as σ is not too big. Since the spike motion is restricted to the domain $[-L, L]$, formula (3.6) is restricted to those parameter values for which ρ is vanishingly small outside $x \in [-L, L]$ [1].

[1]Here, "vanishing" is used loosely to mean exponentially small; meaning in practical terms that it is not expected to be observed numerically within a reasonable timeframe (say a week of running on a standard laptop). For example, for parameters in row 2 of Figure 3.1, one finds $\rho(\pm L)/\rho(0) \approx 1.3 \times 10^{-10}$. The precise measure is clarified in Section 3.3 in terms of Mean First Passage Time.

On the other hand, when σ becomes too big, the density (3.6) does not "fit" into the domain $[-L, L]$ and there is a non-vanishing chance that a spike "hits" the boundary. While the SODE cannot predict what happens when the spike collides with the boundary, it can predict how long it takes (on average) before such collision occurs. Numerically, we observe that following the collision, the spike can remain at the boundary for some time, until the noise eventually kicks it off the boundary. This is illustrated in the bottom row of figure 3.1; red bars correspond to the spike being temporarily "stuck" near the boundary. The expected time for the spike to "hit" the boundary can be formulated in terms of the Mean First Passage Time (MFPT) problem. This is done in section 3.3.

We now summarize this chapter. We derive the SODE (3.4) in section 3.1. The spike position distribution is analyzed in section 3.2; in the case of large L, we also derive the "trapping region" of size $2l$ such that the spike remains "trapped" within a region $|x| < l \leq L$. The hitting time to the boundary is studied in section 3.3. We conclude in section 3.4 where we discuss some generalizations and propose several open problems.

3.1 Derivation of Reduced SODE for Spike Motion

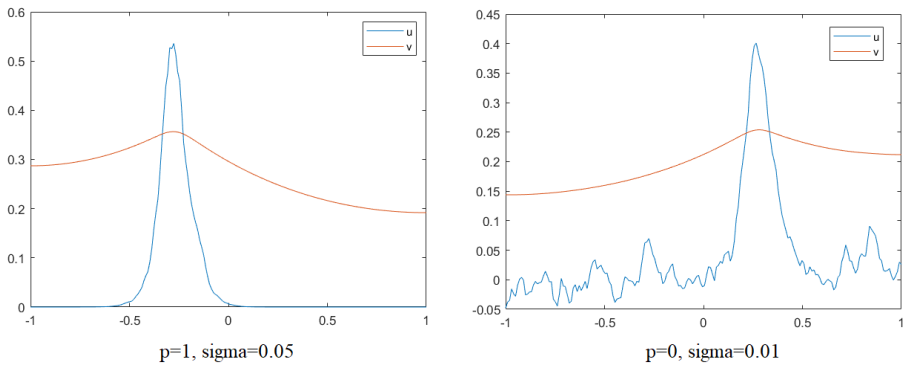

Figure 3.2: Spike in the presence of noise. Here, $\varepsilon = 0.05$. Left: when $p = 1$, the noise affects the inside of the spike only. Right: when $p = 0$, the whole spike including the background is affected.

We now derive the equations of motion starting with the PDE system (3.2). In

fact, we will generalize this slightly, by replacing

$$uW \to u^p W \tag{3.7}$$

in (3.2) and considering both the cases $p = 1$ as well as $p = 0$. A typical snapshot of solutions for the two cases is shown in Figure 3.2. The case $p = 0$ is discussed in section 3.4. When $p = 1$; the noise is mostly occuring inside a spike, but does not affect the background due to exponential decay of u. On the other hand, when $p = 0$, the noise affects the background and can lead to many other phenomena as discussed in section 3.4.

We use by-now-standard techniques to reduce the full PDE solution to an ODE system for spike center position x_0. The derivation is rather standard, see for example [110, 3, 96, 111, 100, 112, 4]. In particular the deterministic part in (3.4) is well known, although we rederive it here in full for convenience. The main novelty here is to derive the reduced noise level σ^* (3.5) from the original system.

Let $x_0(t)$ denote the position of the spike. In the inner region near x_0 we expand (3.2) as follows:

$$\begin{aligned} x &= x_0(s) + \varepsilon y, \quad s = \varepsilon^2 t \\ u(x,t) &= U_0(y) + \varepsilon U_1(y) + \dots, \\ v(x,t) &= V_0(y) + \varepsilon V_1(y) + \dots. \end{aligned}$$

To leading order in ε we have

$$0 = U_{0yy} - U_0 + \frac{U_0^2}{V_0}, \quad 0 = V_{0yy} \tag{3.8}$$

and at the next order, after collecting $O(\varepsilon)$ terms, we obtain

$$-x_0'(s)U_{0y} = U_{1yy} - U_1 + 2\frac{U_0 U_1}{V_0} - \frac{U_0^2}{V_0^2}V_1 + \sigma U_0^p W \frac{\sqrt{ds}}{ds}, \tag{3.9}$$

$$0 = V_{1yy} + U_0^2. \tag{3.10}$$

Then V_0 is a constant and therefore U_0 can be written as

$$U_0(y) = w(y)V_0 \tag{3.11}$$

where w is the well-known ground state satisfying

$$w_{yy} - w + w^2 = 0, \quad w \to 0 \text{ as } |y| \to \infty, \quad w'(0) = 0 \tag{3.12}$$

with the explicit solution given by

$$w(y) = \frac{3}{2}\operatorname{sech}^2(y/2). \tag{3.13}$$

In the outer region, we write

$$v \sim SG(x, x_0) \tag{3.14}$$

where G is the Green's function satisfying

$$G_{xx} - G + \delta(x - x_0) = 0, \qquad G_x(\pm L) = 0 \tag{3.15}$$

given by

$$G(x; x_0) = \frac{1}{\sinh(2L)} \begin{cases} \cosh(x + L)\cosh(x_0 - L), & -L < x < x_0 \\ \cosh(x_0 + L)\cosh(x - L), & x_0 < x < L \end{cases}, \tag{3.16}$$

and S is computed as

$$S = \int_{x_0^-}^{x_0^+} \frac{u^2(x)}{\varepsilon} dx \sim \int_{-\infty}^{\infty} (w(y)V_0)^2 \, dy = 6V_0^2.$$

Matching inner and outer regions we obtain $V_0 \sim v(x_0) \sim SG(x_0, x_0)$ so that

$$V_0 = \frac{1}{6G_0}; \quad G_0 = G(x_0, x_0) = \frac{\cosh(2x_0) + \cosh(2L)}{2\sinh(2L)}.$$

Finally we formulate the solvability condition to determine x_0. Multiplying (3.9) by U_{0y} we have:

$$\begin{aligned} -x_0'(s) \int_{-\infty}^{\infty} U_{0y}^2 dy = &\int_{-\infty}^{\infty} U_{0y} \left(U_{1yy} - U_1 + 2\frac{U_0 U_1}{V_0} \right) dy - \int_{-\infty}^{\infty} U_{0y} \frac{U_0^2}{V_0^2} V_1 dy \\ &+ \sigma \frac{\sqrt{ds}}{ds} \int_{-\infty}^{\infty} U_{0y} U_0^p W dy. \end{aligned} \tag{3.17}$$

We now integrate by parts using the decay of w at infinity to obtain

$$\int_{-\infty}^{\infty} U_{0y} \left(U_{1yy} - U_1 + 2\frac{U_0 U_1}{V_0} \right) dy = \int_{-\infty}^{\infty} U_1 \left(U_{0yyy} - U_{0y} + 2\frac{U_{0y} U_{0y}}{V_0} \right) dy.$$

Note that

$$U_{0yyy} - U_{0y} + 2\frac{U_{0y} U_{0y}}{V_0} = \left(w_{yyy} - w_y + 2ww_y \right) V_0 = 0,$$

since $w_{yyy} - w_y + 2ww_y = \left(w_{yy} - w + w^2 \right)_y = 0$ (see (3.12)). So (3.17) simplifies to

$$-x_0'(s) \int_{-\infty}^{\infty} U_{0y}^2 dy = -\int_{-\infty}^{\infty} U_{0y} \frac{U_0^2}{V_0^2} V_1 dy + \sigma \frac{\sqrt{ds}}{ds} \int_{-\infty}^{\infty} U_{0y} U_0^p W dy. \tag{3.18}$$

We further evaluate

$$-\int_{-\infty}^{\infty} U_{0y}\frac{U_0^2}{V_0^2}V_1 dy = \frac{V_0}{3}\int_{-\infty}^{\infty} w^3 V_{1y} dy. \tag{3.19}$$

From (3.10), we have

$$V_{1y}(y) = -\int_0^y U_0^2(s)ds + \frac{V_{1y}(\infty)+V_{1y}(-\infty)}{2}.$$

Since $\int_0^y U_0^2(s)ds$ is an odd function and using $\int_{-\infty}^{\infty} w^3 dy = \frac{36}{5}$, the integral in (3.19) evaluates to

$$\int_{-\infty}^{\infty} w^3 V_{1y} dy = \frac{V_{1y}(\infty)+V_{1y}(-\infty)}{2}\frac{36}{5}.$$

We match inner and outer solutions to obtain

$$V_{1y}(\pm\infty) = SG_x\left(x_0^{\pm}, x_0\right) = 6V_0^2 G_x\left(x_0^{\pm}, x_0\right).$$

Using $\int_{-\infty}^{\infty} w_y^2 dy = 6/5$ we get

$$x_0'(s) = -\frac{G_x\left(x_0^+, x_0\right) + G_x\left(x_0^-, x_0\right)}{G(x_0,x_0)} - \sigma\frac{\sqrt{ds}}{ds}V_0^{P-1}\frac{\int w_y w^p W dy}{6/5}. \tag{3.20}$$

From (3.16) we compute

$$\frac{G_x\left(x_0^+, x_0\right) + G_x\left(x_0^-, x_0\right)}{G(x_0,x_0)} = \frac{2\sinh(2x_0)}{\cosh(2x_0)+\cosh(2L)}. \tag{3.21}$$

It remains to evaluate the integral in (3.20). Using the addition formulas $\cos(x) = \cos(x_0+\varepsilon y) = \cos(x_0)\cos(\varepsilon y) - \sin(x_0)\sin(\varepsilon y)$ and parity, we compute

$$\int_{-\infty}^{\infty} w_y w^p \cos\left(x\frac{m\pi}{L}\right) dy = -\sin\left(x_0\frac{m\pi}{L}\right)\int_{-\infty}^{\infty}\sin\left(\varepsilon y\frac{m\pi}{L}\right) w_y w^p dy$$
$$\int_{-\infty}^{\infty} w_y w^p \sin\left(x\frac{m\pi}{L}\right) dy = \cos\left(x_0\frac{m\pi}{L}\right)\int_{-\infty}^{\infty}\sin\left(\varepsilon y\frac{m\pi}{L}\right) w_y w^p dy.$$

Define

$$F_p(x) := \int_{-\infty}^{\infty}\sin(xy)\, w_y w^p dy,$$

whose value is derived explicitly in Appendix C. In terms of F_p we have

$$\int W w_y w^p dy = \sqrt{2}\sum_{m=1}^{(N-1)/2} F_p\left(\frac{m\pi}{L}\varepsilon\right)\left(-\psi_m(t)\sin\left(x_0\frac{m\pi}{L}\right) + \phi_m(t)\cos\left(x_0\frac{m\pi}{L}\right)\right). \tag{3.22}$$

Finally, we compute the variance of $\sigma V_0^{P-1} \frac{\int w_y w^p W dy}{6/5}$. This is done by approximating the summation by an integral as follows,

$$\begin{aligned}(\sigma^*)^2 &= \left(\frac{\sigma V_0^{P-1}}{6/5}\right)^2 2 \sum_{m=1}^{(N-1)/2} F_p^2\left(\frac{m\pi}{L}\varepsilon\right) \\ &\sim \left(\frac{\sigma V_0^{P-1}}{6/5}\right)^2 2 \int_0^{N/2} F_p^2\left(\frac{m\pi}{L}\varepsilon\right) dm \\ &\sim \left(\sigma G_0^{1-p} 5 \cdot 6^{-p}\right)^2 2 \frac{L}{\pi\varepsilon} \int_0^{\infty} F_p^2(z)\, dz.\end{aligned}$$

The latter integral is computed in Appendix C with the result

$$\int_{-\infty}^{\infty} F_p^2(x) dx = \begin{cases} \frac{6}{5}\pi, & p=0 \\ \frac{36}{35}\pi, & p=1 \end{cases}.$$

To summarize, we obtain

$$\sigma^* = \sigma \sqrt{\frac{L}{\varepsilon}} G_0^{1-p} C_p \tag{3.23}$$

where

$$C_p = \sqrt{\left(5 \cdot 6^{-p}\right)^2 \frac{2}{\pi} \int_0^{\infty} F_p^2(z)\, dz} = \begin{cases} \sqrt{60}, & p=0 \\ \sqrt{\frac{10}{7}}, & p=1 \end{cases}.$$

In particular,

$$p=0: \quad \sigma^* = \sigma \sqrt{\frac{15L}{\varepsilon}} \frac{\cosh(2x_0)+\cosh(2L)}{\sinh(2L)}, \tag{3.24}$$

$$p=1: \quad \sigma^* = \sigma \sqrt{\frac{L}{\varepsilon}} \sqrt{\frac{10}{7}}. \tag{3.25}$$

This yields equation (3.4) when $p=1$. The case $p=0$ is discussed in section 3.4.

A similar derivation is possible if we impose periodic boundary conditions on (3.2) instead of Neumann boundary conditions. Then resulting ODE for spike motion is simply (3.4) but without the drift: $dx_0 \sim \sigma^* \xi \sqrt{ds}$, and with $x_0 \in [-L, L]$ taken $\bmod 2L$ (so that the spike that crosses through a left boundary re-emerges on the right boundary and vice-versa). This corresponds to a simple Brownian motion with periodic boundary conditions.

3.2 Spike position distribution

For a general SODE

$$dx = f(x)ds + \sigma(x)\xi\sqrt{ds}, \tag{3.26}$$

subject to initial condition $x(0) = a$, the probability density $\rho(x,t)$ for x to be at a given location at time t satisfies the Fokker-Plank PDE

$$\rho_t = \left(\frac{\sigma^2}{2}\rho\right)_{xx} - (f\rho)_x$$

subject to initial conditions $\rho(x,0) = \delta(x-a)$. See for example [113, 114] for the derivation, or the appendix of [115] for an alternative derivation using integral master equation. The long-time equilibrium density distribution $\rho(x,t) = \rho(x)$ then satisfies $\left(\frac{\sigma^2}{2}\rho\right)_x + f\rho = K$. Assuming the density is finite and decays at $x = \pm\infty$, we must have $K = 0$ so that the equilibirum density is explicitly given by

$$\rho = \frac{2}{\sigma^2} C \exp\left(\int \frac{2}{\sigma^2} f\right) \tag{3.27}$$

where C is a constant of integration chosen so that $\int \rho = 1$. Here, we specialize to the SODE (3.4). For convenience we relabel $x_0 = x$. We evaluate $\int_0^x f = -\log\left(\frac{\cosh(2x)+\cosh(2L)}{1+\cosh(2L)}\right)$ and $\sigma(x) = \sigma^*$ is a constant. This leads to equation (3.6) for the density. In the context of a bounded domain $x \in [-L, L]$, this formula implicitly assumes that ρ is vanishly small near $x = \pm L$. Figure 3.3 shows the graph of $\rho(x)$ for several values of L and σ^*. In the limit of small σ^*, the density is nearly Gaussian. By Taylor-expanding (3.6) for small x we obtain

$$\rho(x_0) \sim C \exp\left\{-\frac{1}{(\sigma^*)^2}\frac{4x^2}{1+\cosh(2L)}\right\} \tag{3.28}$$

where $C = \sqrt{\frac{1}{\pi}\frac{1}{(\sigma^*)^2}\frac{4}{1+\cosh(2L)}}$.

On the other hand, when $L \gg 1$, equation (3.6) simplifies to

$$\rho(x) = C \exp\left\{-\frac{2}{(\sigma^*)^2} e^{2(|x|-L)}\right\}. \tag{3.29}$$

As shown in Figure 3.3, this is well-approximated by a piecewise-constant density, $\rho \sim \frac{1}{2l}\chi_{[-l,l]}$, where χ is the characteristic function. The length l of the box can be computed by setting $\rho(l) = a\rho(0)$, where $0 < a < 1$ is an arbitrarily chosen constant. Solving for l then yields

$$l \sim L - \log\left(\frac{1}{\sigma^*}\sqrt{\frac{2}{\log a^{-1}}}\right).$$

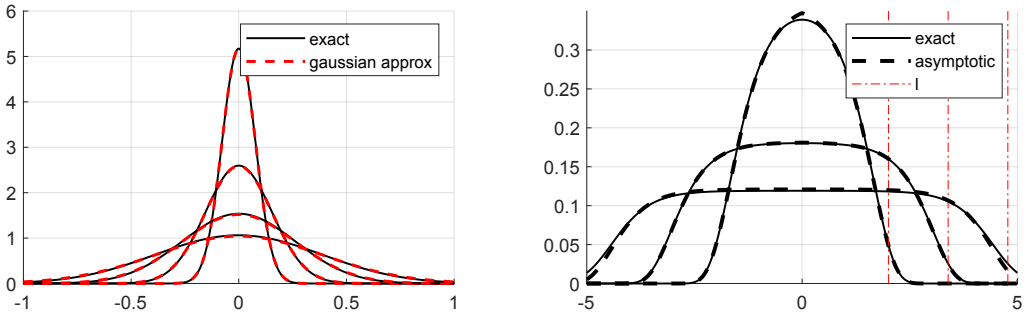

Figure 3.3: Spike density distribution $\rho(x)$ for several values of σ^* and L. Left: $L = 1$ and $\sigma^* = 0.1, 0.2, 0.3, 0.5$ (from highest to lowest). Solid line is the exact formula (3.6) whereas dashed line is the formula (3.28). Right: $L = 5$ and $\sigma^* = 0.1, 0.2, 0.3, 0.5$ (from highest to lowest). Solid line is the exact formula (3.6) whereas dashed line is the formula (3.29).

The choice of a is somewhat subjective. For sufficeintly small σ^* (with $(\sigma^*)^2 \ll O(\log a^{-1})$), to leading order we get

$$l \sim L - \log \frac{1}{\sigma^*}. \tag{3.30}$$

This formula is shown in Figure 3.3 (right); it also corresponds to choosing $a = e^{-2}$.

When $1 \ll l \ll L$, $\rho(x)$ exhibits a sharp transition near $x \sim l$: for $|x| \ll l$, we find $\rho(x) \sim C$ so that $\rho\,(x)$ is nearly constant in this case. For $l \ll |x| \leq L$, $\rho(x)$ is exponentially small so that $\rho\,(x)$ is nearly zero in that region. On the other hand, when l is near L, the density is non-negligible near $x = L$ and the spike is no longer confined away from the boundaries $\pm L$. In this case it will hit the boundary within a realistic timeframe (i.e. observable numerically on a computer for runtimes less than, e.g., a week). In the next section, we use MFPT to quantify this transition more precisely.

3.3 Boundary hitting time

As seen from the SODE (3.4), the spike motion is driven by a competition between the deterministic term that pushes the spike towards the center of the domain, and the noise term which can push the spike away from the center. If the noise is sufficiently large, it can counteract the attraction towards the center, and the spike will eventually collide with the boundary, given enough time.

We can formulate this as the Mean First Passage Problem (MFPT), corresponding to a stochastic particle first hitting the boundary $x = \pm L$. Consider the general SODE,

$$dx = f(x)ds + \sigma^* \xi \sqrt{ds}, \tag{3.31}$$

and let $m(x)$ be the average time it takes for a particle x to hit the boundary $x = \pm L$. Then $m(x)$ satisfies the following MFPT problem [114]:

$$\frac{(\sigma^*)^2}{2} m_{xx} + f(x)m_x + 1 = 0, \qquad m(\pm L) = 0. \tag{3.32}$$

An alternative derivation from first principles is given in Appendix D. For our problem,

$$f(x) = -\frac{2\sinh(2x)}{\cosh(2x) + \cosh(2L)} \tag{3.33}$$

and the solution to (3.32) is given by

$$m_x = -\frac{2}{(\sigma^*)^2} v_h \int_0^x \frac{1}{v_h(s)} ds, \tag{3.34}$$

where v_h satisfies $\frac{(\sigma^*)^2}{2} v_h' + f(x)v_h = 0$; that is,

$$v_h(x) = \exp\left(-\frac{2}{(\sigma^*)^2} \int_0^x f(s)ds\right). \tag{3.35}$$

Integrating (3.34) and using the boundary condition $m(L) = 0$ yields a semi-explicit expression for mean-first-passage time,

$$m(x) = \frac{2}{(\sigma^*)^2} \int_x^L \left\{ v_h(x) \int_0^x \frac{1}{v_h(s)} ds \right\} dx. \tag{3.36}$$

Further analysis is possible for two important cases: either L is large, or σ is small (or both).

Case A: σ^* is small and $L = O(1)$. We use Laplace's method to asymptotically approximate $m(x)$. Note that $f(x)$ is a decreasing function so that $\int_0^x f$ has a maximum at $x = 0$. Therefore we estimate, using Laplace's method, for $x > 0$:

$$\int_0^x \frac{1}{v_h(s)} ds \sim \int_0^\infty \exp\left(\frac{2}{(\sigma^*)^2} \int_0^x f(s)ds\right) dx \sim \frac{\sigma^*}{2} \sqrt{\frac{\pi}{-f'(0)}}$$

so that

$$m(x) \sim \frac{1}{\sigma^*} \sqrt{\frac{\pi}{-f'(0)}} \int_x^L \exp\left(-\frac{2}{(\sigma^*)^2} \int_0^x f(s)ds\right) dx.$$

Note that $-\int_0^x f$ attains its maximum at $|x| = L$, so we estimate, for $x > 0$:

$$\int_x^L \exp\left(-\frac{2}{(\sigma^*)^2}F(x)\right)dx \sim \exp\left(-\frac{2}{(\sigma^*)^2}\int_0^L f(s)ds\right)\frac{(\sigma^*)^2}{2(-f(L))}\left(1-\exp\left(-\frac{2f(L)}{(\sigma^*)^2}(x-L)\right)\right). \tag{3.37}$$

For $x < 0$, we simply replace x by $|x|$ in (3.37) since $m(x)$ is symmetric. To summarize, we obtain the following uniformly valid expression when $\sigma^* \ll 1$,

$$m(x) \sim \left(1-\exp\left(-\frac{2f(L)}{(\sigma^*)^2}(|x|-L)\right)\right)m_{\max}, \text{ where} \tag{3.38}$$

$$m_{\max} = \frac{\sigma^*}{2(-f(L))}\sqrt{\frac{\pi}{-f'(0)}}\exp\left(-\frac{2}{(\sigma^*)^2}\int_0^L f(s)ds\right). \tag{3.39}$$

Specializing to (3.33) we have obtain, after some algebra,

$$m(x) \sim \left(1-\exp\left(\frac{2\tanh(2L)}{(\sigma^*)^2}(|x|-L)\right)\right)m_{\max}, \quad \sigma^* \to 0, \tag{3.40}$$

$$m_{\max} = \sqrt{2\pi}\frac{\cosh(2L)}{8\sinh(2L)}\sigma^*\exp\left\{\frac{2}{\sigma^*}\log\left(1+\tanh^2 L\right)\right\}. \tag{3.41}$$

As can be seen from (3.41), $m_{\max}$ increases exponentially as $\sigma^* \to 0$.

Case B: large L. We estimate, for $x > 0$:

$$f(x) \sim -\frac{2}{1+e^{2L-2x}}$$

and in particular $f(x) \sim 0$ for $|x| \ll L$. We then estimate

$$\int_0^x f(x) \sim -\log\left(1+e^{2(x-L)}\right) \sim \begin{cases} 0, & x \ll L \\ -\log(2) + -(x-L), & x \text{ near } L \end{cases}.$$

This yields the following uniform expansion for v_h :

$$v_h = \exp\left[\frac{2\log\left(1+e^{2(x-L)}\right)}{(\sigma^*)^2}\right] \sim 1+\exp\left(\frac{2\log(2)}{(\sigma^*)^2}\right)\exp\left(\frac{2}{(\sigma^*)^2}(x-L)\right).$$

We then estimate, for $x > 0$,

$$\int_0^x \frac{1}{v_h(s)}ds \sim x$$

and

$$\begin{aligned}\int_x^L \left\{v_h(x)\int_0^x \frac{1}{v_h(s)}ds\right\}dx. &\sim \int_x^L \{v_h(x)x\}\,dx \\ &\sim \int_x^L xdx + \int_x^L \exp\left(\frac{2\log(2)+2(x-L)}{(\sigma^*)^2}\right)Ldx \\ &\sim \frac{L^2-x^2}{2} + \exp\left(\frac{2\log(2)}{(\sigma^*)^2}\right)\frac{(\sigma^*)^2}{2}L\left\{1-\exp(2(x-L)/(\sigma^*)^2\right\}.\end{aligned}$$

In conclusion, we obtain

$$m(x) \sim \frac{L^2 - x^2}{(\sigma^*)^2} + \exp\left(2\frac{\log(2)}{(\sigma^*)^2}\right) L\left\{1 - \exp(2(|x| - L)/(\sigma^*)^2\right\} \tag{3.42}$$

and in particular

$$m(0) \sim \frac{L^2}{(\sigma^*)^2} + 2\exp\left(\frac{2\log(2)}{(\sigma^*)^2}\right) L, \quad L \gg O(1). \tag{3.43}$$

Formula (3.43) is shown in Figure 3.4 (top right). Note the parabolic shape on top of an exponential layer, as predicted by the asymptotics (3.42).

While $m(x)$ gives the mean of the hitting time distribution, the distribution itself does not concentrate around the mean. Figure 3.4 (bottom) shows the hitting time probability distribution obtained using Monte-Carlo simulations. We simulated (3.4) 10,000 times starting with $x(0) = 0$, until x collided with a boundary $x = \pm L$. The time of collision for each simulation is recorded, and the resulting histogram for 10,000 simulations is shown in Figure 3.4 (bottom). The value of $m(0)$ is approximated by the average of these simulations. In Figure 3.4 bottom left, we used the forward Euler method with stepsize $ds = 10^{-3}$ in the simulations. The average of these simulations is $m_{Monte-Carlo}(0) = 23.1$. The exact result (3.36) gives $m_{exact}(0) = 21.97$ whereas the asymptotic result (3.40) is $m_{asympt}(0) = 19.48$, a 13% difference. In Figure 3.4 bottom right, we used $ds = 10^{-2}$; and obtained $m_{Monte-Carlo}(0) = 1429$. The exact result (3.36) gives $m_{exact}(0) = 1203.7$ whereas the asymptotic result (3.43) yields $m_{asympt}(0) = 1380$, a 15% difference. Overall, good agreement between exact results, Monte-Carlo results and asymptotics is observed.

The error between m_{exact} and $m_{Monte-Carlo}$ depends on the number N of simulations used. While the error analysis is outside the scope of this thesis, numerics indicate that it scales like $O(1/\sqrt{N})$, which is typical of Monte-Carlo simulations in general. The error between m_{exact} and $m_{Monte-Carlo}$ depends on both σ^* and L in a complex way depending on the relative scaling of L and σ^*. Numerics indicate that with σ^* fixed, formula (3.43) has a relative error of $O(1/L)$ as $L \to \infty$, whereas formula (3.40) has a relative error that decays exponentially in σ^* for fixed L and with $\sigma^* \to 0$.

3.4 Discussion

We have investigated the effect of noise on the motion of a single spike in the GM model. We formulated a SODE describing the reduced spike motion then used it to describe the spike distribution of a spike inside the domain and the mean first passage time for the spike to hit the boundary. This only scratches the surface of many novel phenomena that are possible when noise is present, and many open problems remain. We conclude with proposing several below.

When a spike hits the boundary, it gets "stuck" there. However it can also get "unglued" from the boundary as well as illustrated in Figure 3.5. While we used MFPT theory to predict how long it takes for the spike to "hit" the boundary, we cannot explain why it gets "unglued" or how long it takes for the spike to unglue.

In this paper, we added noise to the activator equation because it induces random spike motion. Numerical experiments indicate that noise in the inhibitor does not affect spike motion very much; instead, it induces spike oscillations. This is an interesting problem left for future study.

We studied in detail multiplicative noise (3.2), where the spatiotermoral noise is premultiplied by u. This type of noise assures that the randomness affects only the spike itself and has no effect outside the spike, since u decays exponentially away from spike center. One can also consider additive noise, where the noise is added to the background independent of spike height, as follows:

$$\begin{cases} u_t = \varepsilon^2 u_{xx} - u + u^2/v + \sigma W \frac{\sqrt{dt}}{dt}, \qquad 0 = v_{xx} - v + \frac{u^2}{\varepsilon} \\ u_x = v_x = 0 \text{ at } x = \pm L. \end{cases} \tag{3.44}$$

Using the analysis of section 3.1, the spike posititon then satisfies the SODE (3.4), with σ^* given by (3.25). The resulting density distribution, as derived in (3.27), is given by

$$\rho = \frac{C}{\left(\cosh(2x_0) + \cosh(2L)\right)^2} \exp\left(-\frac{\varepsilon}{15L\sigma^2} \frac{\sinh^2(2L)}{\left(\cosh\left(2x_0\right) + \cosh\left(2L\right)\right)^2}\right).$$

It is qualitatively similar to the multiplicative case (3.6). The difference is that adding background noise affects not just the spike motion but spike stability as well – something that the reduced SODE or density (3.44) does not capture, especially in the case of multiple spikes. Figure 3.6 shows simulations for different levels of

additive noise and domain size. Many new phenomena are observed, including spike death, spike insertion, and "switching" behaviour. These are very interesting open problems left for future study.

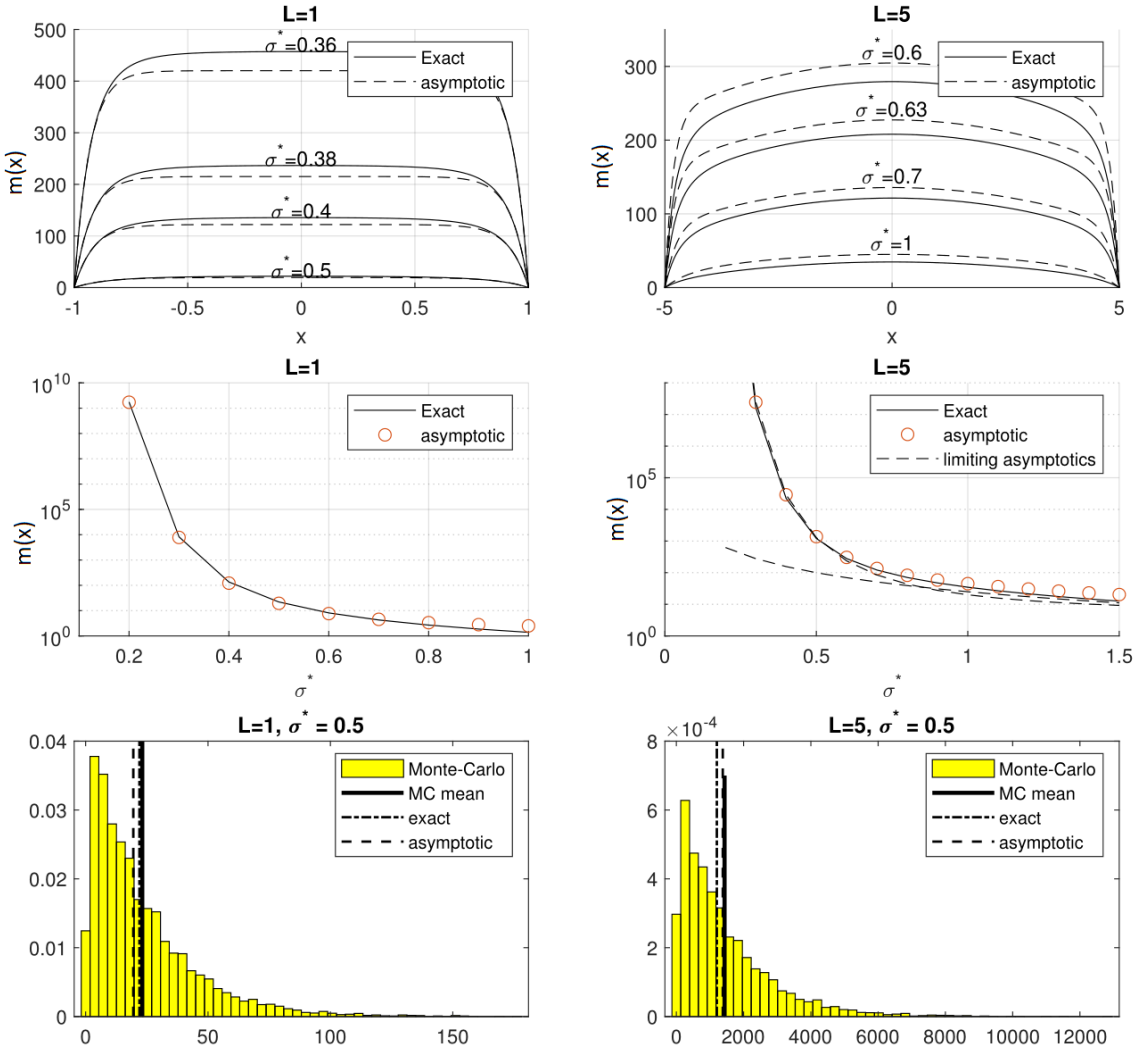

Figure 3.4: Top row: mean first passage time $m(x)$ for $L = 1$ and $L = 10$ for several σ^* as shown. Note the parabolic profile on top of an exponential layer when $L = 5$ and $\sigma \geq 0.5$. Middle row: graph of $m(0)$ for $L = 1$ and $L = 5$ as a function of σ^*. Bottom row: the full distribution of hitting times obtained by Monte-Carlo simulations of (3.4). MC-mean refers to the average of these simulations. Exact result is $m(0)$ given by (3.36). Asymptotic line is given by (3.40) for $L = 1$ and by (3.42) for $L = 5$.

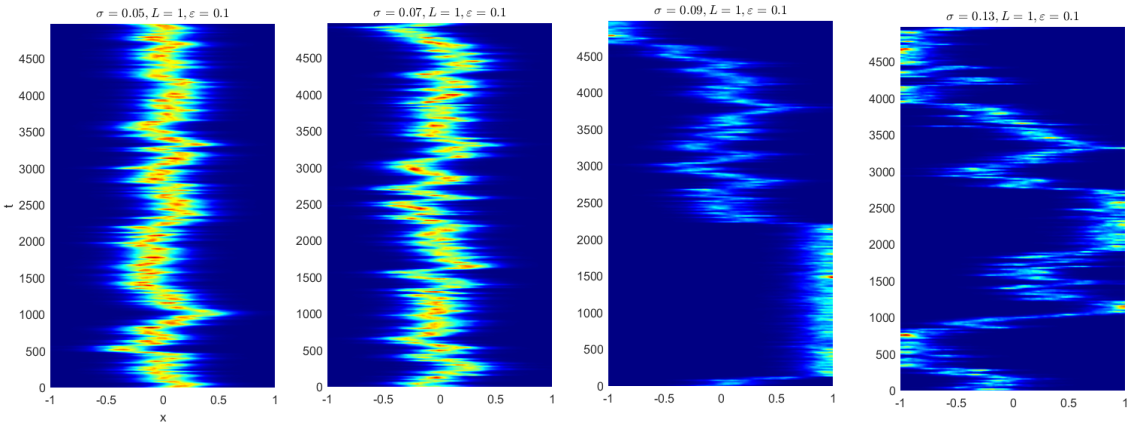

Figure 3.5: Simulation of (3.2) for several different σ as indicated. As σ is increased, the spike collides with the boundary. It can stay at the boundary for a long time but eventually becomes "unglued". The higher the σ value, the shorter time the spike spends at the boundary. The spike still retains its shape even for larger σ.

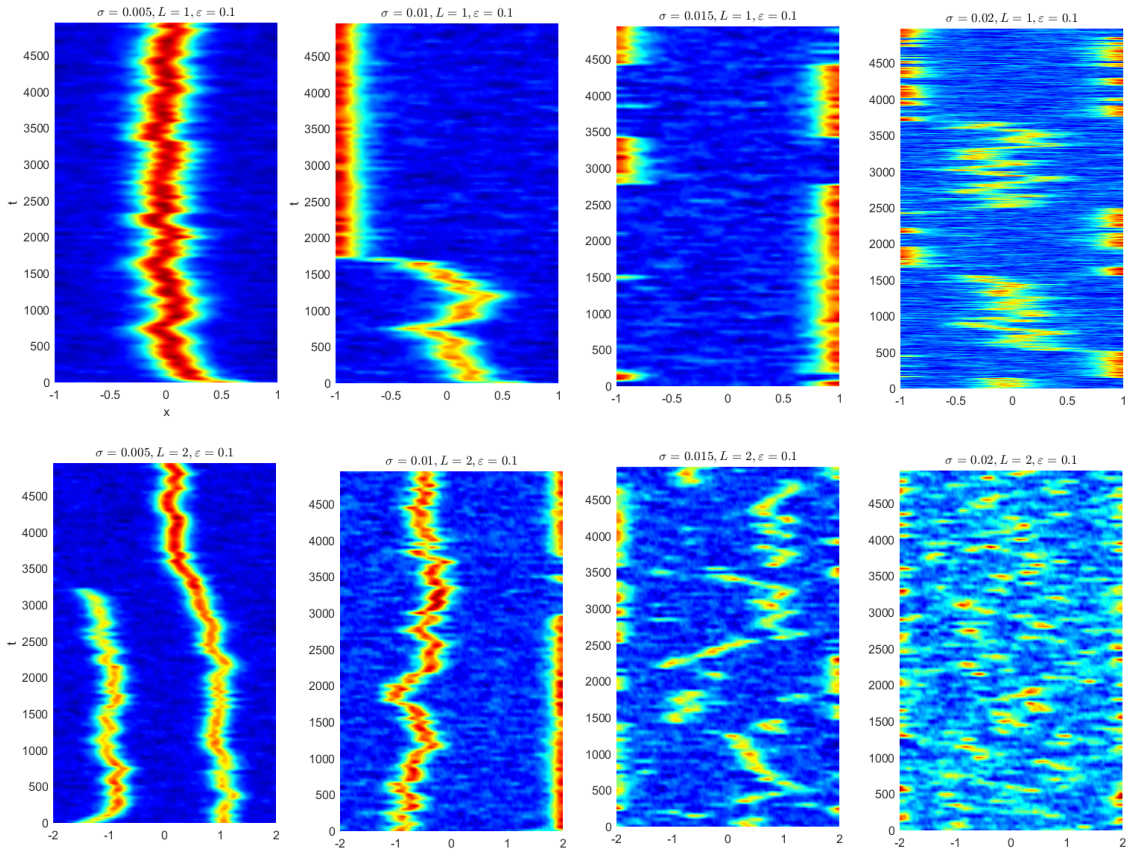

Figure 3.6: Simulation of (3.44) for two different domain sizes and various σ as indicated. Depending on domain length and noise level, many interesting phenomena are observed including boundary switching (top row, pane 3), spike death (bottom row, left), and chaotic dynamics (bottom right)

Chapter 4

Resource-mediated competition between two plant species with different rates of water intake

Competition for resources has long been regarded as one of the main mechanisms in structuring plant communities and natural selection [116, 117, 118]. In particular, in the semiarid regions where water resource is limited, the sparsity of water can lead to self-organised vegetation patterns such as vegetation patches and stripes [5, 7, 8, 9, 119, 6]. These patterns can be thought of as a transition state from full vegetation to a desert state [77, 120, 7, 121, 122, 6].

In this paper, we look at competition for water between two plant species with different water absorption rates in the water-limited regime, where the vegetation forms in patches. We are interested in how the competition for water affects co-existence and stability of patches of different plant species. We consider two plant species: a "thirsty" species and a "frugal" species that only differ by the amount of water they consume, while being identical in all other aspects.

Our starting point is the following variant of the Klausmeier model (1.9), incorporating two plant species and water-mediated competition between them:

$$\begin{aligned} \partial_t u_1 &= D_u \partial_{xx} u_1 - \mu u_1 + \gamma u_1^2 v, \\ \partial_t u_2 &= D_u \partial_{xx} u_2 - \mu u_2 + \gamma u_2^2 v, \\ \partial_t v &= D_v \partial_{xx} v + a - c_1 u_1^2 v - c_2 u_2^2 v. \end{aligned} \tag{4.1}$$

Here, the effect of evaporation is ignored. u_1 and u_2 represent plant densities of the two types of plants and v denotes the concentration of the water in the soil. For simplicity and concreteness, we will consider their dynamics to be identical, except for the amount of water consumed per unit growth. We take these dynamics as originally suggested by Klausmeier [5]. In the absence of water, the plants wither with a rate μ. They grow at the same rate $\gamma u_i v$ in the presence of water. Plants "diffuse" through seed dispersal in proportion to the diffusion constant D_u. The water diffuses through

the soil according to the diffusion constant D_v. The constants c_1, c_2 represent the amount of water intake needed to grow at a given rate γ. The term a represents water precipitation. The plant species u_1 is more thirsty than u_2 if $c_1 > c_2$.

By rescaling, we reduce (4.1) to the following non-dimensional form [1]

$$\begin{aligned} \partial_t u_1 &= \varepsilon^2 \partial_{xx} u_1 - u_1 + u_1^2 v, \\ \partial_t u_2 &= \varepsilon^2 \partial_{xx} u_2 - u_2 + u_2^2 v, \\ \tau \partial_t v &= D \partial_{xx} v + a - \frac{u_1^2 v}{\varepsilon} - \beta \frac{u_2^2 v}{\varepsilon}, \end{aligned} \tag{4.2}$$

which we will refer to as the "two-species vegetation model". Here, $\beta = c_2/c_1$ is the ratio of the water intake rates. In what follows, we will assume that $D \gg O(\varepsilon^2)$ and τ is sufficiently small that the term $\tau \partial_t v$ doesn't affect the dynamics and can be discarded to leading order. In terms of the original variables, these assumptions reflect the fact that the "diffusion" of plants through seed dispersal is on a much slower scale than the water diffusion through the soil. We will also assume Neumann boundary conditions on a domain $x \in (-L, L)$:

$$\partial_x u_1(\pm L) = \partial_x u_2(\pm L) = \partial_x v(\pm L) = 0. \tag{4.3}$$

The ratio β indicates how thirsty plant species u_1 is compared to u_2. When $\beta < 1$, the species u_2 consumes less water than u_1, and the opposite is true when $\beta > 1$. Without loss of the generality, we may also assume that $0 < \beta \leq 1$, so that u_1 is more thirsty (per unit growth) than u_2 : u_1 is the "thirsty" species whereas u_2 is the "frugal" species in such a case.

When $\beta = 1$, the two species are indistinguishable from each-other, and the model (4.2) *behaves* like the "classical" Schnakenberg model [27, 28],

$$\partial_t u = \varepsilon^2 \partial_{xx} u - u + u^2 v, \qquad \tau \partial_t v = D \partial_{xx} v + a - \frac{u^2 v}{\varepsilon} \tag{4.4}$$

where $u = u_1 + u_2$ (this model is itself a special case of the Klausmeier model).

In this paper, we will be concerned with the following parameter regime

$$0 < \varepsilon \ll 1, \quad \tau = 0, \quad D, a = O(1). \tag{4.5}$$

[1] Take $\mu = 1$ by rescaling the time variable t and relabelling parameters. Next, let $\varepsilon := \sqrt{D_u}$ and rescale $u_1 = \hat{u}_1 \frac{1}{c_1 \varepsilon}$, $u_2 = \hat{u}_2 \frac{1}{c_1 \varepsilon}$, $v = \frac{\hat{v} c_1 \varepsilon}{\gamma}$, $a = \frac{\hat{a}}{\gamma}$. Dropping the hats yields (4.2) with $\tau = \varepsilon c_1$, $D = D_v \varepsilon c_1$.

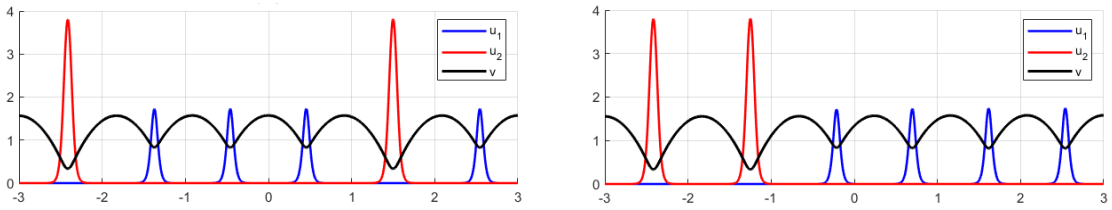

Figure 4.1: Two steady states of (4.2), consisting of $k_1 = 4$ spikes of type u_1 (blue) and $k_2 = 2$ spikes of type u_2 (red). Parameters are $\varepsilon = 0.025, a = 8, L = 3, D = 1, \beta = 0.5$. The spike heights and profiles are the same for each type, regardless of the spike ordering.

The assumption $\tau = 0$ can be replaced with "$\tau \ll D$" without any change in the results.

It is well documented that Schnakenberg model (4.4) admits spot solutions having N concentrations in u [28, 27]. More generally, similar results for spike-stability analysis are obtained in singularly perturbed two-component reaction diffusion systems such as Schnakenberg model, Gierer-Meinhardt model [63, 3], and the Gray-Scott model [33, 98, 97, 36]. However there are important differences both in the analysis and in the stability results for the 3-component system when $\beta \neq 1$.

The two-species model (4.2) inherits spike solutions from (4.4), but has a much richer structure. Indeed, given any two non-negative integers k_1, k_2, there exist a solution with a total $N = k_1 + k_2$ spikes corresponding to k_1 spikes in u_1 and k_2 spikes in u_2. We shall refer to this as a (k_1, k_2) pattern.

At first glance, given N spikes, there is a total of 2^N possible ways to choose their type (each spike can be either u_1 or u_2-type). One might then think that there is a total of 2^N possible patterns with different spike height and radius. However it turns out that the spike *ordering* of spots does not matter: only the total number of each type matters. As such, there are $N + 1$ patterns with distinct spike heights for fixed N. This is illustrated in Figure 4.1 which shows two distinct orderings for same number of parameters and number of spikes. Both orderings, however, have the same height and profile for the spikes u_1 and u_2.

In Figure 4.1, the "thirsty" patches are shown in blue and correspond to u_1 whereas the "frugal" patches are in red, corresponding to u_2. Note that the frugal plants have bigger height; this is because they absorb less water per unit growth and hence there is more water remaining for them to grow more.

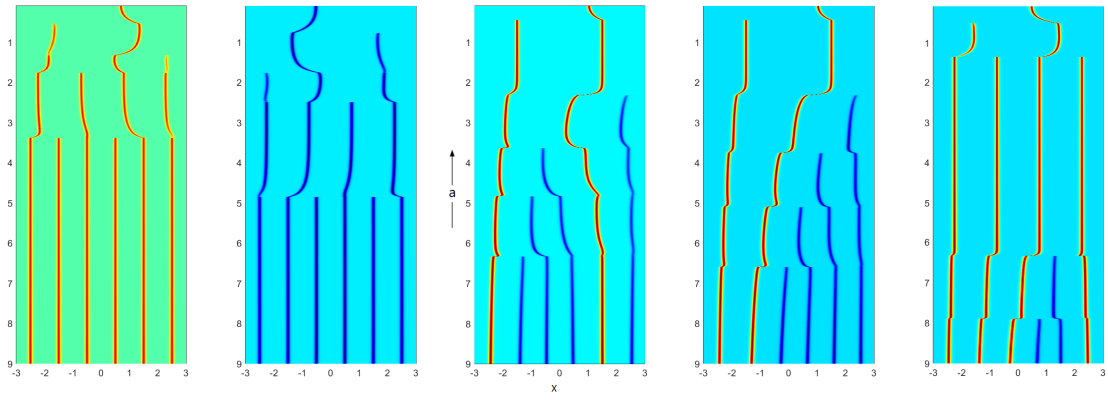

Figure 4.2: Spike death as a is decreased. Here, $a = 10 - 10^{-5}t$ and other parameters are $\beta = 0.5, L = 3, D = 1, \varepsilon = 0.025$. Color plot of u_1 ("thirsty", in blue) and u_2 ("frugal", in red) is shown as a function of a. The subpanels only differ in initial conditions, and are arranged from most resilient pattern (on the left) to least-resilient pattern (on the right). Note that a pattern of all-frugal patches is the most resilient, followed by all-thristy, and then mixed patterns.

As rainfall rate a is decreased, competition for water between the plants triggers the collapse of one of the spikes in the overall pattern. This process is illustrated in Figure 4.2, which shows that as a is decreased, the *thirsty* spikes (in blue, corresponding to u_1) die out *first,* until only "frugal" species (u_2, in red) remains. Our main goal is to study stability of this N-spike equilibria. In particular, we derive the corresponding eigenvalue problem and consider both the small eigenvalues of order $O(\varepsilon^2)$ and large eigenvalues of order $O(1)$.

We now illustrate our main results. There are three thresholds that can affect the existence and stability of (k_1, k_2) spike patterns. One is the large eigenvalue threshold a_l such that the large eigenvalue becomes unstable as a decreases below a_l. The other two thresholds are small eigenvalue thresholds associated with either intraspecific competition (i.e., competition within u_1 or u_2 type) or interspecific competition (i.e., competition between u_1 and u_2 type). The intraspecific competition threshold is denoted by the fold point a_f and the interspecific competition threshold is denoted by a_s. The maximum of these three critical values gives the competition instability threshold a^*, which triggers the collapse of plant patches. By comparing a_l, a_f and a_s, we find that a_s is the dominant instability threshold for almost all (k_1, k_2) patterns except the case where only one *thirsty* spike exists (i.e., $(1, N-1)$ patterns with

$\beta < 1$ and $(N-1,1)$ patterns with $\beta > 1$) and the dominant instability threshold is a_f. This result is illustrated in Table 4.1, where the three thresholds a_f, a_s and a_l for different (k_1, k_2) patterns are computed. The large eigenvalue threshold a_l is *dependent* of spike orderings, while the other two are not. Therefore a_f, a_s are unique for each pattern while a_l is different for different spike orderings. In Table 4.1, we compute the maximum of a_l and compare it with other thresholds in all types of 5-spike patterns and 6-spike patterns, and it can be seen that the instability threshold a^* (maximum in each column) is given by either a_s or a_f. Note that the large eigenvalue threshold may not exist under given parameter values such as the $(1,4)$ pattern in Table 4.1, which means the $(1,4)$ pattern is always stable for the large eigenvalues.

For fixed N, we compared the instability threshold a^* for different (k_1, k_2) spike patterns, and found that the plant with smaller water intake rate is more competitive. If $\beta < 1$ (i.e. $c_2 < c_1$), then u_2 is more competitive and one u_1-type spike will get killed when bifurcation happens unless the pattern only contains u_2-type spike initially. Otherwise u_1 is more competitive and one u_2-type spike will get killed when bifurcation occurs. Moreover, among the $N+1$ combinations of spike patterns, homogeneous spike patterns (i.e.,$(0,N)$ pattern or $(N,0)$ pattern) are always more stable than mixed-spike patterns. These results are shown in Table 4.2, where the instability thresholds in terms of a are given for each (k_1, k_2) pattern. A smaller threshold a^* suggests that the corresponding pattern is more stable. As we see in Table 4.2, the first number in each column is the minimum, which indicates that for fixed N, $(0,N)$ is the most stable pattern given that $\beta < 1$. Moreover, for mixed N-spike patterns, the more "frugal" spikes the pattern contains, the more unstable the pattern is.

A summary of this chapter is as follows. We construct the N spike equilibrium of system (4.2) in Section 4.1. In Section 4.2 we analyze the stability of the N-spike equilibrium with respect to the large eigenvalues by deriving the corresponding nonlocal eigenvalue problem (NLEP), as well as the small eigenvalues by looking at asymmetric branches. The stability analysis is very similar to [27, 28] but with some key differences. We then show that the instability due to small eigenvalues is the dominant instability. In Section 4.3 we use numerics to explore what happens in the high-precipitaiton regime of large a, and we conclude with some open questions.

thresholds \ 5-spike patterns	(4,1)	(3,2)	(2,3)	(1,4)
a_s	4.3372	4.9778	5.6471	2.3655
$\max(a_l)$	4.1362	4.7233	5.4138	DNE
a_f	2.3894	4.1053	5.3282	6.2754

thresholds \ 6-spike patterns	(5,1)	(4,2)	(3,3)	(2,4)	(1,5)
a_s	5.5649	6.2585	6.9725	7.7247	3.1677
$\max(a_l)$	5.3832	6.0649	6.7470	7.4579	DNE
a_f	2.6816	4.7327	6.2608	7.4492	8.4342

Table 4.1: Instability thresholds a_f, a_s and $\max(a_l)$ in N-spike patterns with $N = 5, 6$. The critical values in red are maximum in each column, which are the competition instability threshold a^* that triggers the collapse of one spike in the overall pattern. The parameters are $L = 3, \beta = 0.5, D = 1$.

4.1 Construction of N-spike solutions

In this section, we construct N-spike equilibria of system (4.2), which contains k_1 u_1-spikes and k_2 u_2-spikes. Since the patterns with fixed k_1, k_2 have same height and profile for u_1 and u_2, without loss of generality, we consider all u_1-type spikes located on the left side and all u_2-type spikes located on the right side. Since the same type of spikes has a common height and equal spacing, we define the radius of u_1-type spike as l_1 and the radius of u_2-type spike as l_2. So that l_1, l_2 satisfies

$$k_1 l_1 + k_2 l_2 = L. \tag{4.6}$$

To construct an N-spike solution, we first look at the inner region, where we introduce the inner variable

$$y = \frac{x - x_j}{\varepsilon},$$

in which x_j is the location of j-th spike. After collecting leading order terms we have

$$\begin{aligned} u_{1yy} - u_1 + u_1^2 v &= 0, \\ u_{2yy} - u_2 + u_2^2 v &= 0, \\ v_{yy} &= 0. \end{aligned} \tag{4.7}$$

$a^*_{(k_1,k_2)}$ k_1 \ N	2	3	4	5	6
0	0.67	1.22	1.89	2.64	3.46
1	1.20	2.63	4.33	6.28	8.43
2	0.94	2.21	3.80	5.65	7.72
3		1.73	3.22	4.98	6.98
4			2.67	4.34	6.26
5				3.73	5.56
6					4.90

Table 4.2: Theoretical predictions for competition instability thresholds a^* with parameters $L = 3, \beta = 0.5, D = 1$. The critical values in blue indicates the most stable patterns in each column, while the critical values in red correspond to most unstable patterns. See also Figure 4.2 for comparison with numerics.

Solving system (4.7) yields

$$u_1 = \frac{1}{v_1}\sum_{j=1}^{k_1} w\left(\frac{x-x_j}{\varepsilon}\right), u_2 = \frac{1}{v_2}\sum_{j=k_1+1}^{N} w\left(\frac{x-x_j}{\varepsilon}\right), \tag{4.8}$$

in which $v_1 = v(x_j)$ with $j = 1...k_1$ and $v_2 = v(x_j)$ with $j = k_1 + 1...N$, and $w(y)$ is the "ground state" profile satisfying

$$w'' - w + w^2 = 0, \quad w'(0) = 0, \quad w(y) > 0, \quad w(y) \to 0 \text{ as } y \to \infty; \tag{4.9}$$

it has a well-known explicit solution

$$w(y) = \frac{3}{2}\text{sech}^2\left(\frac{y}{2}\right). \tag{4.10}$$

In the outer region, the terms that involve u_1, u_2 can be estimated as delta functions. Therefore, v satisfies

$$Dv_{xx} + a = \frac{6}{v_1}\sum_{j=1}^{k_1}\delta(x-x_j) + \frac{6\beta}{v_2}\sum_{j=k_1+1}^{N}\delta(x-x_j), v_x(\pm L) = 0. \tag{4.11}$$

Here we have used the fact that $\int_{x_j^-}^{x_j^+}\frac{u_1^2 v}{\varepsilon}dx = \frac{6}{v_1}$ for $j = 1, \cdots k_1$ and $\int_{x_j^-}^{x_j^+}\frac{u_2^2 v}{\varepsilon}dx = \frac{6}{v_2}$ for $j = k_1 + 1, \cdots N$. Integrating equation (4.11) over $(-L, L)$ and imposing that $k_1 l_1 + k_2 l_2 = L$, we obtain

$$v_1 = \frac{3}{al_1}, v_2 = \frac{3\beta}{al_2}, \tag{4.12}$$

in which l_1, l_2 are to be determined. We then solve equation (4.11) by introducing the Green's function $G(x; x_j)$ and let

$$v(x) = \bar{v} + \frac{6}{v_1}\sum_{j=1}^{k_1} G(x; x_j) + \frac{6\beta}{v_2}\sum_{j=k_1+1}^{N} G(x; x_j) \tag{4.13}$$

for some constant $\bar{v}$ to be determined. Here $G(x; x_j)$ satisfies

$$DG_{xx}(x; x_j) + \frac{1}{2L} = \delta(x - x_j), G_x(\pm L; x_j) = 0, \int_{-L}^{L} G(x; x_j) = 0, \tag{4.14}$$

which has the following solution

$$G(x; x_j) = -\frac{1}{4DL}(x^2 + x_j^2) + \frac{1}{2D}|x - x_j| - \frac{L}{6D}, j = 1, \cdots N. \tag{4.15}$$

The constant $\bar{v}$ is then determined by the matching condition $v(x_j) = v_1, j = 1, \cdots k_1$:

$$\bar{v} = v_1 - \frac{6}{v_1}\sum_{j=1}^{k_1} G(x_1; x_j) - \frac{6\beta}{v_2}\sum_{j=k_1+1}^{N} G(x_1; x_j). \tag{4.16}$$

It remains to find the radius of spikes l_1, l_2. For the patterns that only contain u_1-type or u_2-type spike (i.e., $(0, N)$ or $(N, 0)$ pattern), it is easy to see that $l_1 = l_2 = \frac{L}{N}$. For mixed-spike cases, we proceed by matching the outer solution (4.13) with the inner ones $v(x_j) = v_1, j = 1, \cdots k_1$, $v(x_j) = v_2, j = k_1 + 1, \cdots N$; then we obtain

$$v_1 = \bar{v} + \frac{6}{v_1}\sum_{j=1}^{k_1} G(x_1; x_j) + \frac{6\beta}{v_2}\sum_{j=k_1+1}^{N} G(x_1; x_j), \tag{4.17}$$

$$v_2 = \bar{v} + \frac{6}{v_1}\sum_{j=1}^{k_1} G(x_N; x_j) + \frac{6\beta}{v_2}\sum_{j=k_1+1}^{N} G(x_N; x_j). \tag{4.18}$$

Note that the same type of spikes has a common height and equal spacing, so that

$$x_j = \begin{cases} -L + (2j-1)l_1, & j = 1, \cdots k_1, \\ L - (2(N-j+1)-1)l_2, & j = k_1 + 1, \cdots N. \end{cases} \tag{4.19}$$

Subtracting equation (4.17) from (4.18) and simplifying using equation (4.12), (4.13), and (4.15), we get

$$\frac{3\beta}{al_2} - \frac{3}{al_1} = \frac{a}{2D}(l_1^2 - l_2^2). \tag{4.20}$$

In the end, we eliminate l_1 by combining the condition $k_1 l_1 + k_2 l_2 = L$ and equation (4.20); then we obtain the following polynomial for l_2:

$$f(l_2) = e l_2^4 + p l_2^3 + q l_2^2 + r l_2 + s = 0 \tag{4.21}$$

where

$$e = (k_1^2 - k_2^2), p = 3Lk_2 - \frac{k_1^2 L}{k_2}, q = -3L^2, r = \frac{6D\beta k_1^2}{a^2} + \frac{6Dk_1^3}{a^2 k_2} + \frac{L^3}{k_2}, s = -\frac{6D\beta L k_1^2}{a^2 k_2}, \tag{4.22}$$

and l_1 can be found through $l_1 = \frac{L - k_2 l_2}{k_1}$. We summarize our results as following:

Result 4.1.1 *In the limit $\varepsilon \to 0$, system (4.2) has N-spike equilibrium solution that contains k_1 u_1-spikes and k_2 u_2-spikes, in which $k_1 \geq 0$, $k_2 = N - k_1$:*

$$u_{1e}(x) = \sum_{j=1}^{k_1} \frac{w\left(\frac{x - x_j}{\varepsilon}\right)}{v_1}, \tag{4.23}$$

$$u_{2e}(x) = \sum_{j=k_1+1}^{N} \frac{w\left(\frac{x - x_j}{\varepsilon}\right)}{v_2}, \tag{4.24}$$

$$v_e(x) = \bar{v} + \frac{6}{v_1} \sum_{j=1}^{k_1} G(x; x_j) + \frac{6\beta}{v_2} \sum_{j=k_1+1}^{N} G(x; x_j). \tag{4.25}$$

Here $w(y) = \frac{3}{2}\mathrm{sech}^2\left(\frac{y}{2}\right)$, and $v_1, v_2, G(x; x_j), \bar{v}$ and x_j are given in (4.12), (4.15), (4.16), (4.19), respectively, in which l_2 can be evaluated through equation (4.21) and $l_1 = \frac{L - k_2 l_2}{k_1}$.

4.1.1 Fold point of N-spike equilibrium

The N-spike equilibrium has a fold point $a_f(k_1, k_2)$, corresponding to a double root of the polynomial (4.21) (also referred to as the discriminant of the polynomial). It can be obtained by solving a polynomial system

$$f(l_2) = 0, f'(l_2) = 0.$$

We used Maple's grobner basis package to derive the following expression for the fold point:

$$\begin{aligned}\Delta(a) = &-256e^3s^3 + 192e^2prs^2 + 128e^2q^2s^2 - 144e^2qr^2s + 27e^2r^4 - 144ep^2qs^2 + 6ep^2r^2s \\ &+ 80epq^2rs - 18epqr^3 - 16eq^4s + 4eq^3r^2 + 27p^4s^2 - 18p^3qrs + 4p^3r^3 + 4p^2q^3s \\ &- p^2q^2r^2,\end{aligned} \tag{4.26}$$

where e, p, q, r, s satisfy (4.22). Then $a_f(k_1, k_2)$ can be obtained by solving $\Delta(a_f(k_1, k_2)) = 0$ numerically.

Note that equation (4.21) is a fourth order polynomial when $k_1 \neq k_2$. When $k_1 = k_2$, it becomes a cubic polynomial and the discriminant (4.26) simplifies to

$$\Delta(a) = 27p^4s^2 - 18p^3qrs + 4p^3r^3 + 4p^2q^3s - p^2q^2r^2. \tag{4.27}$$

An example of a fold point with $k_1 = k_2 = 2$ is given in Figure 4.4. There are three solutions for $a > a_f$ and only one for $a < a_f$. By solving the full system (4.2) numerically, we observe that the second branch is stable when $a > a_f$; there are no stable solutions for $a < a_f$. As a consequence, the fold point a_f corresponds to one instability threshold of the system. Note that in the classical vegetation model where $\beta = 1$, the radius is unique, which is $l_1 = l_2 = \frac{L}{N}$. This matches our result shown in the right panel of Figure 4.4, where as $\beta = 1$, both the radius l_2 and l_1 are equal to $\frac{L}{2} = 0.75$.

4.2 Stability analysis

In this section, we analyse the stability of N-spike patterns constructed in Section 4.1. Section 4.1.1 shows that there are three or four branches (depending on whether $k_1 = k_2$ or not) corresponding to different equilibria. In this paper we only consider and compute stability thresholds of the stable branch such as the middle branch in Figure 4.4. We will first compute the bifurcation point where an asymmetric pattern bifurcates from the symmetric branch of u_1 or u_2-spike; this threshold characterizes the stability threshold of an N spike equilibria with respect to the small eigenvalues with $\lambda \to 0$ as $\varepsilon \to 0$. We will then derive a Nonlocal Eigenvalue Problem (NLEP) which determines the stability of the large eigenvalue ($O(1)$). Note that the large

eigenvalue threshold can be affected by the order of the spikes, so in section 4.2.2 we consider spike steady state in general orderings. Numerical simulations are used to validate our stability results.

4.2.1 Asymmetric branches and competition instability thresholds

The primary mechanism that drives spike instability in one-dimensional reaction diffusion models corresponds to a small-eigenvalue bifurcation [27, 28, 100]. Instead of computing fully the small eigenvalues, it was shown in [27, 28] that this bifurcation point (at which there is a zero small eigenvalue) is characterized precisely by an emergence of an asymmetric solution (e.g., two spikes of unequal height) off the symmetric branch (i.e., spikes of equal height). As expected, our two-component system inherits a similar structure, except that it has two such bifurcation points: one for each type of species which we denote by a_{s1}, a_{s2}. By taking the maximum of the two, we will obtain the bifurcation threshold $a_s = \max(a_{s1}, a_{s2})$ which is responsible for destabilization of the (k_1, k_2) pattern.

The key to computing a_{s1}, a_{s2} is to compute the value of v where $v' = 0$. These points occur inbetween any two consecutive spikes. From (4.13) we have

$$\begin{aligned} v(x_j + l_1) &\sim \tfrac{al_1^2}{2D} + \tfrac{3}{al_1}, \quad \text{when } x_j \text{ is the center of } u_1, \\ v(x_j + l_2) &\sim \tfrac{al_2^2}{2D} + \tfrac{3\beta}{al_2}, \quad \text{when } x_j \text{ is the center of } u_2. \end{aligned} \tag{4.28}$$

Since the steady state $v(x)$ is continuous, we have the following relation

$$\frac{al_1^2}{2D} + \frac{3}{al_1} = \frac{al_2^2}{2D} + \frac{3\beta}{al_2}. \tag{4.29}$$

The bifurcation point for the emergence of an asymmetric u_1-spike or u_2-spike solution is obtained by calculating the minimum points in (4.28). This is given by setting $\frac{\partial}{\partial l_1}\left(\frac{al_1^2}{2D} + \frac{3}{al_1}\right) = 0$ or $\frac{\partial}{\partial l_2}\left(\frac{al_2^2}{2D} + \frac{3\beta}{al_2}\right) = 0$ for a_{s1} and a_{s2}, respectively. This yields

$$a_{s1} = \sqrt{\frac{3D}{l_1^3}}, \tag{4.30}$$

$$a_{s2} = \sqrt{\frac{3\beta D}{l_2^3}}. \tag{4.31}$$

Suppose that $\beta < 1$, then $l_1 < l_2$; it follows that $a_{s1} > a_{s2}$. Thus $a_s = a_{s1}$, and the spike annihilation within u_1-type spikes happens first. Similarly, we get $a_s = a_{s2}$ when

$\beta > 1$. For the case $\beta = 1$, we have $l_1 = l_2 = \frac{L}{N}$ so that $a_s = a_{s1} = a_{s2} = \sqrt{\frac{3DN^3}{L^3}}$. This recovers the threshold previously obtained in [27, 28] for the classical Schnakenberg model. The above computations assume that there are at least two spikes of type u_1 (or u_2) when $\beta < 1$ (or $\beta > 1$). In summary, we obtain

$$a_s = \begin{cases} \sqrt{\frac{3D}{l_1^3}}, & \text{when } \beta < 1 \text{ with } k_1 \geq 2, \\ \sqrt{\frac{3\beta D}{l_2^3}}, & \text{when } \beta > 1 \text{ with } k_2 \geq 2. \end{cases} \tag{4.32}$$

Note that the threshold (4.32) computes the competition within the same type of spikes, and it does not cover the competition between u_1 and u_2 spikes. Therefore, this result does not work for $(1, 1)$ pattern. However, as we compare a_s and a_f, which is obtained in Section 4.1.1, we found that $a_f < a_s$ when $\beta \neq 1$, and $a_f = a_s = \sqrt{\frac{3DN^3}{L^3}}$ when $\beta = 1$. This is shown in Figure 4.3, where we compared a_f and a_s for $(2, 2)$ and $(1, 2)$ patterns. We conjecture that a_f is another small eigenvalue threshold that corresponds to interspecific competition between u_1 and u_2 spikes.

There exist two special cases: either $k_1 = 1$ (i.e., $(1, N-1)$ spike patterns) with $\beta < 1$, or $k_2 = 1$ (i.e., $(N-1, 1)$ spike patterns) with $\beta > 1$. For these cases, $a_s < a_f$, so the dominant instability is triggered by the fold point a_f as computed in Section 4.1 instead of a_s. This is illustrated in Figure 4.3, where in the left panel ($(2, 2)$ pattern) $a_s = a_{s1} > a_f$, and the dominant threshold is a_s, while in the right panel ($(1, 2)$ pattern) $a_f > a_s = a_{s2}$, so the dominant threshold is a_f. This is further illustrated in Figure 4.2, which shows excellent agreement between numerics and theoretical results. For example, the last panel in Figure 4.2 shows that the first spike death is caused by $a_s = 7.7247$ in $(2, 4)$ pattern and the second spike death is caused by $a_f = 6.2754$ in $(1, 4)$ pattern. The theoretical thresholds a_s and a_f can be found in Table 4.1.

4.2.2 Large eigenvalues and nonlocal eigenvalue problem

In this section we compute the large $O(1)$ eigenvalues by deriving the corresponding eigenvalue problem. We start by linearizing around the steady state given in (4.23). That is, we let $u_1 = u_{1e} + e^{\lambda t}\phi, u_2 = u_{2e} + e^{\lambda t}\psi$ and $v = v_e + e^{\lambda t}\xi$. Note that here the (k_1, k_2) spike steady states are considered in general spike orderings without changing the profile of u_1 and u_2. Upon substituting into (4.2) and assuming that

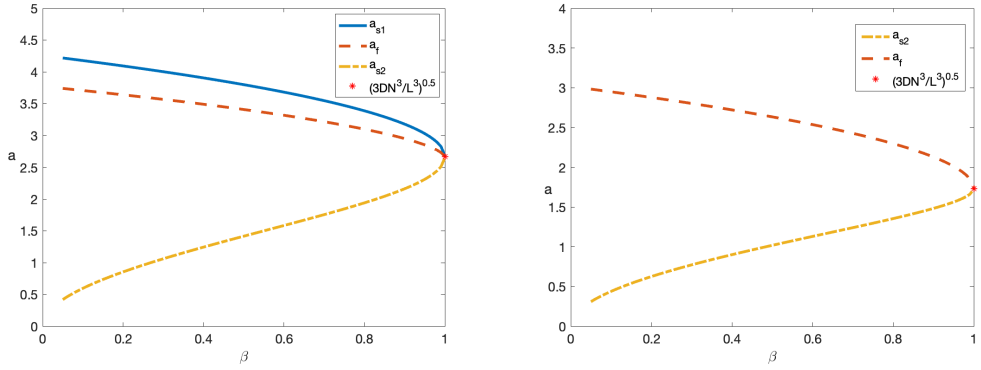

Figure 4.3: Plot of three thresholds a_f (4.26), a_{s1} (4.30) and a_{s2} (4.31) vs β for $(2,2)$ spike pattern (left panel) and $(1,2)$ spike pattern (right panel). In the left figure ($(2,2)$ pattern), $a_s = a_{s1}$ is the dominant instability threshold; while on the right figure ($(1,2)$ pattern), there is no competition within u_1 spike so only a_{s2} exists and $a_{s2} < a_f$, thus a_f is the dominant instability threshold. Here the parameters are $D = 1, L = 3$.

$|\phi| \ll 1, |\psi| \ll 1, |\xi| \ll 1$ we obtain the following eigenvalue problem

$$\lambda\phi = \varepsilon^2\phi_{xx} - \phi + 2u_{1e}v_e\phi + u_{1e}^2\xi, \quad \phi_x(\pm L) = 0, \tag{4.33a}$$

$$\lambda\psi = \varepsilon^2\psi_{xx} - \psi + 2u_{2e}v_e\phi + u_{2e}^2\xi, \quad \psi_x(\pm L) = 0, \tag{4.33b}$$

$$\tau\lambda\xi = D\xi_{xx} - \frac{1}{\varepsilon}\left[2u_{1e}v_e\phi + 2\beta u_{2e}v_e\psi + \left(u_{1e}^2 + \beta u_{2e}^2\right)\xi\right], \quad \xi_x(\pm L) = 0. \tag{4.33c}$$

Near the j-th spike, we change variables $x = x_j + \varepsilon y$. To leading order, we obtain $\xi(y) \sim \xi_j := \xi(x_j)$, and in the inner variables we have

$$\lambda\phi \sim \phi_{yy} - \phi + 2w\phi + \frac{w^2}{v_1^2}\xi_j, \tag{4.34a}$$

$$\lambda\psi \sim \psi_{yy} - \psi + 2w\psi + \frac{w^2}{v_2^2}\xi_j. \tag{4.34b}$$

Considering the different order of spikes in a (k_1, k_2) pattern, we look for an eigenfunction of the form

$$\Phi \sim \sum_{j=1}^{N} \Phi_j, \xi \sim \sum_{j=1}^{N} \xi_j$$

where

$$\Phi_j = \begin{cases} \phi_j = \phi\left(\frac{x-x_j}{\varepsilon}\right), & j\text{th spike is } u_1\text{-type}, \\ \psi_j = \psi\left(\frac{x-x_j}{\varepsilon}\right), & j\text{th spike is } u_2\text{-type}. \end{cases}$$

In the outer region, both ϕ and ψ are assumed to be localized functions so ξ satisfies

$$\xi_{xx} - \mu^2 \xi = \sum_{j=1}^{N} c_j \delta(x - x_j), \quad \xi_x(\pm L) = 0 \tag{4.35}$$

where $\mu = \sqrt{\frac{\tau\lambda}{D}}$ and c_j is defined as

$$c_j = \begin{cases} \frac{1}{D}\left(2\int_{-\infty}^{\infty} w\phi_j dy + \frac{6}{v_1^2}\xi_j\right), & j\text{th spike is } u_1\text{-type}, \\ \frac{\beta}{D}\left(2\int_{-\infty}^{\infty} w\psi_j dy + \frac{6}{v_2^2}\xi_j\right), & j\text{th spike is } u_2\text{-type}. \end{cases} \tag{4.36}$$

We first solve (4.35) and write $\xi(x)$ as

$$\xi = \sum_{j=1}^{N} c_j G^{(\mu)}(x; x_j), \tag{4.37}$$

where $G^{(\mu)}(x; x_j)$ satisfies

$$G^{(\mu)}_{xx}(x; x_j) - \mu^2 G^{(\mu)}(x; x_j) = \delta(x - x_j), \quad G^{(\mu)}_x(\pm L; x_j) = 0. \tag{4.38}$$

Solving (4.38) yields

$$G^{(\mu)}(x; x_j) = -\frac{1}{\mu \sinh(2\mu L)} \begin{cases} \cosh\left(\mu(x + L)\right)\cosh\left(\mu(x_j - L)\right), & x < x_j \\ \cosh\left(\mu(x_j + L)\right)\cosh\left(\mu(x - L)\right), & x > x_j. \end{cases} \tag{4.39}$$

Evaluating (4.37) at $x = x_j$, we obtain that

$$\xi(x_i) = \xi_i = \sum_{j=1}^{N} c_j G^{(\mu)}_{i,j},$$

where $G^{(\mu)}_{i,j} = G^{(\mu)}(x_i; x_j)$ is given in (4.39). In matrix form, it can be written as

$$\vec{\xi} = \mathcal{G}^{(\mu)} \mathcal{B} \left(\frac{2}{D}\int w\vec{\Phi} dy + \frac{6}{D}\mathcal{V}\vec{\xi}\right), \tag{4.40}$$

where

$$\vec{\xi} \equiv \begin{pmatrix} \xi_1 \\ \vdots \\ \xi_N \end{pmatrix} \quad \text{and} \quad \mathcal{G}^{(\mu)} \equiv \begin{pmatrix} G^{(\mu)}_{1,1} & G^{(\mu)}_{1,2} & \cdots & G^{(\mu)}_{1,N} \\ G^{(\mu)}_{2,1} & \ddots & \cdots & G^{(\mu)}_{2,N} \\ \vdots & \vdots & \ddots & \vdots \\ G^{(\mu)}_{N,1} & G^{(\mu)}_{N,2} & \cdots & G^{(\mu)}_{N,N} \end{pmatrix}, \tag{4.41}$$

$\mathcal{B}$ and $\mathcal{V}$ are diagonal matrices with

$$\mathcal{B}_{j,j}=\begin{cases} 1, & j\text{th spike is } u_1\text{-type,} \\ \beta, & j\text{th spike is } u_2\text{-type,} \end{cases} \text{ and } \mathcal{V}_{j,j}=\begin{cases} \frac{1}{v_1^2}, & j\text{th spike is } u_1\text{-type,} \\ \frac{1}{v_2^2}, & j\text{th spike is } u_2\text{-type.} \end{cases} \tag{4.42}$$

Solving system (4.40) we get

$$\vec{\xi}=\frac{2}{D}\left(\mathcal{I}-\frac{6}{D}\mathcal{G}^{(\mu)}\mathcal{B}\mathcal{V}\right)^{-1}\mathcal{G}^{(\mu)}\mathcal{B}\int w\vec{\Phi}dy. \tag{4.43}$$

We label $\vec{\Phi}=\vec{m}\phi_0$ and plug (4.43) into (4.34); then we have

$$\vec{m}\lambda\phi_0=\vec{m}L_0\phi_0+M\vec{m}\frac{w^2\int w\phi_0}{\int w^2}, \tag{4.44}$$

where

$$M=\frac{2\int w^2}{D}\mathcal{V}\left(\mathcal{I}-\frac{6}{D}\mathcal{G}^{(\mu)}\mathcal{B}\mathcal{V}\right)^{-1}\mathcal{G}^{(\mu)}\mathcal{B}. \tag{4.45}$$

This yields

$$\lambda\phi_0=L_0\phi_0+\eta w^2\frac{\int w\phi_0}{\int w^2}, \tag{4.46}$$

where η is the eigenvalue of M given in (4.45).

Note that when $\beta=1$, u_1, u_2 are essentially the same so that $l_1=l_2=\frac{L}{N}$ and $v_1=v_2=\frac{3N}{aL}$. Then the matrix M in (4.45) becomes

$$M=\frac{2\int w^2}{Dv_1^2}\left(\mathcal{I}-\frac{6}{Dv_1^2}\mathcal{G}^{(\mu)}\right)^{-1}\mathcal{G}^{(\mu)}. \tag{4.47}$$

This recovers the results for the large eigenvalue in the two-component Schnackenberg model [28].

For our system with $\beta\neq 1$, since it's hard to compute the general results for eigenvalues of M given in (4.47), here we consider a special case where there is 1 u_1-type spike and 1 u_2-type spike. In this case we have

$$\begin{aligned} M&=\frac{2\int w^2}{D}\begin{pmatrix} \frac{1}{v_1^2} & 0 \\ 0 & \frac{1}{v_2^2} \end{pmatrix}\begin{pmatrix} 1-\frac{6}{Dv_1^2}G_{1,1}^{(\mu)} & -\frac{6\beta}{Dv_2^2}G_{1,2}^{(\mu)} \\ -\frac{6}{Dv_1^2}G_{2,1}^{(\mu)} & 1-\frac{6\beta}{Dv_2^2}G_{2,2}^{(\mu)} \end{pmatrix}^{-1}\begin{pmatrix} G_{1,1}^{(\mu)} & \beta G_{1,2}^{(\mu)} \\ G_{2,1}^{(\mu)} & \beta G_{2,2}^{(\mu)} \end{pmatrix} \\ &=C\begin{pmatrix} Dv_2^2G_{1,1}^{(\mu)}-6\beta\det(\mathcal{G}) & Dv_2^2\beta G_{1,2}^{(\mu)} \\ Dv_1^2G_{2,1}^{(\mu)} & Dv_1^2\beta G_{2,2}^{(\mu)}-6\beta\det(\mathcal{G}) \end{pmatrix}, \end{aligned} \tag{4.48}$$

where $\mathcal{G}=\begin{pmatrix} G_{1,1}^{(\mu)} & G_{1,2}^{(\mu)} \\ G_{2,1}^{(\mu)} & G_{2,2}^{(\mu)} \end{pmatrix}$ and $C=\frac{2\int w^2}{D^2v_1^2v_2^2-6\beta Dv_1^2G_{2,2}^{(\mu)}-6Dv_2^2G_{1,1}^{(\mu)}+36\beta\det(\mathcal{G})}$.

In the limit as $\tau \to 0$, we have $\mu \to 0$ and, after some algebra, matrix M can be simplified as

$$M = \frac{-2}{\beta D v_1^2 + D v_2^2 + 6\beta L} \begin{pmatrix} D v_2^2 + 6\beta L & \beta D v_2^2 \\ D v_1^2 & \beta D v_1^2 + 6\beta L \end{pmatrix}. \tag{4.49}$$

Computing the eigenvalues of M, we obtain that

$$\eta_1 = -2, \eta_2 = \frac{-12\beta L}{\beta D v_1^2 + D v_2^2 + 6\beta L}. \tag{4.50}$$

Let's recall the following lemma from [63]:

Lemma 4.2.1 *Consider the nonlocal eigenvalue problem*

$$\phi'' - \phi + 2w\phi - \alpha \frac{\int w\phi}{\int w^2} w^2 = \lambda\phi. \tag{4.51}$$

1) If $\alpha > 1$, then there exists a positive eigenvalue to (4.51);

2) If $\alpha < 1$, Then either $\lambda = 0$ with the eigenfunction $\phi = c_0 w'$ for some constant c_0 or

$$Re(\lambda) < 0.$$

From Lemma 4.2.1, we see that the critical threshold for the stability of the large eigenvalue is such that

$$-1 = \frac{-12\beta L}{\beta D v_1^2 + D v_2^2 + 6\beta L}. \tag{4.52}$$

Plugging $v_1 = \frac{3}{a l_1}, v_2 = \frac{3\beta}{a l_2}$, we get the critical threshold for the stability of the large eigenvalue (denoted as a_l)

$$a_l = \sqrt{\frac{3D}{2L}\left(\frac{1}{l_1^2} + \frac{\beta}{l_2^2}\right)}. \tag{4.53}$$

For more general case $N \geq 3$, the large eigenvalue threshold a_l corresponds to the value of a for which the largest eigenvalue of M equals -1. Table 4.3 shows the thresholds a_l for different orders of spikes in $(3,1)$ and $(3,2)$ spike patterns. Note that for different orders of spikes, a_l can be different, so in Table 4.3 we denote the ordering of u_1 and u_2 as s, l. Although there are $\binom{N}{k_2}$ different spike orderings for fixed k_1, k_2, the number of instability thresholds is less than $\binom{N}{k_2}$ since the threshold

a_l patterns / (k_1, k_2)	$(s\,s\,s\,l)$	$(s\,s\,l\,s)$	$(s\,l\,s\,s)$	$(l\,s\,s\,s)$
(3,1)	2.9898	2.7709	2.7709	2.9898

a_l patterns / (k_1, k_2)	$(s\,s\,s\,l\,l)$	$(s\,s\,l\,s\,l)$	$(s\,s\,l\,l\,s)$	$(s\,l\,s\,s\,l)$	$(s\,l\,s\,l\,s)$	$(l\,s\,s\,s\,l)$
(3,2)	4.7233	4.4944	4.4941	4.5941	4.1552	4.7656

Table 4.3: larger eigenvalue instability thresholds a_l in different spike orderings. The parameters are $L = 3, \beta = 0.5, D = 1$. Note that in the 2nd table we only show the spike orderings that have distinct thresholds.

is the same when the ordering is flipped (for example, see Table 4.3 where the large eigenvalue threshold is the same for $(s\,s\,s\,l)$ and $(l\,s\,s\,s)$).

It is well known that for two-component reaction diffusion systems the competition instability threshold in N-spike equilibria ($N \geq 2$) cross the threshold for small eigenvalues first [27, 28, 100]. And it appears to still be the case in the two-species vegetation system (4.2). We compare the instability thresholds a_l and a_s for arbitrary (k_1, k_2) patterns (except $(1, N-1)$ patterns when $\beta < 1$ and $(N-1, 1)$ patterns when $\beta > 1$) numerically; the results are shown in Figure 4.4, where we tried different β for $(2, 2)$ spike pattern and it is always the case $a_s > a_l$. As we increase β to 1, a_s overlaps with a_f, and a_l *does not exist* on the stable branch, which means the whole branch is stable for large eigenvalues. Similar results can be obtained for other patterns. See also Table 4.1 for more results of a comparison between a_l and a_s. We then conjecture that for arbitrary (k_1, k_2) patterns it is still the case that the competition instability threshold a_s crosses the threshold for small eigenvalues first.

Therefore we have the result that $a_s > a_l$ and N-spike equilibria are stable with respect to both large and small eigenvalues when $a > a_s$; when $a_l < a < a_s$, they are stable with respect to large eigenvalues but unstable with respect to small eigenvalues; when $a < a_l$, N-spike equilibria become unstable with respect to both large and small eigenvalues.

We now combine these results with those in Section 4.2.1. We have shown in Figure 4.3 that $a_s > a_f$ for $k_1 \geq 2$ ($\beta < 1$) or $k_2 \geq 2$ ($\beta > 1$) and $a_s < a_f$ for either

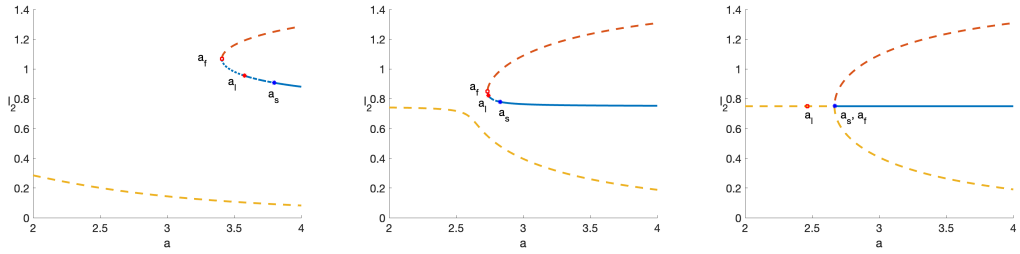

Figure 4.4: Radius of u_2 spike l_2 vs a for $(2,2)$ spike pattern. The instability thresholds on the stable branch are shown. Solid lines: linearly stable for both the small eigenvalues and the large eigenvalues; Dash-dotted lines: unstable for the small eigenvalues but stable for the large eigenvalues; Dotted line: unstable for both small eigenvalues and large eigenvalue. Here we choose $\beta = 0.5, 0.99, 0.9999$ from left to right; the other parameters are $D = 1, L = 3$.

$(1, N-1)$ spike patterns ($\beta < 1$) or $(N-1, 1)$ spike patterns ($\beta > 1$). For the former case, $a_f < a_l < a_s$, thus a_s is the dominant instability threshold; for the latter one, we found that a_l *does not exist* in the stable branch, thus $a_f > a_s$ is the dominant instability threshold.

Therefore, there are $N+1$ distinct instability thresholds denoted as a^* for each N, each corresponding to a different number of u_1 spikes (from zero to N). Moreover, we are curious about stability ordering within these patterns. We compared a^* for different $(k_1, N-k_1)$ patterns with fixed N. Table 4.1 illustrates the results for various patterns and this is further illustrated in Figure 4.2.

We now summarize the result as follows.

Result 4.2.1 *The N-spike steady state for system (4.2) which contains k_1 u_1-spikes and k_2 u_2-spikes becomes unstable when a decreases to $a^* = \max(a_f, a_s)$, where a_f is the largest real root of equation (4.21) and a_s is given in equation (4.32). Moreover, using (k_1, k_2) to represent different patterns regardless of the order of different spikes, where $k_1 = 0...N, k_2 = N - k_1$, the stability of the patterns has following order (from most stable to most unstable) depending on the ratio of water intake β:*

$$\beta < 1 : (0, N) > (N, 0) > (N-1, 1) > (N-2, 2) > ... > (1, N-1),$$

$$\beta > 1 : (N, 0) > (0, N) > (1, N-1) > (2, N-2) > ... > (N-1, 1).$$

Figure 4.5 shows stability regions for all possible combinations of 3-spike patterns. As a decrease below the critical line, the corresponding pattern becomes unstable.

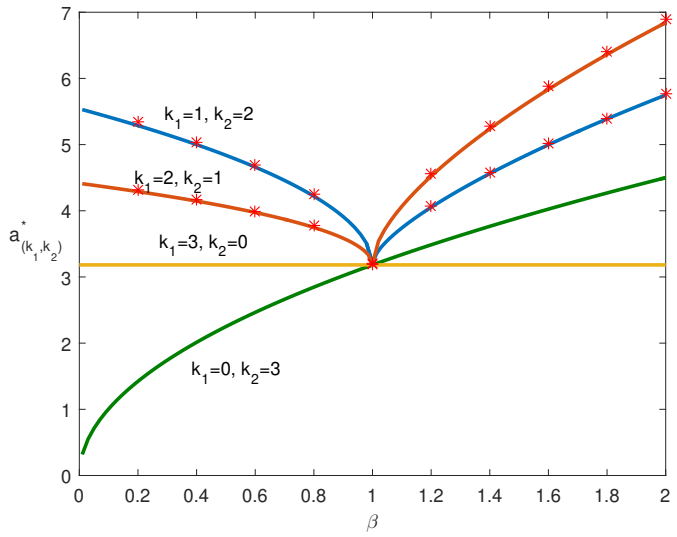

Figure 4.5: Instability regions for all possible combinations of 3-spike patterns. Below each line the corresponding (k_1, k_2) pattern becomes unstable and one u_1-type spike will get killed when $k_1 \geq 1$ or one u_2-type spike get killed when $k_1 = 1$. The red dots are numerical thresholds obtained from full simulations of system (4.2) by FlexPDE. We look for the numerical thresholds by gradually decreasing a until the pattern becomes unstable and one thirsty patch collapses. Here the parameters are: $L = 2, D = 1, \varepsilon = 0.03$.

The dots in Figure 4.5 are obtained by full simulations using FlexPDE which are in good agreement with our analytical results.

4.3 Discussion

In this chapter we have proposed a two-species model (corresponding to two different plants), with competition for a common resource (water). This model is based on the well-known Klausmeier model of vegetation patterns. For simplicity, we concentrated on two plant species which are identical in every aspect except for the rate of water consumption: thirsty and frugal plants. We have shown that in the water-constrained regime where spike patterns exist, the two species can co-exist. However as the precipitation rate decreases, the "frugal" plant is more robust and can out-compete the more "thirsty" plant, leading to the death of thirsty plants and survival of the more frugal plant.

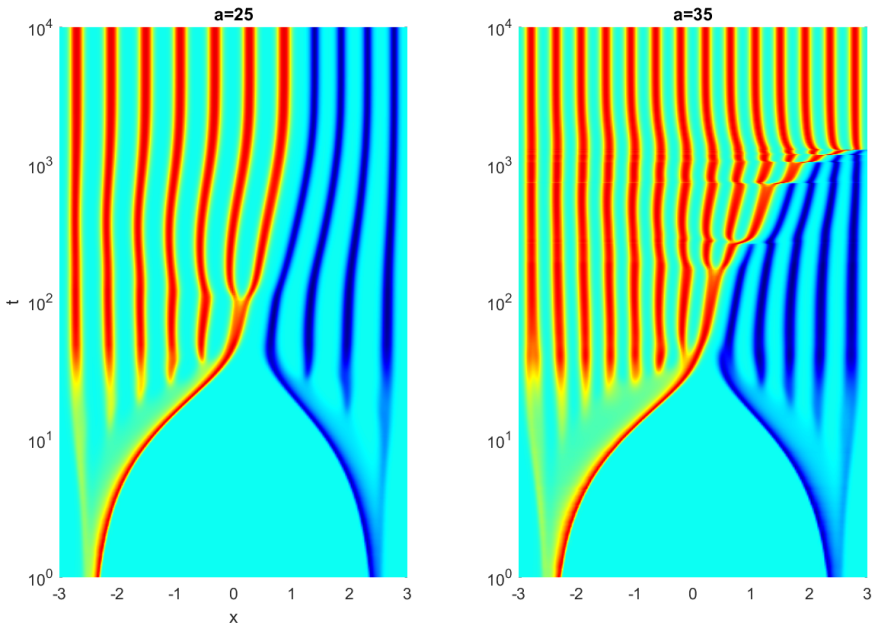

Figure 4.6: Space-time plot of u_1 (blue) and u_2 (red) as a function of time with a as indicated and with $\beta = 0.6, \varepsilon = 0.03, D = 1, L = 3$, with a as indicated. Initial conditions consist of two spots on the opposite sides of the domain. Left: self-replication of both types of plants, leading to co-existence. Right: self-replication is followed by a takeover of the entire domain by the red plant. Note that time is plotted on a log scale

We found two distinct mechanisms which triggered the dominant instability, depending on the number of spikes of each type. When only one spike of the thirsty plant is present (represented in blue in Figure 4.2), the dominant instability corresponds to a fold point a_f as derived in Section 4.1.1, and leads to the death of the blue spike when triggered. When more than one blue spikes exists, the dominant instability corresponds to asymmetric spike bifurcation at a_s as explained in Section 4.2.1. This leads to a competition instability among the blue spikes, with one of the blue spikes getting killed. In summary, no matter which mechanism triggers spike death, the blue spikes always get killed first until only red spikes remain. In either case, when $\beta = 1$ (so that the two species are indistinguishable), the instability thresholds correspond exactly to those derived for a symmetric $N-$spike configuration for the Schnakenberg model in [27, 28]. Note that in Section 4.2.1 the conclusion that the dominant instability corresponds to asymmetric spike bifurcation at a_s rather than

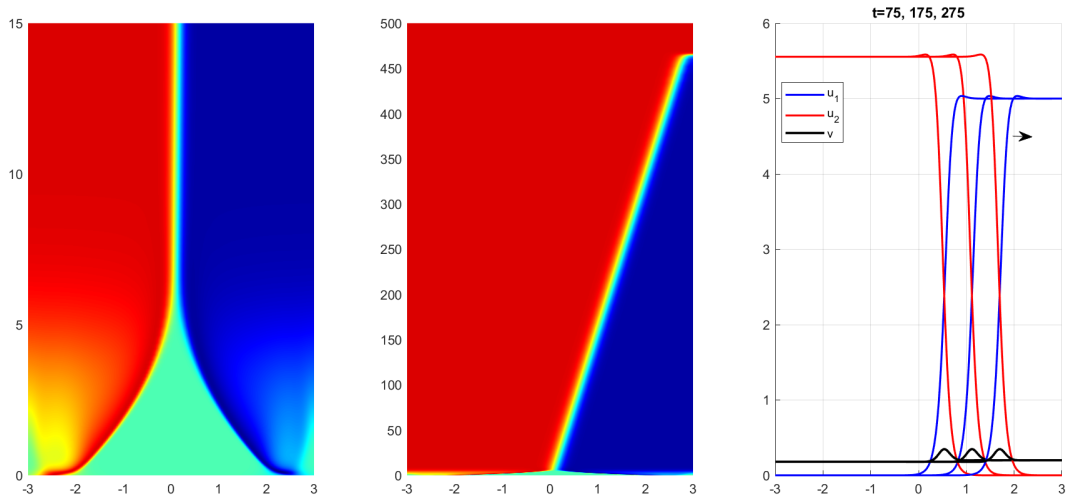

Figure 4.7: Space-time plot of u_1 (blue) and u_2 (red) as a function of time with $\varepsilon = 0.1, \beta = 0.9, a = 50$. Initial conditions consist of two spots on the opposite sides of the domain. Left: intial space-filling dynamics for $t \in (0, 15)$. Middle: takeover of the domain by the red plant, $t \in (0, 500)$. Right: snapshot of the propagating waves at three different times as indicated. The wave propagates with a constant speed.

large eigenvalue instability threshold a_l is a conjecture. An interesting open problem is to prove it analytically.

What happens as the precipitation rate is increased? For the Schnakenberg model, it is well-known that as a is increased, spot replication is observed [122, 6, 100]. A further increase of a eventually leads to a uniform-vegetation state. In the case of two species, self-replication is also observed for sufficiently large a; see Figure 4.6 (left). However, depending on the parameter values chosen, this can further lead to the more frugal plant species taking over the entire domain. This suggests that the co-existence of two plant species occurs only for precipitation parameter $a \in (a_{\text{coexistence,min}}, a_{\text{coexistence,max}})$. It is an open question to determine the upper boundary of this interval.

The behaviour of the system is very different for even larger a, as shown in Figure 4.7. In this case, the two plants self-organize into a propagating wave of vegetation. The red wave (corresponding to a more frugal plant) eventually takes over the entire domain. Similar phenomenon can be observed in other competition kinetics [123]. An open question is compute the propagation speed as a function of system parameters.

Chapter 5

Localized structure in the Schnakenberg model

In this chapter, we consider the following modified one-dimensional Schnakenburg model by taking $d_1 = \varepsilon^2, d_2 = 1$ in (1.10):

$$u_t = a - u + u^2 v + \varepsilon^2 \frac{\partial^2 u}{\partial x^2}, \quad x \in (-L, L), \tag{5.1a}$$

$$v_t = b - u^2 v + \frac{\partial^2 v}{\partial x^2}, \quad x \in (-L, L), \tag{5.1b}$$

subject to Neumman boundary conditions.

5.1 Semi-strong asymptotic construction of spike solutions.

We first construct the single-spike patterns in (5.1). Moreover, we are interested in the limit that $L \to \infty$, in which case we shall seek a solution of (5.1) that is a homoclinic orbit in space to the homogeneous equilibrium

$$u \to a + b, \qquad v \to \frac{b}{(a+b)^2}, \quad \text{as } x \to \pm\infty.$$

The semi-strong interaction method [124] is a form of matched asymptotic expansion which applies to the current problem when both parameters a and b are small. In particular, we find a natural distinguished limit by setting

$$a = \varepsilon\, \alpha, \qquad b = \varepsilon^2\, \beta, \qquad \text{where } \alpha \text{ and } \beta \text{ are } O(1), \tag{5.2}$$

to obtain

$$u_t = \varepsilon^2 \frac{\partial^2 u}{\partial x^2} + u^2 v - u + \varepsilon\alpha, \tag{5.3a}$$

$$v_t = \frac{\partial^2 v}{\partial x^2} - u^2 v + \varepsilon^2 \beta. \tag{5.3b}$$

We then seek solutions expanded in powers of ε

$$u(x) = u_0 + \varepsilon u_1 + O(\varepsilon^2), \qquad v(x) = v_0 + \varepsilon v_1 + O(\varepsilon^2),$$

in the inner and outer asymptotic regimes, separately.

To find the steady state of system (5.1), we first look at inner region and introduce inner variable $y = \frac{x}{\varepsilon}$; then to leading order, the system becomes:

$$\begin{aligned} u_{yy} - u + u^2 v = 0, \\ v_{yy} = 0\,. \end{aligned} \tag{5.4}$$

Solving system (5.4), we have

$$u = \frac{w(y)}{v_0}, v = v(0) = v_0\,, \tag{5.5}$$

where $w(y)$ satisfies $w'' - w + w^2 = 0$ and $w(y) = \frac{3}{2}\operatorname{sech}^2(\frac{y}{2})$.

We then look at the outer region; to leading order we have

$$u \sim \varepsilon\alpha\,. \tag{5.6}$$

By doing change of variable $z = \varepsilon x$ and plugging (5.6) into the $v-$equation, we have that v satisfies

$$\begin{cases} v_{zz} - \alpha^2 v + \beta = \dfrac{6}{v_0}\delta(z), \\ v_z(0_+) - v_z(0_-) = \dfrac{6}{v_0}, \\ v_z(\pm\varepsilon L) = 0\,, \end{cases} \tag{5.7}$$

where we have used the fact that $\int_{0_-}^{0_+} u^2 v dz = \frac{6}{v_0}$.

To solve system (5.7), we introduce the Green's function $G(z)$ which satisfies

$$\begin{cases} G_{zz} - \mu^2 G = \delta(z), \\ G_z(\pm\varepsilon L) = 0\,. \end{cases} \tag{5.8}$$

A simple calculation gives

$$G(z;\mu) = -\frac{1}{2\mu\sinh(\mu\varepsilon L)}\cosh(\mu(|z| - \varepsilon L)). \tag{5.9}$$

The solution to (5.7) is then given by

$$\begin{aligned} v(z) &= \frac{6}{v_0}G(z;\alpha) + \frac{\beta}{\alpha^2}, \\ &= -\frac{3}{\alpha v_0\sinh(\alpha\varepsilon L)}\cosh(\alpha(|z| - \varepsilon L)) + \frac{\beta}{\alpha^2}, \end{aligned} \tag{5.10}$$

where v_0 is to be determined.

To determine v_0 we take $z = 0$ to obtain the following quadratic equation

$$v_0^2 - \frac{\beta}{\alpha^2} v_0 + \frac{3}{\alpha \tanh(\alpha\varepsilon L)} = 0, \tag{5.11}$$

so that

$$v_{0\pm} = \frac{\beta}{2\alpha^2} \pm \sqrt{\frac{\beta^2}{4\alpha^4} - \frac{3}{\alpha \tanh(\alpha\varepsilon L)}}. \tag{5.12}$$

Fold bifurcation occurs when

$$\tanh(\varepsilon\alpha L)\beta^2 = 12\alpha^3 \tag{5.13}$$

with $v_0^* = \frac{\beta}{2\alpha^2} = \sqrt{\frac{3}{\alpha \tanh(\varepsilon\alpha L)}}$.

Note that when $L \to \infty$, $\tanh(\varepsilon\alpha L) \sim 1$, which yields the fold point $\beta^2 = 12\alpha^3$. Moreover, as we take $L \to \infty$, v_0, expressed in (5.10), simplifies to the following exponential function:

$$v(z) = -\frac{3}{\alpha v_0} e^{-\alpha|z|} + \frac{\beta}{\alpha^2}. \tag{5.14}$$

We now summarize our result as follows:

Result 5.1.1 *With $0 < \varepsilon \ll 1$, the modified Schnackenberg system (5.1) has the following single-spike steady state:*

$$\begin{aligned} u(x) &= \frac{1}{v_0} w\left(\frac{x}{\varepsilon}\right) + \varepsilon\alpha, \\ v(x) &= -\frac{3}{\alpha v_0 \sinh(\alpha\varepsilon L)} \cosh(\alpha\varepsilon(|x| - L)) + \frac{\beta}{\alpha^2}, \end{aligned} \tag{5.15}$$

where $w(y) = \frac{3}{2}\operatorname{sech}^2(\frac{y}{2})$ and v_0 is a constant given in (5.12). There is a fold point when $\tanh(\varepsilon\alpha L)\beta^2 = 12\alpha^3$, which corresponds to the double roots of (5.11).

Moreover, in the limit $L \to \infty$, the equilibrium $v(x)$ simplifies to

$$v(x) = -\frac{3}{\alpha v_0} e^{-\alpha\varepsilon|x|} + \frac{\beta}{\alpha^2}, \tag{5.16}$$

and the fold bifurcation criteria simplifies to $\beta^2 = 12\alpha^3$.

5.2 Stability Analysis

In this section we consider linear stability of a spike. Our analysis is closely related to [66, 63] and uses the results on the related Non-local Eigenvalue Problem (NLEP) therein.

We start by considering a more general case where the timescales of the two fields are different. Specifically, let us assume that a time scaling parameter τ multiplies v_t, so that system (5.1) becomes

$$u_t = \varepsilon^2 u_{xx} - u + u^2 v + \varepsilon\alpha, \tau v_t = v_{xx} - u^2 v + \varepsilon^2\beta\,. \tag{5.17}$$

It will be convenient to consider τ at first to be small, and then continue up to the case $\tau = 1$, which leads to (5.1).

5.2.1 A non-local eigenvalue problem

We first linearize around the steady state by taking

$$\begin{aligned} u(x,t) &= u_0(x) + \phi(x)\exp(\lambda t), \\ v(x,t) &= v_0(x) + \psi(x)\exp(\lambda t)\,, \end{aligned}$$

where we assume $|\phi|, |\psi| \ll 1$. Then we obtain the linearized problem

$$\begin{aligned} \lambda\phi &= \varepsilon^2\phi_{xx} + (2u_0v_0 - 1)\phi + u_0^2\psi, \\ \tau\lambda\psi &= \psi_{xx} - 2u_0v_0\phi - u_0^2\psi\,. \end{aligned}$$

In the inner region, we let $y = \frac{x}{\varepsilon}$; then, to leading order, we obtain $\psi_{yy} = 0$ so that $\psi \sim \psi_0$ is a constant which needs to be determined. The equation for ϕ then becomes

$$\lambda\phi = \phi_{yy} + 2w\phi - \phi + \frac{w^2}{\kappa^2}\psi_0. \tag{5.18}$$

In the outer region, we approximate

$$\psi_{xx} - \tau\lambda\psi - \varepsilon^2\alpha^2\psi = c\delta(x;0), \tag{5.19}$$

where

$$\begin{aligned} c &= 2\int_{0-}^{0+} u_0v_0\phi dx + \int_{0-}^{0+} u_0^2\psi dx \\ &\sim 2\varepsilon\int_{-\infty}^{\infty}\phi w dy + \frac{6\varepsilon}{\kappa^2}\psi_0\,, \text{as } \varepsilon \to 0 \end{aligned}$$

in which we have used the fact that $\int_{-\infty}^{\infty} w^2 dy = 6$. The solution to (5.19) can be written as

$$\psi = cG(x;\mu), \mu = \sqrt{\tau\lambda + \varepsilon^2\alpha^2}$$

where $G(x;\mu)$ is the Green's function which satisfies

$$\begin{cases} G_{xx} - \mu^2 G = \delta(x;0), \\ \quad G_x(\pm l) = 0\,, \end{cases}$$

and

$$G(x;\mu) = -\frac{1}{2\mu\sinh(\mu l)}\cosh(\mu(|x| - l)).$$

Therefore the solution to (5.19) is

$$\psi(x) = -\frac{c}{2\sqrt{\tau\lambda + \varepsilon^2\alpha^2}\sinh(\sqrt{\tau\lambda + \epsilon^2\alpha^2}l)}\cosh(\sqrt{\tau\lambda + \varepsilon^2\alpha^2}(|x| - l)),$$

and we solve ψ_0 by letting

$$\psi_0 = \psi(0) = -\frac{\epsilon\int \phi w dy + \frac{3\varepsilon}{\kappa^2}\psi_0}{\sqrt{\tau\lambda + \varepsilon^2\alpha^2}\tanh(\sqrt{\tau\lambda + \varepsilon^2\alpha^2}l)}$$

so that

$$\psi_0 = -\frac{\varepsilon\int \phi w dy}{\frac{3\varepsilon}{\kappa^2} + \sqrt{\tau\lambda + \varepsilon^2\alpha^2}\tanh(\sqrt{\tau\lambda + \varepsilon^2\alpha^2}l)}. \tag{5.20}$$

Substituting (5.20) into (5.18) yields the following non-local eigenvalue problem (NLEP)

$$\lambda\phi = L_0\phi - w^2\frac{\int \phi w dy}{A}, \tag{5.21}$$

where $L_0\phi = \phi_{yy} - \phi + 2w\phi$ and

$$A = 3 + \sqrt{\frac{\tau\lambda}{\varepsilon^2} + \alpha^2}\tanh(\sqrt{\tau\lambda + \varepsilon^2\alpha^2}l)\kappa^2. \tag{5.22}$$

To analyse stability, we consider the following two cases, $\tau = 0$ and $\tau \neq 0$.

5.2.2 The case $\tau = 0$

When taking $\tau = 0$, A in (5.22) simplifies to

$$A = 3 + \alpha\tanh(\varepsilon\alpha l)v_0^2; \tag{5.23}$$

then equation (5.21) reduces to a well-known NLEP which was first studied in [63]; in particular, we have the following basic result:

Theorem 5.2.1 *(See [63]) Consider the problem (5.21); we have* $Re(\lambda) < 0$ *if* $A < 6$, $Re(\lambda) > 0$ *if* $A > 6$, *and* $\lambda = 0$ *with* $\phi = w$ *if* $A = 6$.

To determine the stability of the two branches corresponding to the values v_{0-} and v_{0+} shown in (5.12), we substitute $v_{0\pm}$ into (5.23) to obtain

$$A(v_{0\pm}) = \frac{\beta^2 \tanh(\varepsilon\alpha l)}{2\alpha^3} \pm \frac{\beta\sqrt{\tanh(\varepsilon\alpha l)}}{2\alpha^{\frac{3}{2}}}\sqrt{\frac{\beta^2 \tanh(\varepsilon\alpha l)}{\alpha^3} - 12}. \tag{5.24}$$

Since the existence of a solution for v_{0+} requires $\frac{\beta^2\tanh(\varepsilon\alpha l)}{\alpha^3} > 12$, it is easy to see that $A(v_{0+}) > 6$, so by Theorem 5.2.1 the solution corresponding to v_{0+} is unstable. For the other branch, corresponding to v_{0-}, we take $\frac{\beta^2\tanh(\varepsilon\alpha l)}{\alpha^3} = 12 + \delta$, where $\delta > 0$, then we have

$$A(v_{0-}) = 6 - \frac{\sqrt{12\delta + \delta^2} - \delta}{2} < 6.$$

Therefore, the solution corresponding to v_{0-} is stable. Moreover, at the fold point where $\frac{\beta^2\tanh(\varepsilon\alpha l)}{\alpha^3} = 12$, we can easily get from (5.24) that $A = 6$, which corresponds to $\lambda = 0$. We summarize our result as follows.

Proposition 5.2.1 *In the case* $\tau = 0$, *the one-spike solution* $u(x), v(x)$ *given in (5.5), (5.10) with* $v(0) = v_{0+}$ *is unstable and the other branch* $v(0) = v_{0-}$ *is always stable. The two roots* $v_{0\pm}$ *connect at a fold point corresponding to a double root of (5.11).*

5.2.3 The case $\tau \neq 0$

We now study the case where A depends on λ. To study the stability of the lower branch v_{0+}, we first rewrite equation (5.21) in the following form

$$(L_0 - \lambda)\phi = w^2, \qquad \text{where} \quad \int \phi w \, dy = A(\lambda)\,,$$

or

$$\int w(L_0 - \lambda)^{-1} w^2 \, dy = A(\lambda). \tag{5.25}$$

(Above, we use the fact that ϕ is only defined up to a multiplicative constant and we scale ϕ so that $\int \phi w = A$).

We denote the left-hand side of equation (5.25) as $f(\lambda)$. The global behaviour of precisely this same $f(\lambda)$ was studied in [66], from which we obtain the following basic results:

Theorem 5.2.2 *(See [66]) $f(\lambda)$ has the behavior*

$$f(0) = 6, f'(\lambda) > 0, f''(\lambda) > 0, \lambda \in (0, \frac{5}{4}).$$

Moreover, $f(\lambda)$ has a singularity at $\lambda = \frac{5}{4}$ with $f(\lambda) \to \pm\infty$ as $\lambda \to \frac{5}{4}_{\pm}$. For $\lambda > \frac{5}{4}$, we have $f(\lambda) < 0$ and $f(\lambda) \to 0$ as $\lambda \to \infty$.

The graph of $f(\lambda)$ is shown in Figure 5.1(a). From the right-hand side of equation (5.25), we have that $A(\lambda)$ is continuous and from the previous subsection, we have that $A(0) > 6$. Therefore the two functions $f(\lambda)$ and $A(\lambda)$ must intersect in the domain $\lambda > 0$, so that equation (5.25) must have a positive eigenvalue, which shows that the lower branch with $v(0) = v_{0+}$ is unstable.

We now study the stability of the upper branch, with $v(0) = v_{0-}$. Since we are interested in large domain $L \to \infty$, we let $\tanh(\varepsilon\alpha L) \sim 1$; then we rewrite A as follows by introducing $\hat{\tau} = \frac{\tau k^4}{\varepsilon^2}$, and $\gamma = \alpha^2 k^4$, to obtain

$$A \sim 3 + \sqrt{\hat{\tau}\lambda + \gamma}.$$

When $\hat{\tau}$ is sufficiently large, the system can be destabilized via a Hopf bifurcation. This was first proved in [66], from which we have the following result:

Theorem 5.2.3 *(See [66]) In the case $\hat{\tau} > 0$, the one-spike solution $u(x), v(x)$ given in (5.5), (5.10) with $v(0) = v_{0+}$ is always unstable and $v(0) = v_{0-}$ is stable only when $0 < \hat{\tau} < \hat{\tau}_h$ for some $\hat{\tau}_h > 0$. As $\hat{\tau}$ increases past $\hat{\tau}_h$, a Hopf bifurcation in the amplitudes of the spikes is triggered.*

Although we know of no explicit formula for the threshold $\hat{\tau}_h$ at which the Hopf bifurcation occurs, we can compute $\hat{\tau}_h$ numerically in matlab. We discretized the NLEP (5.21) using an implicit finite difference method. This results in a matrix eigenvalue problem $M\vec{\phi} = \lambda\vec{\phi}$. Here $\vec{\phi}$ is an n by 1 column vector corresponding to the discretization of the eigenfunction $\phi(x)$, where n is the number of mesh points, and M is an n by n matrix corresponding to the discretization of the linear operator in (5.21). When $\hat{\tau} = 0$, this is a straight forward matrix eigenvalue problem whose eigenvalues we computed using matlab's `eig` command. However when $\hat{\tau} \neq 0$, the coefficients in M also depend on λ: $M = M(\lambda)$. In this case, we used an iterative approach: starting with some λ_0, we solve $M(\lambda_0)\phi = \lambda_1\phi$ for λ_1; then $M(\lambda_1)\phi = \lambda_2\phi$ for λ_2 etc, with $\lambda_i \to \lambda$ as $i \to \infty$.

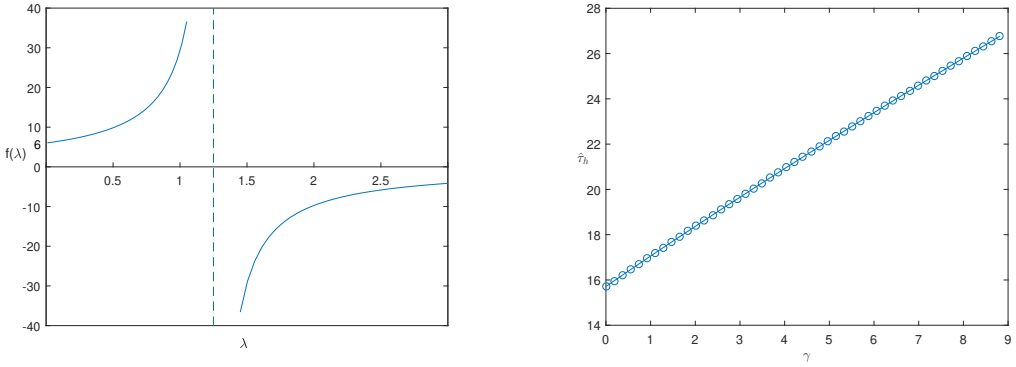

(a) (b)

Figure 5.1: Computational results illustrating the stability analysis; see text for details. (a) The function $f(\lambda)$ given in left-hand side of (5.25). (b) Hopf bifurcation points $\hat{\tau}_h$ against γ.

For a fixed γ, we used the above method to compute $\hat{\tau}_h$ such that $Re(\lambda) = 0$. The result is shown in Figure 5.1(b), which shows the Hopf bifurcation point $\hat{\tau}_h$ for $\gamma \in (0, 9)$.

5.2.4 The case $\tau = 1$

We now mainly consider system (5.17) with $\tau = 1$, which yields

$$\hat{\tau} = \frac{v_0^4}{\varepsilon^2}, \tag{5.26}$$

In particular, we consider the regime $\beta \gg 1$ (independent of ε) and $\alpha \sim O(1)$; then, to leading order, we have from (5.12) that

$$v_{0-} \sim \frac{3\,(\alpha + \varepsilon\beta)}{\beta} + \frac{9\,(\alpha + \varepsilon\beta)^4}{\beta^3} + O\left(\frac{1}{\beta^5}\right) \approx \frac{3\alpha + \varepsilon\beta}{\beta}. \tag{5.27}$$

Therefore $v_{0-}^4 \ll 1$ and $\gamma = \alpha^2 v_{0-}^4 \sim 0$, in which case $\hat{\tau}_h \sim 15.7$. From (5.26), we obtain the critical bifurcation value for α:

$$\alpha_h \sim \frac{\epsilon^{\frac{1}{2}} \hat{\tau}_h^{\frac{1}{4}} \beta}{3} = \frac{15.7^{\frac{1}{4}} \varepsilon^{\frac{1}{2}} \beta}{3} - \varepsilon\beta \sim (0.6636\varepsilon^{\frac{1}{2}} - \varepsilon)\beta. \tag{5.28}$$

We summarize our results as follows.

Result 5.2.1 *In the case $\tau = 1$, the one-spike solution $u(x), v(x)$ given in (5.5), (5.10) with $v(0) = v_{0-}$ is stable only when $0 < \alpha < \alpha_h$. As α increases past α_h,*

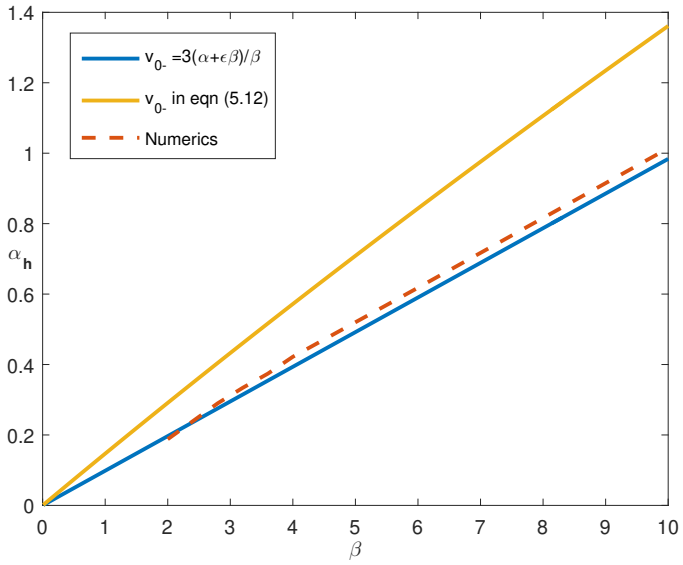

Figure 5.2: Hopf bifurcation threshold (Result 5.2.1). The parameters are $\varepsilon = 0.05, L = 100$. Here the dashed line is obtained through full simulations of system (5.3) by FlexPDE; we look for the numerical threshold by gradually increasing α until Hopf bifurcation is observed; different colored solid line is obtained by plugging asymptotic value (5.27) or exact value of v_{0-} (5.12) into (5.26) and computing α_h such that $\hat{\tau} = \hat{\tau}_h \sim 15.7$.

a Hopf bifurcation in the amplitude of the spikes is triggered. In particular, in the regime of large β, we have

$$\alpha_h \sim (0.6636\varepsilon^{\frac{1}{2}} - \varepsilon)\beta.$$

To verify this proposition, we can compare with numerical computation of the spectrum using a finite difference method. The result is shown in Figure 5.2, which shows good agreement when we take various different approximations to v_{0-} that are accurate to $O(\varepsilon)$.

5.3 Discussion

In this chapter, we studied the existence and stability of single-spike patterns in a modified Schnackenberg model, in which the inhibitor source $a = O(\varepsilon)$ and substrate source $b = O(\varepsilon^2)$. One of the key results presented here, compared with other papers that use semi-strong asymptotic theory, is the construction of spike patterns on the unbounded domain. We have shown how the exponentially localized solutions found

by taking an infinite domain, naturally transition to the solutions that are delocalized in the v-field.

An additional feature we found is the presence of a Hopf bifurcation in the limit that the source parameters a and b are sufficiently small. The presence of this instability was argued using an extension to a previously-analysed NLEP. For the particular model studied though, this instability was found numerically to not penetrate into parameter regions with large a and b. Preliminary calculations suggest that further asymptotic explanation of this disappearance of the Hopf bifurcation might be possible, by taking a slightly different distinguished limit.

Let us describe the difference between the "extended" Schankenberg model (5.3) and what we shall call the "classical" Schankenberg model, which is obtained by setting the feed-rate of the activator u to zero: $a = 0$ in (5.3) (see [124]). There are several key differences here: first, the introduction of the non-zero activator feed-rate allows for a spike solution which exists on an unbounded domain $x \in \mathbb{R}$. For the classical Schankenberg model, that is not the case: a single spike cannot be constructed on an unbounded domain (note however that a single spike on the entire domain is possible for the Gray-Scott model which also has a decay term in v). Moreover the outer region for u no longer decays to zero, and instead leads to a nonlinear outer problem.

Just like many other reaction-diffusion diffusion models such as the desertification model [120] or the "classical" Schankenberg model [124, 28], the extended Schankenberg model exhibits spike self-replication when b is increased. In addition, it has an entirely new mechanism leading to birth of new spikes – as illustrated in Figure 5.4 – that occurs for higher values of a: we call this "spike insertion" whereby additional spikes appear from the "background", away from other spikes. Contrast this with spike replication, where a spike splits into two. Numerics suggest that spike insertion is more prevalent for smaller values of a and when there are fewer spikes already present, and in general spike replication can follow spike insertion as b is increased further. Unlike spike replication, spike insertion is specific to the extended Schnakenberg model and does not appear in the classical Schnakenberg model nor in the Gray-Scott model.

The analysis in § 5.2 uses linear stability and NLEP theory to characterize the Hopf

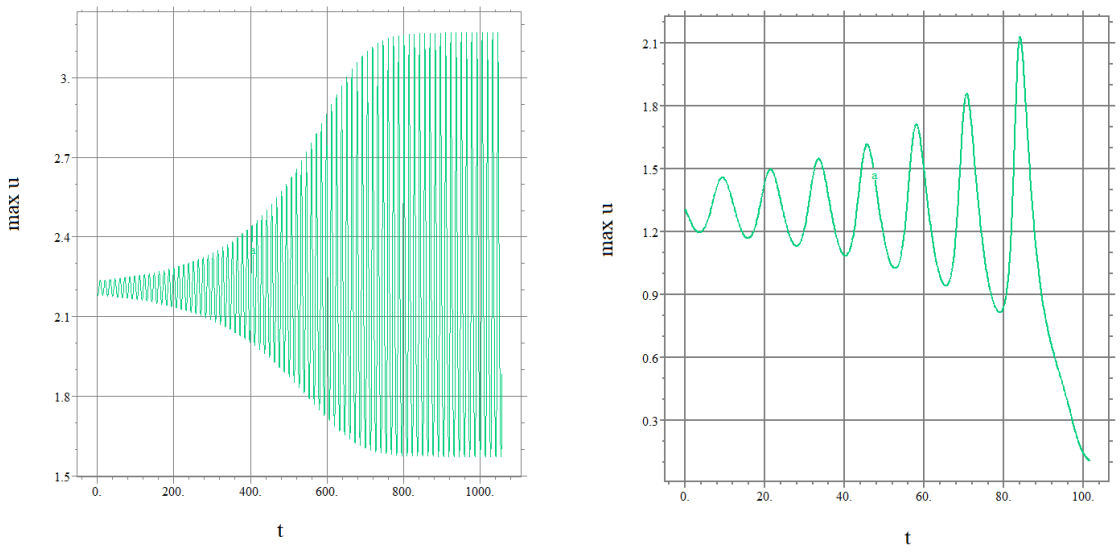

Figure 5.3: Spike oscillations above the Hopf bifurcations. Left: $\alpha = 1.2,\ \beta = 8,\ \varepsilon = 0.05,\ L = 30$ and $\tau = 0.255$. Supercritical bifurcation is observed leading to stable periodic oscillations Right: same parameter values as on the left, except that $L = 10$ and $\tau = 0.035$. the simulation shown in right figure suggests subcritical nature of the Hopf bifurcation, eventually resulting in spike death.

bifurcation leading to oscillations in spike height. However linear analysis does not describe what happens to a spike when it becomes unstable due to a Hopf bifurcation. For this, we use numerical experiments (via FlexPDE) to investigate the fate of the spike as the Hopf threshold is crossed. Numerics indicate that both subcritical as well as supercritical bifurcations are possible depending on parameter choice. This is illustrated in Figure 5.3.

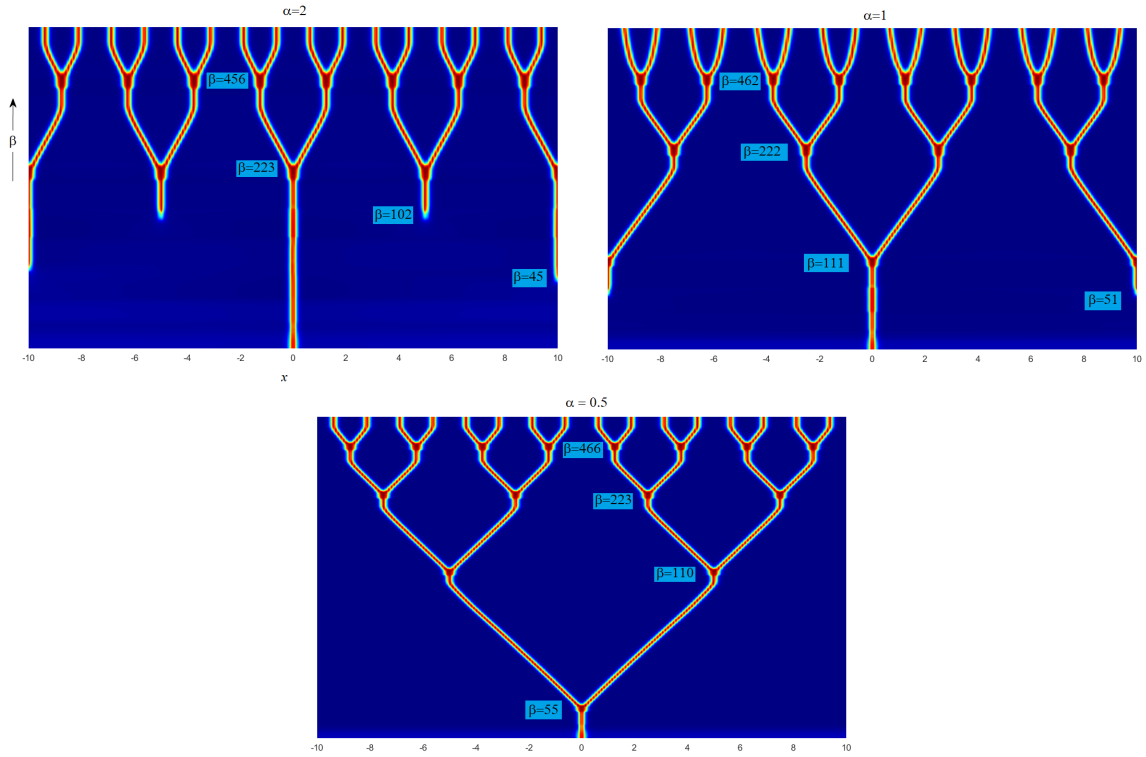

Figure 5.4: Spike insertion versus spike splitting. Full numerical simulations of (5.3) with $\varepsilon = 0.05, L = 10$ and with b gradually increased according to the formula $\beta = 20 + 0.001 * t$, for several values of α as indicated in the subpanels, where $a = \varepsilon\alpha, b = \varepsilon^2\beta$. $\alpha = 2$: two insertion events followed by self-replication events. $\alpha = 1$: one insertion event. $\alpha = 0.5$: no insertion events. Generally, for larger values of α several spike-insertion events can occur when β is relatively small, followed by self-replication events as β is further increased. For smaller values of α, only self-replication occurs as β is increased.

Chapter 6

Conclusions and future plans

In this thesis, we have studied four reaction-diffusion models and presented results on the dynamics and instabilities of one-dimensional spike patterns in these systems. We have applied asymptotic analysis combined with numerical methods to validate our results.

In the SIRS epidemic model with spatial diffusion and nonlinear incidence rates considered, we have shown that for small diffusion rate of the infected class D_I, the infected population tends to be highly localized at certain points inside the domain, forming K spikes. We then have studied three distinct instabilities, as well as a transition from localized spikes to plateau solutions under two regimes. When $D_R \gg O(\varepsilon^2)$, the K-spike patterns can undergo two types of instabilities, which are due to coarsening (spike death) and self-replication (spike birth), and have well-known analogues in other reaction-diffusion systems such as the Schnakenberg model. In the other regime where $D_R \leq O(\varepsilon^2)$, we have studied the instability where a single spike becomes unstable and moves to the boundary. We also show that a spike solution can transition into a plateau-type solution when the diffusion rates of recovered and susceptible class are sufficiently small.

An open problem here is to compute plateau-type steady states with nonzero D_R. We have studied plateau-type steady states in § 2.4.3 and this equilibrium solution can be thought of as "quarantine effect": when mobility of the recovered population and the susceptible population is reduced, the infected population is confined to a certain region of the entire domain with a sharp interface in between. For simplicity, We took the diffusion rate of the recovered class $D_R = 0$ when analyzing mesa-patterns. However, numerical simulations indicate that similar interface solutions persist for $0 < D_R \leq \varepsilon^2$. Construction of mesa-patterns and the transition between them and spike-patterns are to be studied in this regime for nonzero but sufficiently small D_R.

In contrast to the well-studied 1D problem, there have been far fewer studies

of the existence, linear stability, and dynamics of localized patterns for reaction-diffusion systems in 2D spaces. So another interesting open problem is to consider this SIRS model in a two-dimensional spatial domain, where localized spot patterns undergo either self-replication or competition or oscillatory instabilities depending on the parameter regime. The methodology is to use a hybrid asymptotic-numerical approach based on ideas from strong localized perturbation theory.

For the classical Gierer-Meinhardt model, we have studied in detail in chapter 3 the effect of noise on dynamics of a single spike on a finite interval. When spatio-temporal noise is introduced in the equation for the activator, we derived a stochastic ODE that describes the motion of a single spike on a slow time-scale. The steady state was described by a density distribution for spike positions, obtained via the corresponding Fokker-Plank PDE. For sufficiently small noise level, the spike performs random fluctuations near the centre of the domain. As the noise level is increased, the spike can deviate from the domain center but remains effectively "trapped" within a certain subinterval that includes the center. For even larger noise levels, the spike starts to undergo large excursions that eventually collide with the domain boundary and temporarily trap the spike there. By reformulating this problem in terms of mean first passage time (MFPT), we derive the expected time for the spike to collide with the boundary.

Note that we mainly studied the effect of **multiplicative noise** on the dynamics of single spike, where the spatial-temporal noise is multiplied by u. This type of noise assures that the randomness affects only the spike itself and has no effect outside the spike, since u decays exponentially away from spike center. An open problem we would like to study in the future is to study the effect of **additive noise**, where the noise is not multiplied by u but rather added to the whole background domain. From the numerical experiments, we observe that the additive noise can affect not only the spike motion but also spike stability as well, which leads to many new phenomena observed, including spike death, spike insertion, and *switching* behaviour. Simulation shows that spike insertion occurs when the height of inhibitor v exceeds activator u; we can reformulate this problem in terms of MFPT and compute the expected time for a new spike to generate. As for the spike death problem, we think this happens as the corresponding non-local eigenvalue problem becomes unstable. In this case the

non-local eigenvalue problem may contain noise term, which is a new problem and hasn't been studied much.

One more open problem in the Gierer-Meinhardt model is that when a spike hits the boundary, it gets "stuck" there. However, it can also get "unglued" from the boundary after a while. While we used MFPT theory to predict how long it takes for the spike to "hit" the boundary, we cannot explain why it gets "unglued" or how long it takes for the spike to unglue. These are all very interesting and doable problems for future work.

For the two-species vegetation model we have shown that in the water-constrained regime where spike patterns exist, the two species can co-exist. However, as the precipitation rate decreases, the "frugal" plant is more robust and can out-compete the more "thirsty" plant, leading to the death of thirsty plants and survival of the more frugal plants. We found two distinct mechanisms which triggered the dominant instability, depending on the number of spikes of each type. When only one spike of the thirsty plant is present (represented in blue in Figure 4.2), the dominant instability corresponds to a fold point a_f as derived in § 4.1.1, and leads to the death of the blue spike when triggered. When more than one blue spike exists, the dominant instability corresponds to asymmetric spike bifurcation at a_s as explained in § 4.2.1. This leads to a competition instability among the blue spikes, with one of the blue spikes getting killed. In summary, no matter which mechanism triggers spike death, the blue spikes always get killed first until only red spikes remain.

Simulations show that as a increases, self-replication can occur as precipitation rate is increased. A further increase of a eventually leads to a uniform-vegetation state. However, depending on parameters, this can further lead to the more frugal plant species taking over the entire domain. This suggests that the co-existence of two plant species occurs only for precipitation parameter $a \in (a_{\text{coexistence,min}}, a_{\text{coexistence,max}})$. It is an open question to determine the upper boundary of this interval.

For the modified Schnackenberg model with non-zero activator feed-rate, we have presented existence and stability of single-spike patterns on a bounded and unbounded domain. As discussed in § 5.3, an open problem is that this modified Schnackenberg model has an entirely new mechanism leading to birth of new spikes by "spike insertion" rather than by "self-replication" only. This phenomenon happens for larger

values of α and when β is relatively small. For smaller values of α, only self-replication occurs as β is increased.

Bibliography

[1] William O. Kermack and Anderson G. McKendrick. Contributions to the mathematical theory of epidemics—I. *Bulletin of Mathematical Biology*, 53(1-2):33–55, 1991.

[2] Alfred Gierer and Hans Meinhardt. A theory of biological pattern formation. *Kybernetik*, 12(1):30–39, 1972.

[3] David Iron, Michael J. Ward, and Juncheng Wei. The stability of spike solutions to the one-dimensional Gierer–Meinhardt model. *Physica D: Nonlinear Phenomena*, 150(1):25–62, 2001.

[4] Juncheng Wei and Matthias Winter. *Mathematical aspects of pattern formation in biological systems*. Springer, 2013.

[5] Christopher A. Klausmeier. Regular and irregular patterns in semiarid vegetation. *Science*, 284(5421):1826–1828, 1999.

[6] Yuxin Chen, Theodore Kolokolnikov, Justin Tzou, and Chunyi Gai. Patterned vegetation, tipping points, and the rate of climate change. *European Journal of Applied Mathematics*, 26(6):945–958, 2015.

[7] Olivier Lejeune, Mustapha Tlidi, and Pierre Couteron. Localized vegetation patches: a self-organized response to resource scarcity. *Physical Review E*, 66(1):010901, 2002.

[8] Ricardo Martínez-García, Justin M. Calabrese, Emilio Hernández-García, and Cristóbal López. Vegetation pattern formation in semiarid systems without facilitative mechanisms. *Geophysical Research Letters*, 40(23):6143–6147, 2013.

[9] F. Borgogno, P. D'Odorico, F. Laio, and L. Ridolfi. Mathematical models of vegetation pattern formation in ecohydrology. *Reviews of Geophysics*, 47(1), 2009.

[10] J. Schnakenberg. Simple chemical reaction systems with limit cycle behaviour. *Journal of Theoretical Biology*, 81(3):389–400, 1979.

[11] A. M. Turing. The chemical basis of mokphogenesis. *Philosophical Transactions of the Royal Society of London. Series B, Biological Sciences*, 237(641):37–72, 1952.

[12] Lee A. Segel and Julius L. Jackson. Dissipative structure: an explanation and an ecological example. *Journal of Theoretical Biology*, 37(3):545–559, 1972.

[13] Hans Meinhardt and Alfred Gierer. Pattern formation by local self-activation and lateral inhibition. *Bioessays*, 22(8):753–760, 2000.

[14] Hans Meinhardt. Models of biological pattern formation: from elementary steps to the organization of embryonic axes. *Current Topics in Developmental Biology*, 81:1–63, 2008.

[15] Niky Kamran and Yasumasa Nishiura. *Far-from-equilibrium Dynamics*, volume 209. American Mathematical Soc., 2002.

[16] Izumi Takagi. Point-condensation for a reaction-diffusion system. *Journal of Differential Equations*, 61(2):208–249, 1986.

[17] Michael J. Ward and Juncheng Wei. Asymmetric spike patterns for the one-dimensional Gierer–Meinhardt model: equilibria and stability. *European Journal of Applied Mathematics*, 13(3):283–320, 2002.

[18] Juncheng Wei and Matthias Winter. On the two-dimensional Gierer–Meinhardt system with strong coupling. *SIAM Journal on Mathematical Analysis*, 30(6):1241–1263, 1999.

[19] Juncheng Wei and Matthias Winter. Spikes for the two-dimensional Gierer-Meinhardt system: The strong coupling case. *Journal of Differential Equations*, 178:478–518, 2002.

[20] Juncheng Wei and Matthias Winter. Spikes for the two-dimensional Gierer-Meinhardt system: the weak coupling case. *Journal of Nonlinear Science*, 11(6):415–458, 2001.

[21] Theodore Kolokolnikov and Michael J. Ward. Reduced wave Green's functions and their effect on the dynamics of a spike for the Gierer–Meinhardt model. *European Journal of Applied Mathematics*, 14(5):513–545, 2003.

[22] Theodore Kolokolnikov and Michael J. Ward. Bifurcation of spike equilibria in the near-shadow Gierer-Meinhardt model. *Discrete & Continuous Dynamical Systems-B*, 4(4):1033, 2004.

[23] Arjen Doelman and Harmen van der Ploeg. Homoclinic stripe patterns. *SIAM Journal on Applied Dynamical Systems*, 1(1):65–104, 2002.

[24] Theodore Kolokolnikov, Wentao Sun, Michael Ward, and Juncheng Wei. The stability of a stripe for the Gierer–Meinhardt model and the effect of saturation. *SIAM Journal on Applied Dynamical Systems*, 5(2):313–363, 2006.

[25] Theodore Kolokolnikov and Xiaofeng Ren. Smoke-Ring Solutions of Gierer–Meinhardt System in R^3. *SIAM Journal on Applied Dynamical Systems*, 10(1):251–277, 2011.

[26] Theodore Kolokolnikov, Juncheng Wei, and Wen Yang. On large ring solutions for Gierer–Meinhardt system in R3. *Journal of Differential Equations*, 255(7):1408–1436, 2013.

[27] Michael J. Ward and Juncheng Wei. The existence and stability of asymmetric spike patterns for the Schnakenberg model. *Studies in Applied Mathematics*, 109(3):229–264, 2002.

[28] David Iron, Juncheng Wei, and Matthias Winter. Stability analysis of Turing patterns generated by the Schnakenberg model. *Journal of Mathematical Biology*, 49(4):358–390, 2004.

[29] Theodore Kolokolnikov, Michael J. Ward, and Juncheng Wei. Spot self-replication and dynamics for the Schnakenburg model in a two-dimensional domain. *Journal of Nonlinear Science*, 19(1):1–56, 2009.

[30] J.C. Tzou, S. Xie, Theodore Kolokolnikov, and Michael J. Ward. The stability and slow dynamics of localized spot patterns for the 3-D Schnakenberg reaction-diffusion model. *SIAM Journal on Applied Dynamical Systems*, 16(1):294–336, 2017.

[31] P. Gray and S. K. Scott. Autocatalytic reactions in the isothermal, continuous stirred tank reactor: isolas and other forms of multistability. *Chemical Engineering Science*, 38(1):29–43, 1983.

[32] P. Gray and S. K. Scott. Autocatalytic reactions in the isothermal, continuous stirred tank reactor: oscillations and instabilities in the system a+ 2b→ 3b; b→ c. *Chemical Engineering Science*, 39(6):1087–1097, 1984.

[33] Arjen Doelman, Tasso J. Kaper, and Paul A. Zegeling. Pattern formation in the one-dimensional Gray-Scott model. *Nonlinearity*, 10(2):523, 1997.

[34] Arjen Doelman, Robert A. Gardner, and Tasso J. Kaper. Stability analysis of singular patterns in the 1D Gray-Scott model: a matched asymptotics approach. *Physica D: Nonlinear Phenomena*, 122(1-4):1–36, 1998.

[35] Arjen Doelman, Robert A. Gardner, and Tasso J. Kaper. *A stability index analysis of 1-D patterns of the Gray-Scott model*. American Mathematical Soc., 2002.

[36] Theodore Kolokolnikov, Michael J. Ward, and Juncheng Wei. The existence and stability of spike equilibria in the one-dimensional Gray–Scott model on a finite domain. *Applied Mathematics Letters*, 18(8):951–956, 2005.

[37] Arjen Doelman, Tasso J. Kaper, and Wiktor Eckhaus. Slowly modulated two-pulse solutions in the Gray–Scott model I: Asymptotic construction and stability. *SIAM Journal on Applied Mathematics*, 61(3):1080–1102, 2000.

[38] Arjen Doelman, Wiktor Eckhaus, and Tasso J. Kaper. Slowly modulated two-pulse solutions in the Gray–Scott model II: geometric theory, bifurcations, and splitting dynamics. *SIAM Journal on Applied Mathematics*, 61(6):2036–2062, 2001.

[39] Wentao Sun, Michael J. Ward, and Robert Russell. The slow dynamics of two-spike solutions for the Gray–Scott and Gierer–Meinhardt systems: competition and oscillatory instabilities. *SIAM Journal on Applied Dynamical Systems*, 4(4):904–953, 2005.

[40] Theodore Kolokolnikov, Frédéric Paquin-Lefebvre, and Michael J. Ward. Stable asymmetric spike equilibria for the Gierer–Meinhardt model with a precursor field. *IMA Journal of Applied Mathematics*, 85(4):605–634, 2020.

[41] Theodore Kolokolnikov and Shuangquan Xie. Spike density distribution for the Gierer–Meinhardt model with precursor. *Physica D: Nonlinear Phenomena*, 402:132247, 2020.

[42] William H. Hamer. *Epidemic disease in England: the evidence of variability and of persistency of type*. Bedford Press, 1906.

[43] Ronald Ross. *The Prevention of Malaria*. John Murray, 1911.

[44] William Ogilvy Kermack and Anderson G. McKendrick. A contribution to the mathematical theory of epidemics. *Proceedings of the Royal Society of London. Series A, Containing papers of a mathematical and physical character*, 115(772):700–721, 1927.

[45] Fred Brauer, Carlos Castillo-Chavez, and Carlos Castillo-Chavez. *Mathematical models in population biology and epidemiology*, volume 2. Springer, 2012.

[46] Maia Martcheva. *An introduction to mathematical epidemiology*, volume 61. Springer, 2015.

[47] Zhilan Feng and Jorge X. Velasco-Hernández. Competitive exclusion in a vector-host model for the Dengue fever. *Journal of Mathematical Biology*, 35(5):523–544, 1997.

[48] Herbert W. Hethcote. The mathematics of infectious diseases. *SIAM Review*, 42(4):599–653, 2000.

[49] Pauline van den Driessche and James Watmough. A simple SIS epidemic model with a backward bifurcation. *Journal of Mathematical Biology*, 40(6):525–540, 2000.

[50] Henryk Fuks and Anna T. Lawniczak. Individual-based lattice model for spatial spread of epidemics. *Discrete Dynamics in Nature and Society*, 6(3):191–200, 2001.

[51] Ruth J. Doran and Shawn W. Laffan. Simulating the spatial dynamics of foot and mouth disease outbreaks in feral pigs and livestock in Queensland, Australia, using a susceptible-infected-recovered cellular automata model. *Preventive Veterinary Medicine*, 70(1-2):133–152, 2005.

[52] Julien Arino and P. Van den Driessche. A multi-city epidemic model. *Mathematical Population Studies*, 10(3):175–193, 2003.

[53] Alun L. Lloyd and Vincent A.A. Jansen. Spatiotemporal dynamics of epidemics: synchrony in metapopulation models. *Mathematical Biosciences*, 188(1-2):1–16, 2004.

[54] Julien Arino, Richard Jordan, and P. Van den Driessche. Quarantine in a multi-species epidemic model with spatial dynamics. *Mathematical Biosciences*, 206(1):46–60, 2007.

[55] Hua Yuan and Guoqing Chen. Network virus-epidemic model with the point-to-group information propagation. *Applied Mathematics and Computation*, 206(1):357–367, 2008.

[56] Marcelo Kuperman and Guillermo Abramson. Small world effect in an epidemiological model. *Physical Review Letters*, 86(13):2909, 2001.

[57] James D. Murray. *Mathematical biology. II Spatial models and biomedical applications {Interdisciplinary Applied Mathematics V. 18}*. Springer-Verlag New York Incorporated New York, 2001.

[58] Gui-Quan Sun. Pattern formation of an epidemic model with diffusion. *Nonlinear Dynamics*, 69(3):1097–1104, 2012.

[59] A. J. Koch and Hans Meinhardt. Biological pattern formation: from basic mechanisms to complex structures. *Reviews of Modern Physics*, 66(4):1481, 1994.

[60] David M. Holloway and Lionel G. Harrison. Order and localization in reaction-diffusion pattern. *Physica A: Statistical Mechanics and its Applications*, 222(1-4):210–233, 1995.

[61] Hans Meinhardt. Models of biological pattern formation. *New York*, page 118, 1982.

[62] Hans Meinhardt. *The algorithmic beauty of sea shells*. Springer Science & Business Media, 2009.

[63] Juncheng Wei. On single interior spike solutions of the Gierer–Meinhardt system: uniqueness and spectrum estimates. *European Journal of Applied Mathematics*, 10(4):353–378, 1999.

[64] A. Doelman, R.A. Gardner, and T.J. Kaper. Large stable pulse solutions in reaction-diffusion equations. *Indiana University Mathematics Journal*, 50(1):443–507, 2001.

[65] David Iron and Michael J. Ward. A metastable spike solution for a nonlocal reaction-diffusion model. *SIAM Journal on Applied Mathematics*, 60(3):778–802, 2000.

[66] M. J. Ward and J. Wei. Hopf bifurcations and oscillatory instabilities of spike solutions for the one-dimensional Gierer-Meinhardt model. *Journal of Nonlinear Science*, 13(2), 2003.

[67] Harmen Van der Ploeg and Arjen Doelman. Stability of spatially periodic pulse patterns in a class of singularly perturbed reaction-diffusion equations. *Indiana University Mathematics Journal*, pages 1219–1301, 2005.

[68] Xinfu Chen and MichaL Kowalczyk. Dynamics of an interior spike in the Gierer–Meinhardt system. *SIAM Journal on Mathematical Analysis*, 33(1):172–193, 2001.

[69] W.A. Macfadyen. Vegetation patterns in the semi-desert plains of British Somaliland. *The Geographical Journal*, 116(4/6):199–211, 1950.

[70] David J. Tongway and John A. Ludwig. Vegetation and soil patterning in semi-arid mulga lands of eastern Australia. *Australian Journal of Ecology*, 15(1):23–34, 1990.

[71] Alyson K. McDonald, Robert J. Kinucan, and Lynn E. Loomis. Ecohydrological interactions within banded vegetation in the northeastern Chihuahuan Desert, USA. *Ecohydrology: Ecosystems, Land and Water Process Interactions, Ecohydrogeomorphology*, 2(1):66–71, 2009.

[72] John A. Ludwig and David J. Tongway. Spatial organisation of landscapes and its function in semi-arid woodlands, australia. *Landscape Ecology*, 10(1):51–63, 1995.

[73] Reinier HilleRisLambers, Max Rietkerk, Frank van den Bosch, Herbert H.T. Prins, and Hans de Kroon. Vegetation pattern formation in semi-arid grazing systems. *Ecology*, 82(1):50–61, 2001.

[74] Erez Gilad, Jost von Hardenberg, Antonello Provenzale, Moshe Shachak, and Ehud Meron. Ecosystem engineers: from pattern formation to habitat creation. *Physical Review Letters*, 93(9):098105, 2004.

[75] J. M. Thiery, J-M d'Herbès, and Christian Valentin. A model simulating the genesis of banded vegetation patterns in Niger. *Journal of Ecology*, pages 497–507, 1995.

[76] Max Rietkerk and Johan van de Koppel. Alternate stable states and threshold effects in semi-arid grazing systems. *Oikos*, pages 69–76, 1997.

[77] Jost von Hardenberg, Ehud Meron, Moshe Shachak, and Yair Zarmi. Diversity of vegetation patterns and desertification. *Physical Review Letters*, 87(19):198101, 2001.

[78] Ehud Meron. Vegetation pattern formation: the mechanisms behind the forms. *Physics Today*, 72(11):30–36, 2019.

[79] Ehud Meron, Erez Gilad, Jost von Hardenberg, Moshe Shachak, and Yair Zarmi. Vegetation patterns along a rainfall gradient. *Chaos, Solitons & Fractals*, 19(2):367–376, 2004.

[80] Sonia Kéfi, Maarten B. Eppinga, Peter C. de Ruiter, and Max Rietkerk. Bistability and regular spatial patterns in arid ecosystems. *Theoretical Ecology*, 3(4):257–269, 2010.

[81] Robbin Bastiaansen, Martina Chirilus-Bruckner, and Arjen Doelman. Pulse solutions for an extended Klausmeier model with spatially varying coefficients. *SIAM Journal on Applied Dynamical Systems*, 19(1):1–57, 2020.

[82] Jonathan A. Sherratt. Pattern solutions of the Klausmeier model for banded vegetation in semi-arid environments I. *Nonlinearity*, 23(10):2657, 2010.

[83] Jonathan A. Sherratt. Pattern solutions of the Klausmeier model for banded vegetation in semi-arid environments II: patterns with the largest possible propagation speeds. *Proceedings of the Royal Society A: Mathematical, Physical and Engineering Sciences*, 467(2135):3272–3294, 2011.

[84] Jonathan A. Sherratt. Pattern solutions of the Klausmeier model for banded vegetation in semi-arid environments III: the transition between homoclinic solutions. *Physica D: Nonlinear Phenomena*, 242(1):30–41, 2013.

[85] Jonathan A. Sherratt. Pattern solutions of the Klausmeier model for banded vegetation in semiarid environments IV: Slowly moving patterns and their stability. *SIAM Journal on Applied Mathematics*, 73(1):330–350, 2013.

[86] Jonathan A. Sherratt. Pattern solutions of the Klausmeier model for banded vegetation in semiarid environments V: the transition from patterns to desert. *SIAM Journal on Applied Mathematics*, 73(4):1347–1367, 2013.

[87] Sjors van der Stelt, Arjen Doelman, Geertje Hek, and Jens D.M. Rademacher. Rise and fall of periodic patterns for a generalized Klausmeier–Gray–Scott model. *Journal of Nonlinear Science*, 23(1):39–95, 2013.

[88] D. L. Benson, J. A. Sherratt, and P. K. Maini. Diffusion driven instability in inhomogeneous domain. *Bulletin of Mathematics Biology*, 55(2):365–384, 1993.

[89] L. J. Shaw and J. D. Murry. Analysis of a model for complex skin pattern. *SIAM Journal on Applied Math*, 50(2):628–648, 1990.

[90] Juncheng Wei and Matthias Winter. Stationary multiple spots for reaction–diffusion systems. *Journal of Mathematical Biology*, 57(1):53–89, 2008.

[91] Shuangquan Xie, Theodore Kolokolnikov, and Yasumasa Nishiura. Complex oscillatory motion of multiple spikes in a three-component Schnakenberg system. *Nonlinearity*, 34(8):5708, 2021.

[92] Chunyi Gai, David Iron, and Theodore Kolokolnikov. Localized outbreaks in an SIR model with diffusion. *Journal of Mathematical Biology*, 80(5):1389–1411, 2020.

[93] Chunyi Gai, David Iron, Theodore Kolokolnikov, and John Rumsey. Spike dynamics in the presence of noise. *SIAM Journal on Applied Dynamical Systems*, 19(4):2783–2802, 2020.

[94] Chunyi Gai and Theodore Kolokolnikov. Resource-mediated competition between two plant species with different rates of water intake. submitted, 2021.

[95] Fahad Al Saadi, Alan Champneys, Chunyi Gai, and Theodore Kolokolnikov. Spikes and localised patterns for a novel schnakenberg model in the semi-strong interaction regime. *European Journal of Applied Mathematics*, pages 1–20.

[96] David Iron and Michael J. Ward. The dynamics of multispike solutions to the one-dimensional Gierer–Meinhardt model. *SIAM Journal on Applied Mathematics*, 62(6):1924–1951, 2002.

[97] Cyrill B. Muratov and V.V. Osipov. Stability of the static spike autosolitons in the Gray–Scott model. *SIAM Journal on Applied Mathematics*, 62(5):1463–1487, 2002.

[98] C.B. Muratov and Vyacheslav V. Osipov. Static spike autosolitons in the Gray-Scott model. *Journal of Physics A: Mathematical and General*, 33(48):8893, 2000.

[99] K. Kang, T. Kolokolnikov, and M. J. Ward. The stability and dynamics of a spike in the one-dimensional Keller-Segel model. *IMA Journal of Applied Mathematics*, 2005.

[100] Theodore Kolokolnikov and Juncheng Wei. Pattern formation in a reaction-diffusion system with space-dependent feed rate. *SIAM Review*, 60(3):626–645, 2018.

[101] Andreas Buttenschoen, Theodore Kolokolnikov, Michael J. Ward, and Juncheng Wei. Cops-on-the-dots: The linear stability of crime hotspots for a 1-D reaction-diffusion model of urban crime. *European Journal of Applied Mathematics*, 31(5):871–917, 2020.

[102] Theodore Kolokolnikov, Michael J. Ward, and Juncheng Wei. The existence and stability of spike equilibria in the one-dimensional Gray–Scott model: The low feed-rate regime. *Studies in Applied Mathematics*, 115(1):21–71, 2005.

[103] Theodore Kolokolnikov, Michael Ward, and Juncheng Wei. The stability of steady-state hot-spot patterns for a reaction-diffusion model of urban crime. *arXiv preprint arXiv:1201.3090*, 2012.

[104] William N. Reynolds, John E. Pearson, and Silvina Ponce-Dawson. Dynamics of self-replicating patterns in reaction diffusion systems. *Physical review letters*, 72(17):2797, 1994.

[105] William N. Reynolds, Silvina Ponce-Dawson, and John E. Pearson. Self-replicating spots in reaction-diffusion systems. *Physical Review E*, 56(1):185, 1997.

[106] Theodore Kolokolnikov, Michael J. Ward, and Juncheng Wei. The existence and stability of spike equilibria in the one-dimensional Gray–Scott model: the pulse-splitting regime. *Physica D: Nonlinear Phenomena*, 202(3-4):258–293, 2005.

[107] Theodore Kolokolnikov and Michael J. Ward. Bifurcation of spike equilibria in the near-shadow Gierer-Meinhardt model. *DSDS B*, 4:1033–1064, 2004.

[108] J. K. Hale, Lambertus A. Peletier, and William C. Troy. Stability and instability in the Gray-Scott model: the case of equal diffusivities. *Applied Mathematics Letters*, 12(4):59–65, 1999.

[109] J. K. Hale, L. A. Peletier, and William C. Troy. Exact homoclinic and heteroclinic solutions of the gray–scott model for autocatalysis. *SIAM Journal on Applied Mathematics*, 61(1):102–130, 2000.

[110] James P. Keener. A geometrical theory for spiral waves in excitable media. *SIAM Journal on Applied Mathematics*, 46(6):1039–1056, 1986.

[111] Theodore Kolokolnikov and Shuangquan Xie. Spike density distribution for the Gierer–Meinhardt model with precursor. *Physica D: Nonlinear Phenomena*, page 132247, 2019.

[112] Juncheng Wei and Matthias Winter. On the Gierer-Meinhardt system with precursors. *Discrete & Continuous Dynamical Systems*, 2009.

[113] Crispin W. Gardiner et al. *Handbook of Stochastic Methods*, volume 3. Springer Berlin, 1985.

[114] Sidney Redner. *A Guide to First-Passage processes*. Cambridge University Press, 2001.

[115] Julien Smith-Roberge, David Iron, and Theodore Kolokolnikov. Pattern formation in bacterial colonies with density-dependent diffusion. *European Journal of Applied Mathematics*, 30(1):196–218, 2019.

[116] Cornelis Van Der Waal, Hans De Kroon, Willem F. De Boer, Ignas M. A. Heitkönig, Andrew K. Skidmore, Henrik J. De Knegt, Frank Van Langevelde, Sipke E. Van Wieren, Rina C. Grant, Bruce R. Page, et al. Water and nutrients alter herbaceous competitive effects on tree seedlings in a semi-arid savanna. *Journal of Ecology*, pages 430–439, 2009.

[117] D.R. Gordon, J.M. Menke, and K.J. Rice. Competition for soil water between annual plants and blue oak (Quercus douglasii) seedlings. *Oecologia*, 79(4):533–541, 1989.

[118] Margherita Gioria and Bruce A. Osborne. Resource competition in plant invasions: emerging patterns and research needs. *Frontiers in Plant Science*, 5:501, 2014.

[119] K. Siteur, E. Siero, M.B. Eppinga, J.D.M. Rademacher, A. Doelman, and M. Rietkerk. Beyond Turing: The response of patterned ecosystems to environmental change. *Ecological Complexity*, 20:81–96, 2014.

[120] Yuval R. Zelnik, Hannes Uecker, Ulrike Feudel, and Ehud Meron. Desertification by front propagation? *Journal of Theoretical Biology*, 418:27–35, 2017.

[121] Olivier Lejeune, Mustapha Tlidi, and René Lefever. Vegetation spots and stripes: dissipative structures in arid landscapes. *International Journal of Quantum Chemistry*, 98(2):261–271, 2004.

[122] Karna Gowda, Yuxin Chen, Sarah Iams, and Mary Silber. Assessing the robustness of spatial pattern sequences in a dryland vegetation model. *Proceedings of the Royal Society A: Mathematical, Physical and Engineering Sciences*, 472(2187):20150893, 2016.

[123] Jonathan A. Sherratt. Wavefront propagation in a competition equation with a new motility term modelling contact inhibition between cell populations. *Proceedings of the Royal Society of London. Series A: Mathematical, Physical and Engineering Sciences*, 456(2002):2365–2386, 2000.

[124] M. J. Ward and J. Wei. The existence and stability of asymmetric spike patterns for the Schnakenberg model. *Studies in Applied Mathematics*, 109:229–264, 2002.

Appendices

Appendix A

FlexPDE script for SIRS system

To find the threshold of competition instability D_{SK}^{com} numerically, we solve system (2.2) using FlexPDE and gradually increase the value of the diffusion rate D_S until competition (or coarsening) instability is observed. Figure A.1 illustrates the FlexPDE script for this, in which the initial conditions are: S and R are constants, I contains 2 spikes. The initial conditions are scaled so that the total mass of the population is $N = 5$. Coarsening can be observed when D_S is increased to 3.2.

The numerical threshold of self-replication can be found in the same simulations using FlexPDE. Taking initial conditions as K-spike solutions, we can find D_{SK}^{rep} by gradually decreasing the value of D_S until self-replication from K spikes to $K + 1$ spikes is observed.

```
TITLE 'SIRS coarsening'     { the problem identification }
COORDINATES cartesian1  { coordinate system, 1D,2D,3D, etc }
VARIABLES        { system variables }
  S
  I
  R                { choose your own names }
SELECT       { method controls }
errlim=1e-3
DEFINITIONS    { parameter definitions }
eps=0.02
DS=3.2
DI=eps^2
DR=5
gamma=1
L= 1
tmax=1e5
N=5
S0=0.1
R0=1.5
integ=2*L*(S0+R0)+6*eps/S0
INITIAL VALUES
S=S0*N/integ
I=(1.5/(cosh((x-0.5)/eps))^2+1.5/(cosh((x+0.5)/eps))^2)/S0*(N/integ)
R=R0*N/integ
EQUATIONS        { PDE's, one for each variable }
S:  dt(S)= DS*dxx(S)-S*I^2+gamma*R
I:    dt(I) = DI*dxx(I)-I+S*I^2
R:  dt(R)= DR*dxx(R)+I-gamma*R
BOUNDARIES       { The domain definition }
  REGION 1       { For each material region }
    START(-L)   { Walk the domain boundary }
point  natural (S)=0
point  natural (I)=0
point  natural (R)=0
    LINE TO  (L)
 TIME 0 TO tmax    { if time dependent }
MONITORS         { show progress }
PLOTS         { show progress }
          { save result displays }
for cycle=1
elevation(S,I,R) from (-L) to (L)
history(integral(S+I+R))
END
```

Figure A.1: FlexPDE script for simulating (2.2).

Appendix B

Numerical method

We use finite differences to solve (3.2) numerically.

We discretize in space using N gridpoints, $\Delta x = 2L/N$, and in time using stepsize Δt so that $u(x_k, t_j) \approx u_j^k$, $v(x,t) \approx v_j^k$ where $x_k = -L + \Delta x k$ with $k = 1 \dots N$, $t_j = \Delta t j$. We use a simple implicit-explicit finite difference scheme, similar to what is described in [6]. The Laplacian is discretized implicitly, the remaining terms are discretized explicitly. This results in:

$$\frac{u_{j+1}^k - u_j^k}{\Delta t} = \varepsilon^2 \frac{u_{j+1}^{k+1} + u_{j+1}^{k-1} - 2u_{j+1}^k}{(\Delta x)^2} - u_j^k + \frac{\left(u_j^k\right)^2}{v_j^k} + \sigma \frac{\sqrt{\Delta t}}{\Delta t} W_j^k,$$

$$0 = \frac{v_{j+1}^{k+1} + v_{j+1}^{k-1} - 2v_{j+1}^k}{(\Delta x)^2} - v_j^k + \frac{\left(u_j^k\right)^2}{\varepsilon}.$$

Neumann boundary conditions are implemented by assuming $u_{j+1} = u_{j-1}$ when $j = 1$ or N, and similarly for v.

Here, W_j^k is the discretization of the noise term. To compute W_j^k, note that $W(x,t)$ is normally distributed with zero mean (since it is a sum of normal variables). Moreover, we have

$$\mathcal{E}\left\{W(x_k,t)W(x_l,t)\right\} = \begin{cases} 0, & \text{if } k \neq l \\ N, & \text{if } k = l \end{cases}.$$

This follows from the fact that $\mathcal{E}\left\{\phi_k \phi_l\right\} = \mathcal{E}\left\{\psi_k \psi_l\right\} = \delta_{kl}$, $\mathcal{E}\left\{\phi_k \psi_l\right\} = 0$, and identities

$$\sum_{m=1}^{(N-1)/2} \cos\left(\frac{2\pi}{N} ml\right) \cos\left(\frac{2\pi}{N} mk\right) = \left(\frac{N}{4} - 1\right) \delta_{l,k}, \quad \sum_{m=1}^{(N-1)/2} \sin\left(\frac{2\pi}{N} ml\right) \sin\left(\frac{2\pi}{N} mk\right) = \frac{N}{4} \delta_{l,k},$$

$$\sum_{m=1}^{(N-1)/2} \sin\left(\frac{2\pi}{N} mj\right) \cos\left(\frac{2\pi}{N} mk\right) = 0.$$

Therefore W_j^k, $k = 1 \dots N$ are N independent normally distributed variables with mean zero and standard deviation $\sqrt{N}$. In matlab, such a random variable is generated using the command `sqrt(N)*randn`. Figure B.1 illustrates the code for the above.

```
L =1; sigma =0.1; eps =0.1;
N =200; dt =0.1;
x = linspace (-L,L,N)';
dx=x(2) -x(1);
Lap = -2* diag ( ones (1,N))+ diag ( ones (1,N -1) ,1)+ diag ( ones (1,N -1) ,-1);
Lap (1 ,2) =2; Lap (N,N -1) =2; Lap=Lap/dx ^2;
Id = eye (N);
M1 = Id -eps ^2* Lap *dt;
M2 = Id -Lap ;

v=x*0+1; u= sech ((x-L*0)/eps);
tout =0;
for t=0: dt :4000
    noise = randn (N ,1)* sqrt (N)* sigma ;
    rhs1 =u+(-u+u .^2./ v)*dt+ noise .*u* sqrt (dt);
    rhs2 =u .^2./ eps;
    u=M1\ rhs1 ;
    v=M2\ rhs2 ;
    if t> tout
        tout = tout +10;
        plot (x,u,x,v);
        legend ('u','v'); xlabel ('x');
        title ( sprintf ('t=%g eps =%g',t,eps ));
        drawnow ;
    end;
end ;
```

Figure B.1: Code for simulating (3.2).

Appendix C

Some integrals

1. Evaluation of $F_p(x) = \int_{-\infty}^{\infty} \sin(xy) w^p w_y dy$ with $p = 0$. Integrating by parts we have

$$F_0(x) = -x \int_{-\infty}^{\infty} \cos(xy) w(y) dy = -6x \,\mathrm{Re} \left(\int_{-\infty}^{\infty} \frac{e^{ixy}}{\left(e^{y/2} + e^{-y/2}\right)^2} dy \right).$$

The integrand has residues at $y = i\pi(1 + 2n),\ n \in \mathbb{Z}$. A standard computation of a second-order residue yields

$$\mathrm{Res}_{y=i\pi} \frac{e^{ixy}}{\left(e^{y/2} + e^{-y/2}\right)^2} = -ixe^{-\pi x}.$$

Consider a rectangular contour C traversed counter-clockwise whose base C_1 is the x-axis, whose height C_2 is at $y = i2\pi$, and whose left and right sides go to $\pm\infty$. Then

$$\int_{C_1} \frac{e^{ixy}}{\left(e^{y/2} + e^{-y/2}\right)^2} dy = I; \qquad \int_{C_2} \frac{e^{ixy}}{\left(e^{y/2} + e^{-y/2}\right)^2} dy = -e^{-2\pi x} I$$

so that $I - e^{-2\pi x} I = 2\pi x e^{-\pi x}$ or $I = \frac{\pi x}{\sinh(\pi x)}$. This yields

$$F_0(x) = \frac{-6\pi x^2}{\sinh(\pi x)}. \tag{C.1}$$

2. Evaluation of $F_p(x)$ with $p = 1$. Integrating by parts we have

$$\begin{aligned} F_1 &= -\frac{x}{2} \int_{-\infty}^{\infty} \cos(xy) w^2 dy = -\frac{x}{2} \int_{-\infty}^{\infty} \cos(xy) \left(w - w''\right) dy = \\ &= -\frac{x}{2} \int_{-\infty}^{\infty} \cos(xy) \left(1 + x^2\right) w dy = \frac{(1 + x^2)}{2} F_0(x). \end{aligned}$$

This yields

$$F_1(x) = \frac{-3\pi \left(x^2 + x^4\right)}{\sinh(\pi x)}. \tag{C.2}$$

3. Evaluation of $\int_0^{\infty} \left(F_p(x)\right)^2 dx$. We first evaluate the integrals

$$I_K = \int_0^{\infty} \frac{x^K}{\left(e^{\pi x} - e^{-\pi x}\right)^2}, \quad K = 2, 4, 6, 8.$$

We have,

$$\frac{x^{2K}}{\left(e^{\pi x}-e^{-\pi x}\right)^2}=\frac{x^K e^{-2\pi x}}{\left(1-e^{-2\pi x}\right)^2}=\sum_{n=1}^{\infty}x^K e^{-2\pi x n}n$$

and recalling that $\int_0^\infty x^K e^{-sx}dx=\Gamma(K+1)s^{-K-1}$ we obtain

$$I_K=\Gamma(K+1)\left(2\pi\right)^{-K-1}\sum_{n=1}^{\infty}n^{-K}.$$

The sum above is the zeta function whose values for even K are well known (see Wikipedia). In particular this yields,

$$I_2=\frac{1}{24\pi},\quad I_4=\frac{1}{120\pi},\quad I_6=\frac{1}{168\pi},\quad I_8=\frac{1}{120\pi}.$$

Finally we get:

$$\int_0^\infty\left(F_0(x)\right)^2dx=144\pi^2 I_4=\frac{6}{5}\pi; \tag{C.3}$$

$$\int_0^\infty\left(F_1(x)\right)^2dx=36\pi^2\left(I_8+2I_6+I_4\right)=\frac{36}{35}\pi. \tag{C.4}$$

Appendix D

Derivation of the MFPT equation

Here, we derive the formula for the MFPT from the first principles. Suppose we are given a SODE with variable drift and noise:

$$dx = f(x)dt + \sigma(x)\sqrt{dt}\xi.$$

The following integral equation gives the MFPT:

$$u(x) = dt + \int_{-\infty}^{\infty} \frac{\exp\left(-\frac{(x-y)^2}{2\sigma^2(x)dt}\right)}{\sqrt{2\pi dt}\sigma(x)} u(y + f(x)dt)dy. \tag{D.1}$$

It states that the MFPT at location x can be computed by looking at the MFPT at all other locations y, taking a deterministic jump $f(x)dt$, then taking a stochastic jump weighted by the probability of getting from y to x.

We next perform a change of variables, $y = x + z\sqrt{2\sigma^2(x)dt}$, so that (D.1) becomes

$$u(x) = dt + \int_{-\infty}^{\infty} \frac{\exp\left(-z^2\right)}{\sqrt{\pi}} u\left(x + \varepsilon z + \varepsilon^2 b\right) dz, \quad \text{where} \quad \varepsilon = \sqrt{2\sigma^2(x)dt}, \quad b = \frac{f(x)}{2\sigma^2(x)}. \tag{D.2}$$

We further expand:

$$u\left(x + z\varepsilon + \varepsilon^2 b\right) = u(x) + \varepsilon z u_x + \varepsilon^2 \left(b u_x + \frac{z^2}{2} u_{xx}\right) + \dots$$

and use

$$\int_{-\infty}^{\infty} \frac{\exp\left(-z^2\right)}{\sqrt{\pi}} = 1, \quad \int_{-\infty}^{\infty} \frac{z\exp\left(-z^2\right)}{\sqrt{\pi}} = 0, \quad \int_{-\infty}^{\infty} \frac{z^2\exp\left(-z^2\right)}{\sqrt{\pi}} = \frac{1}{2},$$

so that (D.1) becomes

$$0 = dt + \varepsilon^2 \left(b u_x + \frac{1}{4} u_{xx}\right)$$

or

$$1 + f(x)u_x + \frac{\sigma^2(x)}{2} u_{xx} = 0.$$

For a similar derivation of the Fokker-Plank equation with variable diffusivity $\sigma(x)$, see Appendix in [115].